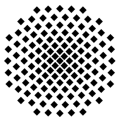

Universität Stuttgart

Quantum states with topological properties via dipolar interactions

Von der Fakultät Mathematik und Physik der Universität Stuttgart zur Erlangung der Würde eines Doktors der Naturwissenschaften (Dr. rer. nat.) genehmigte Abhandlung.

vorgelegt von

David Peter

aus Heilbronn

Hauptberichter:	Prof. Dr. Hans Peter Büchler
Mitberichterin:	Prof. Dr. Maria Daghofer

Tag der mündlichen Prüfung: 25. Juni 2015

Institut für Theoretische Physik III

Universität Stuttgart

2015

List of previous publications

[P1] D. Peter, S. Müller, S. Wessel, and H. P. Büchler. "Anomalous Behavior of Spin Systems with Dipolar Interactions". Phys. Rev. Lett. **109** (2012), 025303. arXiv: 1203.1624 (cit. on pp. 15, 29, 59, 89).

[P2] D. Peter, K. Pawłowski, T. Pfau, and K. Rzażewski. "Mean-field description of dipolar bosons in triple-well potentials". J. Phys. B **45** (2012), 225302. arXiv: 1201.2615.

[P3] J. B. Balewski, A. T. Krupp, A. Gaj, D. Peter, H. P. Büchler, R. Löw, S. Hofferberth, and T. Pfau. "Coupling a single electron to a Bose-Einstein condensate". Nature **502** (2013), 664. arXiv: 1306.5181 (cit. on p. 81).

[P4] D. Peter, A. Griesmaier, T. Pfau, and H. P. Büchler. "Driving Dipolar Fermions into the Quantum Hall Regime by Spin-Flip Induced Insertion of Angular Momentum". Phys. Rev. Lett. **110** (2013), 145303. arXiv: 1302.1308 (cit. on p. 51).

[P5] M. Klinsmann, D. Peter, and H. P. Büchler. "Ferroelectric quantum phase transition with cold polar molecules" (2014). arXiv: 1412.0521 (cit. on pp. 17, 26).

[P6] D. Peter, N. Y. Yao, N. Lang, S. D. Huber, M. D. Lukin, and H. P. Büchler. "Topological bands with Chern number C=2 by dipolar exchange interactions". Phys. Rev. A **91** (2015), 053617. arXiv: 1410.5667 (cit. on pp. 15, 29, 59, 89).

Zusammenfassung

Die vorliegende Arbeit beschäftigt sich mit der Untersuchung verschiedener Modellsysteme im Rahmen der ultrakalten Quantengase. Im Mittelpunkt stehen dabei neuartige Verfahren um Quantenzustände mit topologisch nichttrivialen Eigenschaften mittels dipolaren Wechselwirkungen zu realisieren. Ein berühmtes Beispiel für einen Zustand mit topologischen Eigenschaften zeigt sich im Quanten-Hall Effekt. Die exakte Quantisierung der Hall-Leitfähigkeit kann durch das Auftreten einer topologischen Invarianten verstanden werden. Die Robustheit physikalischer Effekte gegenüber äußeren Störungen macht topologische Materialien dabei interessant für Anwendungen. Entdeckt wurde der Quanten-Hall Effekt in zweidimensionalen Elektronengasen bei extrem tiefen Temperaturen und hohen Magnetfeldern. Die schwierigen experimentellen Bedingungen, sowie eine Reihe offener Fragen, besonders im Bereich des fraktionalen Quanten-Hall Effekts, motivieren daher die Suche nach alternativen Systemen.

Seit einigen Jahren sind Experimente auf dem Gebiet der ultrakalten Quantengase so weit fortgeschritten, dass routinemäßig neuartige Modellsysteme simuliert werden können. Ein Abschnitt dieser Arbeit beschäftigt sich mit der Realisierung des Quanten-Hall Effekts in ultrakalten Gasen. Ein Problem besteht darin, den Effekt des Magnetfelds auf Elektronen mit elektrisch neutralen Atomen zu simulieren. Eine mögliche Lösung, die auf Ideen von Larmor zurückgeht, bedient sich einer exakten Analogie zwischen geladenen Teilchen im Magnetfeld und neutralen Teilchen in einem rotierenden System, wobei die Rotationsfrequenz die Rolle des Magnetfeldes übernimmt. Die Corioliskraft im rotierenden System verhält sich dabei beispielsweise wie die Lorentzkraft im Magnetfeld. Unser Ansatz besteht darin, die Relaxierung in dipolaren Systemen zu nutzen, um das zweidimensionale Quantengas in Rotation zu versetzten. Dabei wird der interne Drehimpuls der Atome durch die Dipol-Dipol Wechselwirkung in eine externe Rotation umgewandelt. Um den Vorgang mehrmals zu

wiederholen, kann der interne Zustand anschließend durch ein externes Magnetfeld zurückgesetzt werden. Der Vorteil dieser Methode besteht darin, dass nicht die Rotationsfrequenz des Systems gesteuert wird, sondern direkt der Gesamtdrehimpuls. Hierdurch kann eine intrinsische Instabilität umgangen werden, die auftritt, wenn die Rotationsfrequenz mit der Fallenfrequenz vergleichbar wird. Bei Kenntnis der genauen Atomzahl können mit dieser Methode dann bestimmte Quanten-Hall Zustände realisiert werden, da deren Gesamtdrehimpuls bekannt ist. Weiterhin untersuchen wir den Einfluss der Wechselwirkung im Rahmen einer vollständigen numerischen Simulation und studieren die dipolar wechselwirkenden Zustände bei fraktionaler Füllung.

Der zweite große Teil dieser Arbeit beschäftigt sich mit dipolaren Spin-Systemen und topologischen Bandstrukturen. Wir gehen dabei von einer vorgegebenen zweidimensionalen Gitterstruktur aus, auf deren Gitterplätzen sich einzelne fest angebrachte Dipole in Form von polaren Molekülen oder Rydberg Atomen befinden. Wir sind an der Dynamik der Anregungen dieser Dipole interessiert, die durch die Dipol-Dipol Wechselwirkung getrieben wird. Insbesondere können diese Anregungen zwischen verschiedenen Dipolen ausgetauscht werden. Damit verhalten sie sich ähnlich wie tunnelnde Elektronen in einem Ionengitter, wobei die Prozesse jedoch aufgrund der Dipol-Dipol Wechselwirkung langreichweitig sind. Dies führt in zwei Dimensionen zu Veränderungen bei kleinen Impulsen. Wir untersuchen dipolare Spin-Systeme im Rahmen der Spinwellen-Theorie, die unter anderem eine spontan gebrochene kontinuierliche Symmetrie bei endlichen Temperaturen vorhersagt.

Des Weiteren zeigen wir, dass in dipolaren Systemen topologische Bandstrukturen realisiert werden können. Betrachtet man zwei verschiedene Anregungen mit unterschiedlichem internen Drehimpuls, dann können diese über die dipolare Wechselwirkung ineinander umgewandelt werden. Dabei tritt ein komplexer Faktor auf, welcher der Gesamtdrehimpuls-Erhaltung Rechnung trägt. Diese Spin-Bahn Kopplung kann dann zu nichttrivialen Phasen in Tunnelprozessen auf geschlossenen Wegen führen. Das entspricht aber gerade dem Effekt eines Magnetfeldes auf ein geladenes Teilchen, wobei die Phase den magnetischen Fluss in Einheiten des Flussquants angibt. Wird außerdem die Zeitumkehr-Symmetrie gebrochen, können in diesen Systemen topologische Bänder auftreten, deren Charakter von der Geometrie des Gitters abhängt. Wir studieren das Verhalten der auftretenden chiralen Zustände auf dem Rand und untersuchen den Einfluss von Unordnung auf die topologische Struktur.

Contents

The story so far: In the beginning the Universe was created. This has made a lot of people very angry and been widely regarded as a bad move.

Douglas Adams

Introduction

The history of topological materials is just a little over thirty years old. A good point to start is the discovery of the quantized Hall conductance in two-dimensional semiconductor samples by von Klitzing in the early 1980s [7, 8]. He found that the Hall conductance develops plateaus as a function of the magnetic field which are exactly quantized in multiples of a fundamental constant that depends on the elementary charge and Planck's constant. In particular, it is independent of any material properties or external conditions. Due to the high precision of the quantization levels, for which an explanation was given in the following years by Laughlin and Halperin [9, 10], this effect immediately found applications in metrology as a direct measurement of the fine structure constant and as a standard for the unit of resistance. The discovery by von Klitzing was awarded with the 1985 Nobel Prize in physics.

A few years after the discovery, Thouless and others discovered the first connection to topological properties [11–17]. They found a direct relation between the Hall conductance and a topological invariant called Chern number. In much the same way that the number of 'handles' of a closed two-dimensional manifold can be calculated by an integration over its curvature, the Chern number of a Hamiltonian can be calculated by integrating its Berry curvature over a periodic two-dimensional configuration space. Similar to the Gaussian curvature of the manifold, the Berry curvature of the quantum mechanical system quantifies the geometric changes of the wave functions under transport around closed loops [18, 19]. The connection of the quantized Hall conductance to a topological invariant manifests itself in the robustness of the physical effect against local perturbations.

A related, but considerably more complex phenomenon was experimentally discovered by Tsui, Störmer and Gossard in 1982 at even lower temperatures in cleaner samples [20]. They found that the Hall conductance could additionally

develop plateaus at certain fractional values of the filling factor, the ratio between the number of electrons and the number of magnetic flux quanta threading through the sample. These plateaus correspond to fractionally filled Landau levels and could not be explained by a single-particle treatment. Once again, it was Laughlin who was able to explain the phenomenon [21], winning him the 1998 Nobel Prize in physics together with Tsui and Störmer. He found that the two-dimensional electron gas condenses into a new state of matter, a quantum fluid with fractionally charged excitations and anyonic statistics. This strongly correlated state of matter is an example of a topologically ordered state with a ground state degeneracy that depends on the topology of the underlying space and a robustness against local perturbations [22, 23]. The structure of some fractional quantum Hall states still remains unexplained. The most prominent example is the even-denominator state at a filling of $^5/_2$ that was experimentally observed as early as 1987 by Willet et al. [24]. Particular interest in this state draws from work by Moore and Read [25], suggesting that it might give rise to quasiparticles with non-Abelian statistics. Interchange of non-Abelian anyons leads to a change in the ground state manifold of the system. This property can be utilized for fault-tolerant quantum computation, an idea that has been proposed by Kitaev in 1997 [26]

Fundamental questions about the nature of these states as well as their prospective use in topological quantum computation spur the research in this field today. Traditional experiments with semiconductor samples remain challenging due to immense requirements on the sample quality, low temperatures and high magnetic fields. With the turn of the century and the advent of ultracold gases experiments, new ideas how to reach the Quantum Hall regime emerged. Unmatched control over system parameters as well as the ability to manipulate and observe on the single-particle level turn these systems into an optimal platform to advance our understanding in the field of Quantum Hall physics. A fundamental problem appears when trying to emulate the effect of the magnetic field. Electrically neutral atoms clearly do not couple to the magnetic vector potential in the way that electrons do. Various solutions to this problem have been proposed and experimentally implemented. Following an analogy that goes back to ideas by Larmor around 1900, it is possible to use a rapid rotation to induce an effective magnetic field for the neutral particles [27]. In the two-dimensional system, the frequency of rotation corresponds to the effective magnetic field strength parametrized by the cyclotron frequency. Likewise, the Coriolis force is in one-to-one correspondence with the Lorentz

force. Starting in the early 2000s, experiments in this respect have advanced over the years [28–31].

An alternative route was followed by Haldane [32]. In 1988, he proposed a lattice model with broken time-reversal symmetry which showed a quantum Hall effect without the requirement of Landau levels that would be generated by an external magnetic field. The Haldane model utilizes complex tunneling phases that respect the symmetry of the lattice and generate a topological band structure. It is a showcase for a class of materials called Chern insulators. They behave similar to ordinary band insulators, but have conducting states at the edge of the material: a physical manifestation of their non-trivial Chern number [33]. For charged particles, the required complex tunneling phases are connected to the external magnetic field through a Peierls substitution [34]. In this regard, synthetic magnetic fields can be created for neutral particles by realizing complex tunneling phases. Powerful approaches are optical flux lattices [35], laser-assisted tunneling [36–39] or lattice shaking methods [40, 41]. The latter has recently been used by Jotzu et al. to realize the Haldane 'toy model' with ultracold fermions in an optical lattice [42].

Finally, another strategy is to use spin-orbit coupling techniques [43–47] to realize topological phases. The interplay between external and internal degrees of freedom can lead to phenomena which are similar to the magnetic field counterparts. In 2005, Kane and Mele showed that spin-orbit coupled electrons in graphene can realize a topological system which encapsulates two time-reversed copies of Haldane's model [48, 49]. The resulting arrangement is an example for a time-reversal invariant topological insulator. It shows a quantum spin Hall effect where the two spin-components have a Hall conductance with opposite sign [50, 51]. A physical realization in semiconductor quantum wells was proposed by Bernevig et al. in 2006 [52, 53] and experimentally demonstrated by König et al. one year later [54].

A variety of experimental methods to probe topological materials have been established in recent years. Edge states have been observed in different systems like silicon photonics [55, 56], photonic lattices [57] and phononic mechanical systems [58]. Furthermore, the perfect control over ultracold atomic systems has led to new ways to directly measure topological properties like the Zak phase [59], the Berry curvature [60] or the Chern number [61].

This thesis is concerned with the study of quantum states which can have topological properties that are induced by dipole-dipole interactions. The first two chapters discuss the properties of dipolar systems in general. After

presenting different physical implementations of systems with dipole-dipole interactions, we start from a microscopic setup and describe a generic way to derive effective models which allow us to understand their behavior. We mainly study one- or two-dimensional systems where single dipoles are pinned at the sites of an externally given lattice structure. We work in a convenient picture where internal excitations of the dipoles in the system are being thought of as individual particles. The dipole-dipole interaction between the microscopic constituents then drives the dynamics of these effective particles. The dipolar exchange interaction in particular allows these particles to 'hop' between different lattice sites. Due to the long-range character of the dipolar interaction, these processes are strictly non-local. This is in contrast to most condensed matter systems where tunneling events are typically exponentially suppressed at larger distances. The second chapter addresses the modifications in two-dimensional spin systems which are a result of the long-range dipolar interactions.

Chapters four and five later build on these foundations and deal with the realization of topological band structures in one- and two-dimensional setups. By incorporating an additional excited state in the dipolar level structure, we are able to study the dynamics of effective particles with an internal degree of freedom. The dipolar exchange interaction then mixes the two internal states and thereby induces a coupling between the 'spin' degree of freedom and the orbital motion. We demonstrate that this spin-orbit coupling leads to the appearance of a synthetic magnetic field which generates band structures with nontrivial topological properties.

The dipolar relaxation term that leads to the appearance of the spin-orbit coupling is also used in the third chapter. Inspired by the ideas of rapidly rotating atomic gases, we devise a scheme to use the dipolar exchange interaction to realize quantum Hall states in a system of ultracold dipolar fermions. In contrast to usual stirring-techniques, the dipolar relaxation allows us to have direct control over the total angular momentum of the system. In this way, we can avoid the rotational instability and put the system in a well defined state. In particular, we show how this method can be used to generate integer and certain fractional quantum Hall states.

1

Effective models for dipolar systems

This introductory chapter is mostly of technical nature and describes the detailed steps in the derivation of effective models for the excitations in dipolar systems. Starting from the microscopic setup, the goal is to introduce a common framework to understand the different dipolar models which are subject of chapters 2, 3, 4 and 5 of this thesis. For this purpose, we will briefly introduce three kinds of physical systems exhibiting dipole-dipole interactions: dipolar atoms, polar molecules and Rydberg atoms.

After describing their properties, the next step is to understand the structure of the dipole-dipole interaction itself. It comes in two different types, although both of them are usually present at the same time. The *static* dipole-dipole interaction has been of great interest and importance in ultracold systems from the beginning [62–70]. In dipolar spin systems, it can be used to engineer Ising-type spin interactions [P1, P6, 71–75]. In this thesis, we are mostly going to focus on the second type: dipolar *exchange* interactions. Here, the internal state of the dipolar particles is allowed to change [75–80]. The exchange interactions can be subdivided into two sectors according to the angular momentum characteristic. One sector preserves the internal and external angular momentum separately. In chapter 2, this will be used to simulate XY-type spin interactions. The second sector only conserves the sum of internal and external angular momentum. This type of interaction induces a spin-orbit coupling. It plays an essential part in chapters 3 to 5, where the coupling between internal and external degrees of freedom will be used in different ways.

1.1 Physical implementations of dipolar systems

In this section we briefly review some of the possible realizations of dipolar systems in ultracold atomic and molecular systems and discuss some of the similarities as well as important differences. A detailed review on dipolar systems has been given by Lahaye et al. [70]. Other systems can also be used to simulate dipolar models, but are not detailed here. Those include trapped ions setups [81, 82], nuclear spins on diamond surfaces [83] or optical lattice clocks [84].

1.1.1 Atoms with high magnetic moments

Highly dipolar atoms were among the first experimental realizations of ultracold dipolar systems [65]. These atoms have large magnetic dipole moments due to their particular electronic structure. In the recent years, a large number of different dipolar atoms have been successfully cooled. Chromium with a magnetic moment of $6\mu_B$ is successfully used in experiments in both bosonic [65, 85] and fermionic forms [86]. Dysprosium with a magnetic moment of $10\mu_B$ is the atom with the largest dipole moment. Again, both bosonic [87] and fermionic [88] quantum degenerate gases have been demonstrated. The same is true for Erbium with a magnetic moment of $7\mu_B$, where bosonic [89] and fermionic isotopes [90] have been cooled to quantum degeneracy.

In their electronic ground state, these atoms typically posses a large amount of internal hyperfine states which contribute to a rich internal structure that can be controlled via Zeeman shifts and optical pumping techniques. Compared to polar molecules, magnetic atoms have a permanent dipole moment, even at zero field. This is useful for certain applications which involve dipolar relaxation such as demagnetization cooling [91–93]. Other advantages compared to polar molecules are the generally simpler structure which makes them easier to cool and manipulate as well as the absence of chemical reactions present in polar molecules [94, 95].

1.1.2 Polar molecules

The dipolar effects in polar molecules can be much larger due to the electric nature of the dipole moments which typically leads to an interaction strength which is stronger by up to four orders of magnitude due to the α^2 fine-structure factor between electric and magnetic systems. For a detailed comparison of the

interaction strengths, see Lahaye et al. [70]. Different species of polar molecules have been successfully cooled, among them KRb [96, 97], NaK [98] and NaLi [99]. For a review, see Quéméner and Julienne [95].

In this thesis, we focus on the rotational structure of the polar molecules, neglecting any vibrational and electronic excitations, as well as possible hyperfine structure effects. Then, the internal structure of the molecules is given by the rotational degree of freedom. Describing the molecule as a rigid rotor, the internal structure is given by $H_{\text{rot}} = BJ^2 - \mathbf{dE}$, where B is the rotational constant and $\mathbf{d}$ is the dipole moment which couples to an external electric field $\mathbf{E}$. In the absence of any external fields, the eigenstates are simply given by the angular momentum states $|J, M\rangle$ where J is the total angular momentum and $M = -J, \ldots, J$ is the projection onto the quantization axis.

In contrast to magnetic atoms, polar molecules do not have a dipole moment in the absence of external fields, that is $\langle J, M|\mathbf{d}|J, M\rangle = 0$ for any J, M. An external electric field, however, mixes states with different J and induces static dipole moments which are eventually constrained by the permanent electric dipole moment d of the molecules. Another important difference compared to magnetic atoms is the rotational splitting B which is typically much larger than the dipolar interaction strength between two molecules at realistic inter-molecule separations, although this can be circumvented [P5].

Just like atoms, polar molecules can be trapped in optical lattices [100]. The experimentally achievable fillings are, so far, much smaller than for atoms. Nevertheless, long-range dipolar effects have been observed in optical lattices, demonstrating one of the fundamental building blocks for dipolar spin models [77].

1.1.3 Rydberg atoms

While we mostly focus on polar molecules in this thesis, the physics and energy scales in highly excited Rydberg atoms can be very similar to polar molecules [101]. Dipolar effects have been observed in Rydberg atoms [80, 102–104] and the achievable dipole moments can be even larger than for polar molecules [105]. While the internal structure can be more complicated due to the fine structure, precise control through electric and magnetic fields still allows to select a suitable set of internal states for the realization of dipolar spin systems [80, 106].

1.2 Dipole-dipole interaction

The aim of this section is to rewrite the familiar interaction between two dipoles $\mathbf{d}_i$ and $\mathbf{d}_j$ at positions $\mathbf{R}_i, \mathbf{R}_j$, namely

$$H_{ij}^{\mathrm{dd}} = \frac{\kappa}{|\mathbf{R}_{ij}|^3}\left[\mathbf{d}_i \cdot \mathbf{d}_j - 3\left(\mathbf{d}_i \cdot \hat{\mathbf{R}}_{ij}\right)\left(\mathbf{d}_j \cdot \hat{\mathbf{R}}_{ij}\right)\right] = \frac{\kappa}{|\mathbf{R}_{ij}|^3} D_{ij}, \tag{1.1}$$

in a spherical tensor representation [107, 108] which will be useful throughout this thesis. Equation (1.1) is given in terms of the relative vector $\mathbf{R}_{ij} = \mathbf{R}_j - \mathbf{R}_i$ and its normalized form $\hat{\mathbf{R}}_{ij}$. The constant prefactor is given by $\kappa = 1/4\pi\epsilon_0$ for electric dipoles and by $\kappa = \mu_0/4\pi$ for magnetic dipoles. In the following, we focus on the distance-independent part $D_{ij} = \mathbf{d}_i \cdot \mathbf{d}_j - 3(\mathbf{d}_i \cdot \hat{\mathbf{R}}_{ij})(\mathbf{d}_j \cdot \hat{\mathbf{R}}_{ij})$ of the dipole-dipole interaction which can be written in terms of the spherical tensor $T^2(\mathbf{d}_i, \mathbf{d}_j)$ of rank two with the components

$$\begin{aligned} T_0^2(\mathbf{d}_i, \mathbf{d}_j) &= \frac{1}{\sqrt{6}}(d_i^+ d_j^- + 2d_i^0 d_j^0 + d_i^- d_j^+), \\ T_{\pm 1}^2(\mathbf{d}_i, \mathbf{d}_j) &= \frac{1}{\sqrt{2}}(d_i^\pm d_j^0 + d_i^0 d_j^\pm), \\ T_{\pm 2}^2(\mathbf{d}_i, \mathbf{d}_j) &= d_i^\pm d_j^\pm. \end{aligned} \tag{1.2}$$

It is constructed from the two dipole moments which are themselves rank-one tensors with spherical components

$$d_j^0 = d_j^z, \qquad d_j^\pm = \mp\frac{1}{\sqrt{2}}\left(d_j^x \pm i d_j^y\right). \tag{1.3}$$

Using this, the dipole-dipole interaction can be written in a compact form as a contraction of two rank-two tensors [109]:

$$\begin{aligned} D_{ij} &= -\sqrt{6}\, T^2(C) \cdot T^2(\mathbf{d}_i, \mathbf{d}_j) \\ &\equiv -\sqrt{6} \sum_{m=-2}^{2} (-1)^m C_{-m}^2(\theta, \phi)\, T_m^2(\mathbf{d}_i, \mathbf{d}_j). \end{aligned} \tag{1.4}$$

Here, $T^2(C)$ is the tensor which is built from the modified spherical harmonics $C_m^l(\theta, \phi) = \sqrt{\frac{4\pi}{2l+1}} Y_m^l(\theta, \phi)$. The spherical angles $\theta = \theta_{ij}$ and $\phi = \phi_{ij}$ describe the direction of the vector $\hat{\mathbf{R}}_{ij}$ in the coordinate system of the quantization axis.

We can expand this expression to get

$$\begin{aligned} D_{ij} = (1 - 3\cos^2\theta)\Big[d_i^0 d_j^0 + \frac{1}{2}\big(d_i^+ d_j^- + d_i^- d_j^+\big)\Big] \\ - \frac{3}{\sqrt{2}}\sin\theta\,\cos\theta\,\Big[\big(d_i^0 d_j^- + d_i^- d_j^0\big)\,\mathrm{e}^{+i\phi} - \big(d_i^0 d_j^+ + d_i^+ d_j^0\big)\,\mathrm{e}^{-i\phi}\Big] \\ - \frac{3}{2}\sin^2\theta\,\Big[\mathrm{e}^{+2i\phi}\,d_i^- d_j^- + \mathrm{e}^{-2i\phi}\,d_i^+ d_j^+\Big]. \end{aligned} \tag{1.5}$$

It is worth noting that the $T^2_{m=0}(\mathbf{d}_i, \mathbf{d}_j)$-terms in the first row conserve the "internal" angular momentum while the $m = 1$ ($m = 2$) terms in the second (third) row increase or decrease the internal angular momentum by one (two) quanta.

1.2.1 High-symmetry alignments

For most applications, we will be concerned with two-dimensional systems where the dipoles are aligned perpendicular to the plane. Then, the dipoles are also perpendicular to the interconnecting axis $\mathbf{R}_{ij}$, implying $\theta = \pi/2$. In this case, the $m = 1$ terms drop out and the tensorial part reduces to

$$D_{ij}^{(\mathrm{2D})} = d_i^0 d_j^0 + \frac{1}{2}\left(d_i^+ d_j^- + d_i^- d_j^+\right) - \frac{3}{2}\left(d_i^- d_j^-\,\mathrm{e}^{+2i\phi} + d_i^+ d_j^+\,\mathrm{e}^{-2i\phi}\right). \tag{1.6}$$

For a one-dimensional geometry there are two high-symmetry alignments. If the dipoles are perpendicular to the lattice direction (say, the x-direction) we can set $\phi = 0$, further simplifying D_{ij} to

$$\begin{aligned} D_{ij}^{(1D,\perp)} &= d_i^0 d_j^0 + \frac{1}{2}\left(d_i^+ d_j^- + d_i^- d_j^+\right) - \frac{3}{2}\left(d_i^- d_j^- + d_i^+ d_j^+\right) \\ &= d_i^z d_j^z + d_i^y d_j^y - 2 d_i^x d_j^x. \end{aligned} \tag{1.7}$$

Conversely, if the dipoles point along the lattice direction, we can set $\theta = 0$ in equation (1.5) to get

$$D_{ij}^{(1D,\parallel)} = -2 d_i^0 d_j^0 - \left(d_i^+ d_j^- + d_i^- d_j^+\right) = -2 d_i^z d_j^z + d_i^x d_j^x + d_i^y d_j^y. \tag{1.8}$$

1.2.2 Tilted field geometry

If we are not in a high-symmetry geometry, we can consider a more general situation (see figure 1.1a) with a two-dimensional system in the xy plane and

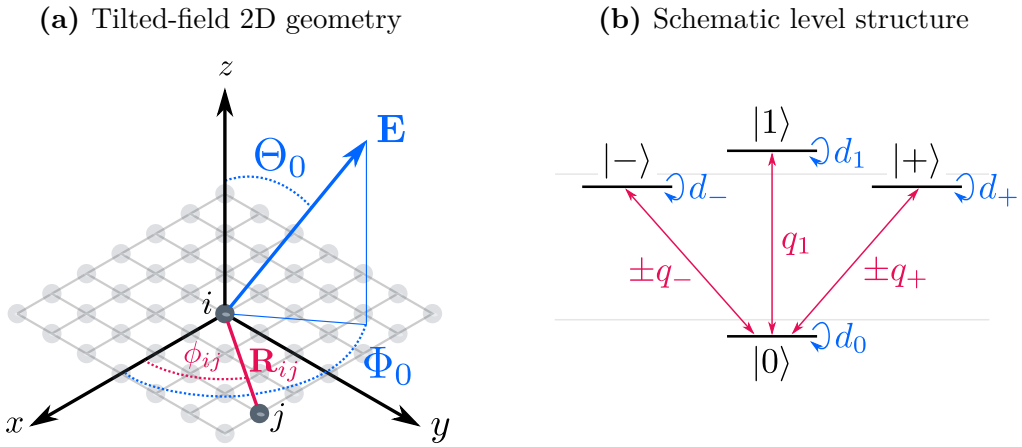

Fig. 1.1: **(a)** Illustration of the relevant axes and angles. The lattice lies in the xy plane while the static external field $\mathbf{E}$ is tilted from the z axis by an angle Θ_0 and rotated around it by an angle Φ_0 with respect to the x axis. The direction of the vector $\mathbf{R}_{ij}$, connecting two dipoles, is determined by the polar angle ϕ_{ij}. **(b)** Internal rotational states of a dipole with a ground state $|0\rangle$ and excited state $|1\rangle$ with $M = 0$, as well as two states $|\pm\rangle$ with $M = \pm 1$. The relevant static dipole moments (blue) and transition dipole moments (red) are shown. The plus sign is for the transitions going "upwards" and the minus sign for transitions going "downwards".

an external polarizing field $\mathbf{E}$ pointing in an arbitrary direction [108]. Let the external field direction be determined by the spherical angles Θ_0 and Φ_0:

$$\hat{\mathbf{E}} = \begin{pmatrix} \sin\Theta_0 \cos\Phi_0 \\ \sin\Theta_0 \sin\Phi_0 \\ \cos\Theta_0 \end{pmatrix}. \tag{1.9}$$

As before, we are interested in the interaction between two dipoles which are now separated by the in-plane vector

$$\mathbf{R}_{ij} = \begin{pmatrix} R_{ij}\cos\phi_{ij} \\ R_{ij}\sin\phi_{ij} \\ 0 \end{pmatrix}. \tag{1.10}$$

For the angle θ between the dipole orientation $\hat{\mathbf{E}}$ and the interconnection line between the dipoles $\hat{\mathbf{R}}_{ij}$, we find the relation

$$\begin{aligned} \cos\theta = \hat{\mathbf{E}} \cdot \hat{\mathbf{R}}_{ij} &= \sin\Theta_0 \left(\cos\Phi_0 \cos\phi_{ij} + \sin\Phi_0 \sin\phi_{ij}\right) \\ &= \sin\Theta_0 \cos(\phi_{ij} - \Phi_0). \end{aligned} \tag{1.11}$$

By defining the difference $\bar{\Phi} = \phi_{ij} - \Phi_0$, we can express the relevant terms in the dipole-dipole interaction from equation (1.5) as

$$\begin{aligned} f_0(\Theta_0, \bar{\Phi}) &\equiv 1 - 3\cos^2\theta = 1 - 3\sin^2\Theta_0\cos^2\bar{\Phi}, \\ f_1(\Theta_0, \bar{\Phi}) &\equiv \sin\theta\cos\theta\,\mathrm{e}^{i\phi} = \sin\Theta_0\cos\bar{\Phi}\left(\cos\Theta_0\cos\bar{\Phi} + i\sin\bar{\Phi}\right), \\ f_2(\Theta_0, \bar{\Phi}) &\equiv \sin^2\theta\,\mathrm{e}^{2i\phi} = \left(\cos\Theta_0\cos\bar{\Phi} + i\sin\bar{\Phi}\right)^2. \end{aligned} \tag{1.12}$$

Those are easily seen to reduce to the expressions (1.6) in the case of a perpendicular external field with $\Theta_0 = 0$, implying $\theta = \pi/2$ and $\bar{\Phi} = \phi_{ij}$. In total, the tensorial part of the dipole-dipole interaction is given by

$$\begin{aligned} D_{ij} = f_0(\Theta_0, \bar{\Phi})\Big[d_i^0 d_j^0 + \frac{1}{2}\left(d_i^+ d_j^- + d_i^- d_j^+\right)\Big] \\ -\frac{3}{\sqrt{2}}\Big[f_1(\Theta_0, \bar{\Phi})(d_i^0 d_j^- + d_i^- d_j^0) - f_1(\Theta_0, -\bar{\Phi})(d_i^0 d_j^+ + d_i^+ d_j^0)\Big] \\ -\frac{3}{2}\Big[f_2(\Theta_0, \bar{\Phi}) d_i^- d_j^- + f_2(\Theta_0, -\bar{\Phi}) d_i^+ d_j^+\Big]. \end{aligned} \tag{1.13}$$

1.3 Effective models

The different dipolar models throughout this thesis will be largely determined by a particular choice of internal states of the dipoles. These states can be additionally "dressed" by external DC and AC fields, with the details depending on the particular physical realization. In the following, we look at several specific choices. Each of them corresponds to a rise in complexity compared to the previous one, but also introduces additional properties and characteristics.

1.3.1 Realizing Ising and XY interactions

We start with the simplest case where we have chosen two states, denoted as $|0\rangle$ and $|1\rangle$, which have the same M quantum number (see figure 1.1b). Then, only the $d_i^0 d_j^0$ part of the dipolar interaction is relevant. We define the dipole elements

$$d_0 = \langle 0|d^0|0\rangle, \qquad d_1 = \langle 1|d^0|1\rangle, \qquad q_1 = |\langle 1|d^0|0\rangle| = |\langle 0|d^0|1\rangle|, \tag{1.14}$$

where d_α denotes a static dipole moment and q_α a transition dipole element. The evaluation of these matrix elements for polar molecules in the presence of external fields is straightforward and has been described in detail elsewhere [107].

Using the projectors $P^0 = |0\rangle\langle 0|$ and $P^1 = |1\rangle\langle 1|$, we can now express the dipole-dipole interaction (1.6) in the $\{|0\rangle, |1\rangle\}$ subspace as

$$H_{ij}^{\mathrm{dd}} = \frac{\kappa}{R_{ij}^3}\Big[d_1^2 P_i^1 P_j^1 + d_0^2 P_i^0 P_j^0 + d_1 d_0 (P_i^1 P_j^0 + P_i^0 P_j^1) + q_1^2(\sigma_i^+\sigma_j^- + \sigma_i^-\sigma_j^+)\Big], \tag{1.15}$$

where we have neglected all processes which are not energy-conserving, i.e. terms that do not conserve the number of excitations. Using $\sigma^z = P^1 - P^0$ and $\mathbb{1} = P^1 + P^0$ we find

$$H_{ij}^{\mathrm{dd}} = \frac{\kappa}{R_{ij}^3}\Big[\frac{(d_1-d_0)^2}{4}\sigma_i^z\sigma_j^z + q_1^2(\sigma_i^+\sigma_j^- + \sigma_i^-\sigma_j^+) + \frac{d_1^2-d_0^2}{4}(\sigma_i^z+\sigma_j^z) + \frac{(d_1+d_0)^2}{4}\Big]. \tag{1.16}$$

Here, the first two terms describe Ising- and XY-type interactions between the two-level dipoles. The third term is equivalent to a magnetic field in z direction and the last term is a constant energy offset. Typically, we will be interested in the interaction terms in the first line. Note, however, that the "magnetic field" term and the constant offset depend on the positions of all other dipoles. If the system is not translationally invariant, these terms describe spatially dependent contributions.

Dipolar XXZ Hamiltonian: Using the spin one-half operators $S_i^\alpha = \hbar\sigma_i^\alpha/2$, we can write the interaction Hamiltonian for a system of interacting dipoles as

$$\begin{aligned} H &= \frac{1}{2}\sum_{i\neq j} H_{ij}^{\mathrm{dd}} = \sum_{i\neq j}\frac{\kappa}{\hbar^2 R_{ij}^3}\Big[\frac{(d_1-d_0)^2}{2}S_i^z S_j^z + q_1^2(S_i^x S_j^x + S_i^y S_j^y)\Big] \\ &= \frac{Ja^3}{\hbar^2}\sum_{i\neq j}\frac{\cos\theta\, S_i^z S_j^z + \sin\theta\,(S_i^x S_j^x + S_i^y S_j^y)}{R_{ij}^3} \end{aligned} \tag{1.17}$$

where we have introduced $J\cos\theta = \kappa(d_1-d_0)^2/2a^3$ and $J\sin\theta = \kappa q_1^2/a^3$ for a convenient parametrization. The length a (lattice constant) has been introduced to define an energy scale J, which will be useful for future applications. This model is reminiscent of the famous XXZ Hamiltonian, where the nearest neighbor interactions are replaced by the dipolar R_{ij}^{-3} interaction. For particular values of the θ parameter, this model describes an Ising model ($\theta = 0, \pi$), XY model ($\theta = \pm\pi/2$) or Heisenberg model ($\theta = \pi/4, 3\pi/4$). The modifications due to the dipolar interaction are subject of chapter 2 of this thesis.

Angular momentum difference: Staying in the regime of two-level dipoles, we can reach a different but related situation, if the upper state $|1\rangle$ is replaced by the $M = 1$ state $|+\rangle$, see figure 1.1b. Proceeding similarly as before, we define the relevant dipole matrix elements

$$d_0 = \langle 0|d^0|0\rangle, \quad d_+ = \langle +|d^0|+\rangle, \quad q_+ = |\langle +|d^+|0\rangle| = |\langle 0|d^-|+\rangle|. \tag{1.18}$$

Note that we can choose the phases of $|0\rangle$ and $|+\rangle$ freely, allowing us to choose real values for the transition dipole elements. Be aware, however, that $\langle 0|d^-|+\rangle = \langle +|(d^-)^\dagger|0\rangle^* = -\langle +|d^+|0\rangle^*$ due to the definition of $d^\pm$. In contrast to the previous section, the term $d_i^0 d_j^0$ only generates an interaction term proportional to $\sigma_i^z\sigma_j^z$, as the angular momentum of the two states is different. However, the term $d_i^+ d_j^-$ in the dipole-dipole interaction provides the same excitation-conserving tunneling term proportional to $\sigma^+\sigma^-$ that we got before. The different nature of the states leads to a flipped sign compared to the previous model:

$$H_{ij}^{\mathrm{dd}} = \frac{\kappa}{R_{ij}^3}\Big[\frac{(d_+ - d_0)^2}{4}\sigma_i^z\sigma_j^z - \frac{q_+^2}{2}(\sigma_i^+\sigma_j^- + \sigma_i^-\sigma_j^+) + \frac{d_+^2 - d_0^2}{4}(\sigma_i^z + \sigma_j^z) + \frac{(d_+ + d_0)^2}{4}\Big]. \tag{1.19}$$

This allows us to tune the model in equation (1.17) to different θ values.

Magnetic dipoles: As an immediate application of equation (1.19), we consider spin $S = 1/2$ atoms with a magnetic dipole moment $\mathbf{d} = \mu_{\mathrm{B}} g\boldsymbol{\sigma}/2$. Then, the dipole matrix elements are given by

$$\begin{aligned} d_0 &= \langle 0|d^0|0\rangle = -\mu_{\mathrm{B}} g/2, \\ d_+ &= \langle +|d^0|+\rangle = +\mu_{\mathrm{B}} g/2, \\ q_+ &= |\langle +|d^+|0\rangle| = \langle +|\sqrt{2}\sigma^+|0\rangle = +\mu_{\mathrm{B}} g/\sqrt{2}. \end{aligned} \tag{1.20}$$

Including the energy non-conserving terms proportional to $\sigma_i^-\sigma_j^-$, the Hamiltonian reduces to

$$H_{ij}^{\mathrm{dd}} = \frac{\kappa\mu_{\mathrm{B}}^2 g^2}{4R_{ij}^3}\left[\sigma_i^z\sigma_j^z - \left(\sigma_i^+\sigma_j^- + 3\sigma_i^-\sigma_j^-\,\mathrm{e}^{+2i\phi} + \mathrm{h.c.}\right)\right]. \tag{1.21}$$

This type of interaction between two magnetic dipoles will be utilized in chapter 3, where we make use of the dipolar relaxation terms.

1.3.2 Excitation hopping: mapping to hard-core bosons

It is often useful to think about spin models in terms of excitations above a certain well defined (ground) state [110]. As an exemplary case, we take the spin 1/2 model from equation (1.17) and write it in terms of $S^{\pm} = S_i^x \pm iS_i^y$:

$$H = \frac{Ja^3}{\hbar^2} \sum_{i \neq j} \frac{1}{R_{ij}^3} \left[\cos\theta \, S_i^z S_j^z + \frac{1}{2} \sin\theta \, (S_i^+ S_j^- + S_i^- S_j^+) \right]. \tag{1.22}$$

Assume that, for some set of parameters, the system is in the state $|G\rangle = \prod_i |\downarrow\rangle_i$ and we are interested in the excitations. Then, for each site, we can introduce the operator $b_i = S_i^-/\hbar = |\downarrow\rangle\langle\uparrow|_i$ as well as its adjoint $b_i^\dagger = S_i^+/\hbar$. These operators satisfy the commutation relation $[b_i, b_j^\dagger] = (1 - 2n_i)\delta_{ij}$, where $n_i = b_i^\dagger b_i = S_i^z/\hbar + 1/2$. For $i \neq j$, these are just bosonic commutation relations. However, on a single site, we find $b_i b_i = b_i^\dagger b_i^\dagger = 0$ and $\{b_i, b_i^\dagger\} = 1$. When interpreting $b_i^\dagger$ as the creation of a single particle (excitation) at site i, these equations formalize the so-called hard core constraint: only a single excitation can be present at each site. Keeping the constraint in mind, we can treat these operators as bosonic creation and annihilation operators for single excitations above the vacuum $|G\rangle$ with $b_i |G\rangle = 0$ and write the model as

$$H = J \sum_{i \neq j} \frac{a^3}{R_{ij}^3} \left[\cos\theta \, n_i n_j + \frac{1}{2} \sin\theta \left(b_i^\dagger b_j + b_i b_j^\dagger \right) \right]. \tag{1.23}$$

For a detailed treatment, see chapter 2 and appendix B. In the following, we will extend this idea to dipoles with more than two internal states.

1.3.3 Three-level dipoles: appearance of spin-orbit coupling

First, we investigate a V-type level scheme including three internal states of a dipole, $|0\rangle$, $|+\rangle$ and $|-\rangle$, as shown in figure 1.1b. The relevant dipole matrix elements are

$$d_0 = \langle 0|d^0|0\rangle, \qquad d_\pm = \langle \pm|d^0|\pm\rangle, \qquad q_\pm = |\langle \pm|d^\pm|0\rangle|. \tag{1.24}$$

As before, we define a vacuum state $|G\rangle = \prod_i |0\rangle_i$ as well as hardcore bosonic operators $b_\pm = |0\rangle\langle\pm|$ and $n_\pm = b_\pm^\dagger b_\pm$. We can either think of two different kinds of bosons ('+' excitations and '−' excitations) or think of a single boson with an internal spin degree of freedom. It is useful to write the spherical

components of the dipole operator in terms of the bosonic operators:

$$\begin{aligned} d^0 &= d_+ n_+ + d_- n_- + d_0(1 - n_+ - n_-) \\ &= d_0 + (d_+ - d_0)n_+ + (d_- - d_0)n_-, \\ d^+ &= q_+ b_+^\dagger - q_- b_-, \\ d^- &= -q_+ b_+ + q_- b_-^\dagger. \end{aligned} \tag{1.25}$$

Restricting ourselves to a two-dimensional geometry with a perpendicular polarization, we can express the relevant parts of the dipole-dipole interaction from equation (1.6) as

$$\begin{aligned} d_i^0 d_j^0 &= d_0^2 + d_0(d_+ - d_0)(n_{+,i} + n_{+,j}) + d_0(d_- - d_0)(n_{-,i} + n_{-,j}) \\ &\quad + (d_+ - d_0)^2 n_{+,i} n_{+,j} + (d_- - d_0)^2 n_{-,i} n_{-,j} \\ &\quad + (d_+ - d_0)(d_- - d_0)(n_{+,i} n_{-,j} + n_{-,i} n_{+,j}) \\ d_i^+ d_j^- &= -q_+^2 b_{+,i}^\dagger b_{+,j} - q_-^2 b_{-,j}^\dagger b_{-,i} \\ d_i^+ d_j^+ &= -q_+ q_- (b_{+,i}^\dagger b_{-,j} + b_{+,j}^\dagger b_{-,i}) \end{aligned} \tag{1.26}$$

where we have neglected any excitation non-conserving terms. Further dropping the constant terms and "magnetic field" terms, we find the many-body Hamiltonian

$$H = \frac{1}{2} \sum_{i \neq j} H_{ij}^{\mathrm{dd}} = \sum_{i \neq j} t_{ij}^{\alpha\beta} b_{\alpha,i}^\dagger b_{\beta,j} + \frac{1}{2} \sum_{i \neq j} V_{ij}^{\alpha\beta} n_{\alpha,i} n_{\beta,j}. \tag{1.27}$$

Here, a summation over the α, β indices, which label the internal state of the excitation, is assumed. This is a (generalized) hard core Bose-Hubbard Hamiltonian, including long-range hopping terms and long-range density-density interactions. In our case, the tunneling rates and interaction matrix elements are given by

$$\begin{aligned} t_{ij} &= \frac{\kappa}{R_{ij}^3} \begin{pmatrix} -\frac{q_+^2}{2} & \frac{3q_+q_-}{2} \mathrm{e}^{-2i\phi_{ij}} \\ \frac{3q_+q_-}{2} \mathrm{e}^{+2i\phi_{ij}} & -\frac{q_-^2}{2} \end{pmatrix}, \\ V_{ij}^{\alpha\beta} &= \frac{\kappa}{R_{ij}^3} (d_\alpha - d_0)(d_\beta - d_0). \end{aligned} \tag{1.28}$$

By introducing the lattice spacing a, we can define the nearest-neighbor tunneling rates

$$t^+ = \frac{\kappa q_+^2}{2a^3}, \qquad t^- = \frac{\kappa q_-^2}{2a^3}, \qquad w = \frac{3\kappa q_+ q_-}{2a^3}. \tag{1.29}$$

Using these, the single-particle tunneling part of the Hamiltonian can be written as

$$H_{\text{single}} = \sum_{i \neq j} \frac{a^3}{R_{ij}^3} \begin{pmatrix} b_{i,+} \\ b_{i,-} \end{pmatrix}^\dagger \begin{pmatrix} -t^+ & w\,\mathrm{e}^{-2i\phi_{ij}} \\ w\,\mathrm{e}^{2i\phi_{ij}} & -t^- \end{pmatrix} \begin{pmatrix} b_{j,+} \\ b_{j,-} \end{pmatrix}. \tag{1.30}$$

This model is the basis for the realization of topological band structures in chapters 4 and 5. The off-diagonal tunneling elements are a manifestation of the spin-orbit coupling which is present in these dipolar models.

One-dimensional system: In one dimension, we can always choose $\phi_{ij} = 0$. Furthermore, if $q_+ = q_-$, the tunneling elements simplify to

$$t_{ij} = \frac{\kappa q^2}{2R_{ij}^3}(3\sigma_x - \mathbb{1}). \tag{1.31}$$

By transforming to $|x\rangle = (|+\rangle - |-\rangle)/\sqrt{2}$ and $|y\rangle = (|+\rangle + |-\rangle)/\sqrt{2}$, the tunneling part can be diagonalized:

$$t_{ij} = \frac{\kappa q^2}{R_{ij}^3} \begin{pmatrix} -2 & 0 \\ 0 & 1 \end{pmatrix}. \tag{1.32}$$

If the energy of the $|x\rangle, |y\rangle$ manifold is low enough compared to the $|0\rangle$ state, this causes excitations to condense in the $|x\rangle$ state, building a ferroelectric state of matter. The accompanying quantum phase transition has been investigated by Klinsmann et al. [P5, 111].

1.3.4 General case: four level dipoles in a tilted external field

Finally, we briefly discuss the most general case when all four states in figure 1.1b are involved. We assume the geometry from figure 1.1a with a possibly tilted external field. Introducing a bosonic operator $b_1 = |1\rangle\langle 0|$ for the additional state, we can write the tunneling rates in the basis $\{+, 1, -\}$:

$$t_{ij} = \frac{\kappa}{R_{ij}^3} \begin{pmatrix} -\frac{q_+^2}{2} f_0 & \frac{3q_+q_1}{\sqrt{2}} f_1^* & \frac{3q_+q_-}{2} f_2^* \\ \frac{3q_+q_1}{\sqrt{2}} f_1 & q_1^2 f_0 & -\frac{3q_1q_-}{\sqrt{2}} f_1^* \\ \frac{3q_+q_-}{2} f_2 & -\frac{3q_1q_-}{\sqrt{2}} f_1 & -\frac{q_-^2}{2} f_0 \end{pmatrix}. \tag{1.33}$$

Here, $f_m = f_m(\Theta_0, \phi_{ij} - \Phi_0)$ are the functions defined in equation (1.12). Note that $f_1(\Theta_0, \phi_{ij} - \Phi_0) = 0$ for an external field which is perpendicular to the two-dimensional plane ($\Theta = 0$). This leads to an effective decoupling of the $|1\rangle$ state from the other two, taking us back to the model in equation (1.30).

2

Anomalous behavior of dipolar spin systems

The foundation for understanding the behavior and properties of quantum matter is based on models with short range interactions. Experimental progress in realizing dipolar spin systems has however increased the interest in systems with strong dipole-dipole interactions. While many properties of quantum systems with dipole-dipole interactions derive from our understanding of systems with short range interactions, the dipole-dipole interaction can give rise to phenomena not present in their short range counterparts. Prominent examples are the description of dipolar Bose-Einstein condensates, where the contribution of the dipolar interaction can not be included in the s-wave scattering length [70], and the absence of a first order phase transition with a jump in the density [112]. In this chapter, we demonstrate that two-dimensional spin systems with dipolar interactions can exhibit anomalous behavior.

A remarkable property of cold polar molecules confined into two dimensions is the potential formation of a crystalline phase for strong dipole-dipole interactions [113, 114]. In contrast to a Wigner crystal with Coulomb interactions [115], the crystalline phase exhibits the conventional behavior expected for a crystal realized with a short range repulsion and the characteristic $1/r^3$ behavior of the dipole interaction can be truncated at distances involving several inter-particle separations. Several strongly correlated phases have been predicted, which behave in analogy to systems with interactions extending over a finite range,

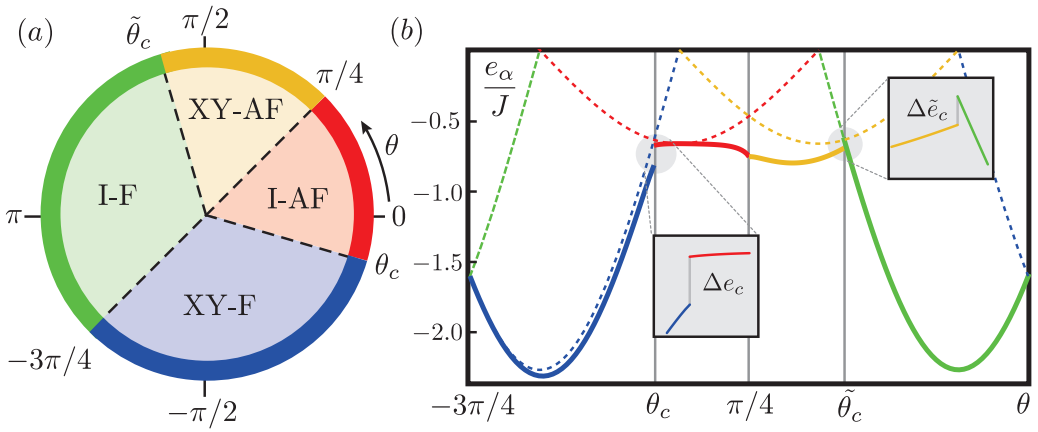

Fig. 2.1: (a) Mean-field phase diagram for the XXZ model with dipolar interactions, where $\tan\theta$ is the ratio between the XY and the Ising spin couplings. **(b)** Ground state energy per particle: the dashed lines show the mean-field predictions, while the solid lines include the contributions from the spin waves. At the critical values θ_c and $\tilde{\theta}_c$, the ground state energy exhibits the jump $\Delta e_c \approx 0.14J$ and $\Delta\tilde{e}_c \approx 0.06J$, indicating the potential formation of an intermediate phase.

such as a Haldane phase [116], supersolids [117, 118], pair supersolids in bilayer systems [119], valence bond solids [120], as well as p-wave superfluidity [121], and self-assembled structures in multi-layer setups [122].

On the other hand, it has been demonstrated that polar molecules in optical lattices are also suitable for emulating quantum phases of two-dimensional spin models [71, 73, 108]. Here, we demonstrate that such spin models with dipole-dipole interactions exhibit several anomalous features, which are not present in their short-range counterparts.

2.1 Dipolar XXZ model

We consider a two-dimensional setup on a square lattice, where each lattice site is occupied by one dipolar particle. We focus on models with two internal degrees of freedom, such that we can define a spin $1/2$ system. Then, as demonstrated in equation (1.17) on page 22, the Hamiltonian reduces to a XXZ model with dipole-dipole interaction between the spins [73, 123]:

$$H = \frac{Ja^3}{\hbar^2} \sum_{i \neq j} \frac{\cos\theta\, S_i^z S_j^z + \sin\theta\, (S_i^x S_j^x + S_i^y S_j^y)}{|\mathbf{R}_i - \mathbf{R}_j|^3}. \tag{2.1}$$

Here, the first term with strength $J\cos\theta$ accounts for the static dipole-dipole interaction between the different internal levels, while the last term with strength $J\sin\theta$ describes the virtual exchange of a photon between the two spins. The constant a denotes the lattice spacing. The dependence of the couplings J and θ on the microscopic parameters is discussed in detail in section 1.3.1 and related works by Müller [124] and Gorshkov et al. [73, 108]. The one-dimensional version of this model has been studied in [72].

2.2 Mean-field theory

Before analyzing this spin model on the square lattice, we shortly discuss the phase diagram of its counterpart with nearest neighbor interactions only. In this case, the phase diagram is highly symmetric and exhibits four different phases:

(I-AF) $-\pi/4 < \theta < \pi/4$
Ising antiferromagnetic phase with excitation gap

(XY-AF) $\pi/4 < \theta < 3\pi/4$
XY antiferromagnetic phase with linear excitation spectrum

(I-F) $3\pi/4 < \theta < 5\pi/4$
Ising ferromagnetic phase with excitation gap

(XY-F) $5\pi/4 < \theta < 7\pi/4$
XY ferromagnetic phase with linear excitation spectrum

The modifications of the phase diagram due to dipole-dipole interactions between the spins can be analyzed within mean-field theory. The main influence is the reduction of the stability for the antiferromagnetic phases, as the next-nearest neighbor interaction introduces a weak frustration to the system. The ground state energy per lattice site within mean-field reduces to $e_{\text{I-AF}} = J\cos\theta\,\epsilon_{\mathbf{K}}/4$ and $e_{\text{XY-AF}} = J\sin\theta\,\epsilon_{\mathbf{K}}/4$ for the antiferromagnetic phases. The summation over the dipole interaction comes down to a dimensionless parameter $\epsilon_{\mathbf{K}} \approx -2.646$, which is related to the dipolar dispersion [P1, P6, 75, 124]

$$\epsilon_{\mathbf{q}} = \sum_{j\neq 0} e^{i\mathbf{q}\mathbf{R}_j} \frac{a^3}{|\mathbf{R}_j|^3} \tag{2.2}$$

GS α	spin wave excitation spectrum $E^\alpha_{\mathbf{q}}$	ground state energy per spin e_α
I-F	$J(\sin\theta\,\epsilon_{\mathbf{q}} - \cos\theta\,\epsilon_0)$	$\frac{3J\cos\theta\,\epsilon_0}{4} + \frac{1}{2}\int\frac{\mathrm{d}\mathbf{q}}{v_0}\,E^\alpha_{\mathbf{q}} = \frac{J\cos\theta\epsilon_0}{4}$
XY-F	$J\sqrt{\sin\theta\,(\epsilon_{\mathbf{q}} - \epsilon_0)(\cos\theta\,\epsilon_{\mathbf{q}} - \sin\theta\,\epsilon_0)}$	$\frac{3J\sin\theta\,\epsilon_0}{4} + \frac{1}{2}\int\frac{\mathrm{d}\mathbf{q}}{v_0}\,E^\alpha_{\mathbf{q}}$
I-AF	$J\sqrt{(\sin\theta\,\epsilon_{\mathbf{q}+\mathbf{K}} - \cos\theta\,\epsilon_{\mathbf{K}})(\sin\theta\,\epsilon_{\mathbf{q}} - \cos\theta\,\epsilon_{\mathbf{K}})}$	$\frac{3J\cos\theta\,\epsilon_{\mathbf{K}}}{4} + \frac{1}{2}\int\frac{\mathrm{d}\mathbf{q}}{v_0}\,E^\alpha_{\mathbf{q}}$
XY-AF	$J\sqrt{\sin\theta\,(\epsilon_{\mathbf{q}+\mathbf{K}} - \epsilon_{\mathbf{K}})(\cos\theta\,\epsilon_{\mathbf{q}} - \sin\theta\,\epsilon_{\mathbf{K}})}$	$\frac{3J\sin\theta\,\epsilon_{\mathbf{K}}}{4} + \frac{1}{2}\int\frac{\mathrm{d}\mathbf{q}}{v_0}\,E^\alpha_{\mathbf{q}}$

Table 2.1: Spin wave excitation spectrum $E^\alpha_{\mathbf{q}}$ and ground state energy e_α.

at the corner of the Brillouin zone with $\mathbf{K} = (\pi/a, \pi/a)$. Conversely, the ferromagnetic phases are enhanced with a mean-field energy $e_{\text{I-F}} = J\cos\theta\,\epsilon_0/4$ and $e_{\text{XY-F}} = J\sin\theta\,\epsilon_0/4$ where $\epsilon_0 \approx 9.033$. The modifications to the phase diagram are shown in figure 2.1: first, the Heisenberg points at $\theta = \pi/4, 5\pi/4$ are protected by the SU(2) symmetry and still provide the transition between the Ising and the XY phases. However, the transitions from the ferromagnetic towards the antiferromagnetic phases are shifted to the values $\theta_c = \arctan(\epsilon_{\mathbf{K}}/\epsilon_0) \approx -0.1\pi$ and $\tilde{\theta}_c = \pi + \arctan(\epsilon_0/\epsilon_{\mathbf{K}}) \approx 0.6\pi$.

The dipole dispersion $\epsilon_{\mathbf{q}}$ in equation (2.2) converges very slowly due to the characteristic power law decay of the dipole-dipole interaction. It is this slow decay, which will give rise to several peculiar properties of the system. Therefore, we continue first with a detailed discussion of this dipolar dispersion. The precise determination of $\epsilon_{\mathbf{q}}$ is most conveniently performed using an Ewald summation [115, 124], which transforms the summation over the slowly converging terms with algebraic decay into a summation of exponential factors. The complete derivation is given in section A.4. The main result is equation (A.22) with

$$\begin{aligned}\epsilon_{\mathbf{q}} = &-2\pi a|\mathbf{q}|\,\mathrm{erfc}(a|\mathbf{q}|/2\sqrt{\pi}) + 4\pi\left(e^{-\frac{a^2|\mathbf{q}|^2}{4\pi}} - \frac{1}{3}\right)\\ &+ 2\pi\sum_{i\neq 0}\int_1^\infty \mathrm{d}\lambda\,\lambda^{3/2}\left[e^{-\pi\lambda\left(\frac{\mathbf{R}_i}{a}+\frac{a\mathbf{q}}{2\pi}\right)^2} + \lambda^2 e^{-\frac{\pi\lambda|\mathbf{R}_i|^2}{a^2}+i\mathbf{R}_i\mathbf{q}}\right]\end{aligned} \tag{2.3}$$

where $\mathrm{erfc}(x)$ the complementary error function. The important feature of the dipole dispersion is captured by the first term in equation (2.3), which gives

rise to a linear and non-analytic behavior $\epsilon_{\mathbf{q}} \sim \epsilon_0 - 2\pi a|\mathbf{q}|$ for small values $|\mathbf{q}| \ll 1/a$, while all remaining terms are analytic. It is this linear part, which will give rise to several unconventional properties of spin systems in 2D with dipolar interactions, and is a consequence of the slow decay of the dipole-dipole interaction. The summation in the last term converges exponentially and guarantees the periodicity of the dipolar dispersion. The quantitative behavior is shown in figure 2.2a. For $\mathbf{q} = 0$ and $\mathbf{q} = \mathbf{K}$, exact results can be derived, giving $\epsilon_0 \approx 9.033$ and $\epsilon_{\mathbf{K}} = (1/\sqrt{2} - 1)\epsilon_0 \approx -2.646$ (details in section A.4.1).

2.3 Spin-wave analysis

Next, we analyze the excitation spectrum above the mean-field ground states within a spin wave analysis. This theory is well established [125, 126], and its application for a spin system with dipolar interaction is straightforward. It allows for the full treatment of the $1/r^3$ tail of the dipole-dipole interactions. The details of the calculation for one specific case (the antiferromagnetic XY model) are presented in appendix B. The results are summarized in table 2.1, and shown in figure 2.2. In the following, we present a detailed discussion for each of the four ordered phases.

2.3.1 Ising ferromagnetic phase

The ferromagnetic mean-field ground state is twofold degenerate with all spins either pointing up or down, and is the exact ground state for $\theta = \pi$, i.e., $|G\rangle = \prod_i |\downarrow\rangle_i$. Within the spin wave analysis, the ground state is not modified and the excitation spectrum reduces to $E^{\text{I-F}}_{\mathbf{q}}$, see table 2.1. The spin waves exhibit an excitation gap Δ: (i) approaching the Heisenberg point at $\theta = -3\pi/4$, the excitation gap vanishes, indicating the instability towards the XY ferromagnet, (ii) in turn, for antiferromagnetic XY couplings, the gap is minimal at $\mathbf{K}$, vanishes at the mean-field transition point $\tilde{\theta}_c$ and drives an instability towards the formation of antiferromagnetic ordering.

In contrast to any short range ferromagnetic spin model, the dispersion relation $E^{\text{I-F}}_{\mathbf{q}}$ is not quadratic for small momenta, but rather exhibits a linear behavior, i.e., $E^{\text{I-F}}_{\mathbf{q}} \sim E^{\text{I-F}}_0 + \hbar c|\mathbf{q}|$ with velocity $c = -2\pi a J \sin\theta/\hbar$, which is a consequence of the dipolar interaction in the system. This anomalous behavior strongly influences the dynamics of the spin waves. The dynamical behavior of a single localized spin excitation is shown in figure 2.3a for a Gaussian initial state. In order to

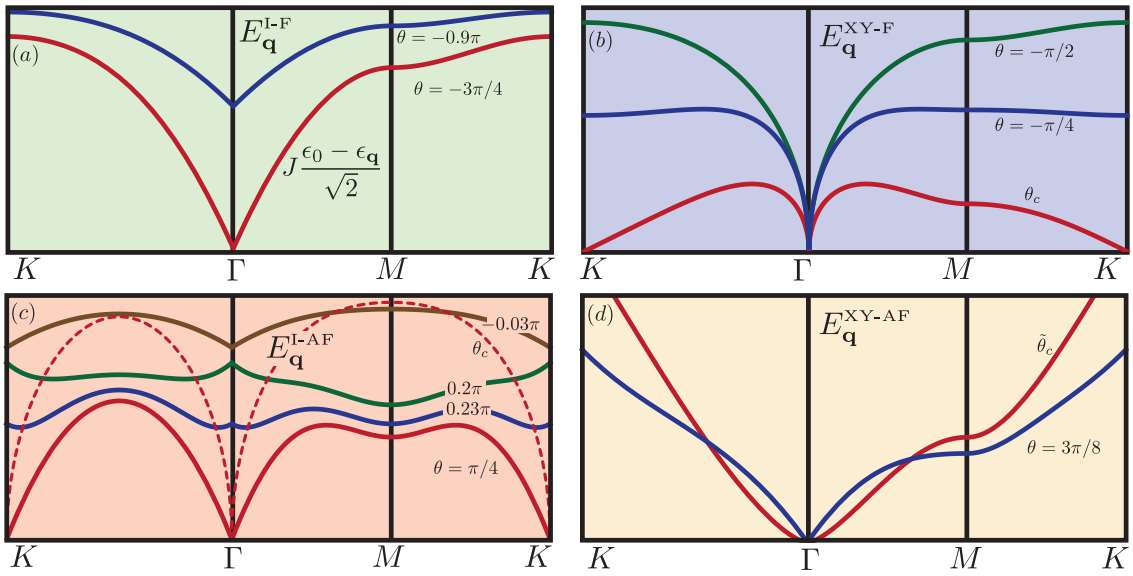

Fig. 2.2: Spin wave excitations with $\Gamma = (0,0)$, $M = (0,\pi/2)$, and $K = (\pi/a, \pi/a)$ for different θ angles. **(a)** Spectrum of the I-F phase which also shows the behavior of the dipolar dispersion $\epsilon_{\mathbf{q}}$ for $\theta = -3\pi/4$, see red line. **(b-d)** Spectrum for the XY-F, I-AF and XY-AF phases. Each red line is a critical excitation spectrum indicating an instability.

probe the linear part in the dispersion relation, the width σ of the localization is much larger than the lattice spacing a, and therefore, the dynamics is well described by a continuum description. Instead of the conventional quantum mechanical spreading, one finds a ballistic expansion of a cylindrical wave packet with velocity c. In addition, the dipole-dipole interaction also strongly influences the correlation function. Within conventional perturbation theory, we find algebraic correlations $\langle S_i^x S_j^x \rangle \sim 1/|\mathbf{r}|^3$. This algebraic decay of correlations even in gapped systems is a peculiar property of spin models with long-range interactions [127, 128].

2.3.2 XY-ferromagnetic phase

Here, the spins are aligned in the xy plane. Within the spin wave analysis, we obtain the excitation spectrum $E_{\mathbf{q}}^{\text{XY-F}}$ and the modified ground state energy $e_{\text{XY-F}}$. In the low momentum regime, the dispersion relation behaves as $E_{\mathbf{q}}^{\text{XY-F}} \sim \sqrt{|\mathbf{q}|}$, in contrast to the well known linear Goldstone modes for the broken $U(1)$ symmetry. This anomalous behavior is a peculiar property of the dipolar interaction, and the most crucial consequence is the existence of long-range

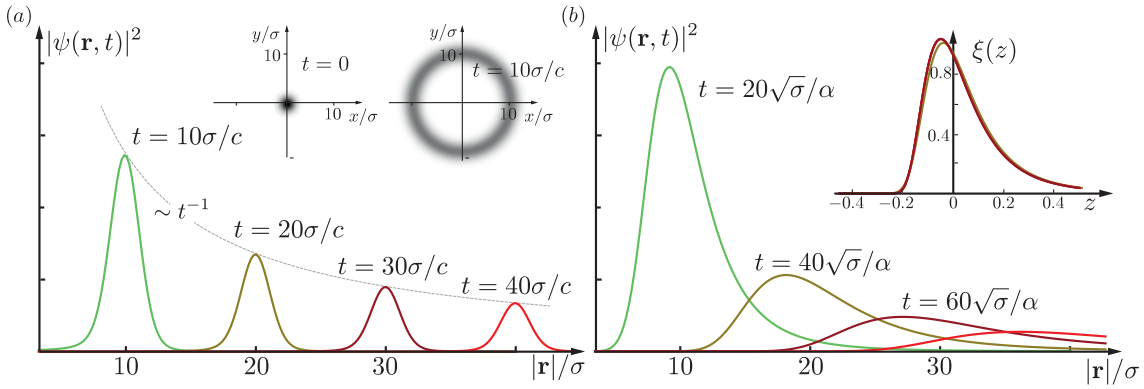

Fig. 2.3: Time evolution for localized spin excitations described by the Gaussian wave packet $\psi_0(\mathbf{r}) = e^{-|\mathbf{r}|^2/2\sigma^2}/\sqrt{\pi\sigma^2}$ with $\sigma \gg a$ in the continuum description. **(a)** For a linear dispersion $c|\mathbf{q}|$ in the I-F phase, the dynamics is described by cylindrical symmetric wave packets (see inset) traveling with velocity c, instead of the conventional quantum mechanical spreading for massive systems. **(b)** For an anomalous dispersion with $\alpha\sqrt{|\mathbf{q}|}$ in the XY-F phase, the behavior at long times $t \gg \sqrt{\sigma}\alpha$ reduces to a scaling function $\xi(z)$ via $|\psi(x,\tau)|^2 = \xi(x/\tau - 1/2)/\tau^2$ (see inset) using rescaled time $\tau = t\alpha/\sqrt{\sigma}$ and space $x = |\mathbf{r}|/\sigma$ coordinates. It describes a cylindrical symmetric wave front with velocity $\alpha\sqrt{\sigma}$.

order for the continuous broken symmetry at finite temperatures even in two-dimensions [129]. This property follows immediately from the above spin wave analysis: the order parameter reduces to $m \equiv \Delta m - 1/2 = \langle S_i^x \rangle/\hbar$, where Δm accounts for the suppression of the order parameter by quantum fluctuations. Within spin wave theory, it reduces to ($\Delta m = \langle a_i^\dagger a_i \rangle$)

$$\Delta m = \int \frac{\mathrm{d}\mathbf{q}}{v_0} \left[\frac{\cos\theta\, \mathbf{q} + \sin\theta(\epsilon_{\mathbf{q}} - 2\epsilon_0)}{4E_{\mathbf{q}}} \coth\left(\frac{E_{\mathbf{q}}}{2T}\right) - \frac{1}{2} \right]. \tag{2.4}$$

This expression is finite and small: at $T = 0$, the integrand behaves as $\sim 1/\sqrt{|\mathbf{q}|}$ and we find a suppression of the order $\Delta m \approx 0.008$ at $\theta = -\pi/2$. The smallness of this corrections due to quantum fluctuations is a good justification for the validity of the spin wave analysis. On the other hand, even at finite temperatures, the low momentum behavior of the integrand takes the form $\sim T/|\mathbf{q}|$, and provides a finite contribution in contrast to a conventional Goldstone mode, which provides a logarithmic divergence.

The appearance of a long-range order at a finite temperature for a ground state with a broken $U(1)$ symmetry is a peculiar feature of dipole-dipole interactions, which renders the system more mean-field like. Note that this finding is

correlation function	$T = 0$	$0 < T < T_c$	$T_c < T$
$\langle S_i^z S_j^z \rangle$	$\sim \lvert\mathbf{r}\rvert^{-5/2}$	$\sim \lvert\mathbf{r}\rvert^{-3}$	$\sim \lvert\mathbf{r}\rvert^{-3}$
$\langle S_i^y S_j^y + S_i^x S_j^x \rangle - m^2$	$\sim \lvert\mathbf{r}\rvert^{-3/2}$	$\sim \lvert\mathbf{r}\rvert^{-1}$	$\sim \lvert\mathbf{r}\rvert^{-3}$

Table 2.2: Correlation functions in the XY-F phase predicted by the spin wave analysis and high temperature expansion.

consistent with the well-known Mermin-Wagner theorem as the latter does not exclude long-range order for interactions with a $1/r^\alpha$ tail, where $\alpha \leq 4$ [130, 131]. The system exhibits a finite temperature transition into a disordered phase at a critical temperature T_c. This behavior is also expected from the analysis of the classical XY model with dipolar interactions [129]. The correlation functions determined within spin wave theory and through a high temperature expansion are summarized in table 2.2. For details, see appendices B and C. Note that the spin wave analysis neglects the influence of vortices. This is well justified here, as the dipolar interactions gives rise to a confining of vortices, i.e., the interaction potential between a vortex–anti-vortex pair increases linearly with the separation between the vortices.

The spin wave dynamics caused by the anomalous dispersion relation $\sim \sqrt{|\mathbf{q}|}$ are shown in figure 2.3b for a Gaussian wave packet of width σ. Interestingly, the propagation velocity of the wave packets is proportional to $\sqrt{\sigma}$ and thus faster for broad wave packets, in contrast to the usual dispersion dynamics. This is a consequence of the group velocity $v_\mathbf{q} \sim 1/\sqrt{|\mathbf{q}|}$ which is large for the small momentum components involved in the broad wave packets.

2.3.3 Ising antiferromagnetic phase

Next, we focus on the antiferromagnetic phases and start with the I-AF ground state. Again, the ground state is two-fold degenerate on bipartite lattices. We choose the ground state with spin up on sublattice A and spin down on sublattice B, i.e., $|G\rangle = \prod_{i\in A} |\uparrow\rangle_i \prod_{j\in B} |\downarrow\rangle_j$. The spin wave analysis is straightforward, and we obtain the spin wave excitation spectrum $E_\mathbf{q}^{\text{I-AF}}$ and ground state energy $e_{\text{I-AF}}$, see table 2.1. The system exhibits an excitation gap as expected for a system with a broken Z_2 symmetry. However, the dipole interactions give rise to an anomalous behavior at small momenta similar to the ferromagnetic Ising phase with $E_\mathbf{q}^{\text{I-AF}} - E_0^{\text{I-AF}} \sim -\sin\theta\,|\mathbf{q}|$. Consequently, the dynamics of spin waves at

low momenta is analogous to the Ising-ferromagnet, see figure 2.3. Within spin wave theory, we obtain that the antiferromagnetic correlations $\langle(-1)^{i-j}S_i^\beta S_j^\beta\rangle$ and the ferromagnetic correlations $\langle S_i^\beta S_j^\beta\rangle$ decay with the power law $\sim 1/|\mathbf{r}|^3$ with $\beta = x, y, z$ determined by the characteristic behavior of the dipole-dipole interaction. The excitation gap vanishes approaching the mean field critical point θ_c towards XY- ferromagnetic phase, and also approaching the Heisenberg point at $\theta = \pi/4$. For the latter, the qualitative behavior of the excitation spectrum changes drastically within a very narrow range of θ, see figure 2.2c.

2.3.4 XY antiferromagnetic phase

Finally, we analyze the properties of the antiferromagnetic XY phase. In contrast to the ferromagnetic XY phase, the excitation spectrum $E_{\mathbf{q}}^{\text{XY-AF}}$ exhibits the conventional linear Goldstone mode, see figure 2.2d. This can be understood, as the antiferromagnetic ordering introduces a cancellation of the dipolar interactions, and provides a behavior in analogy to its short range counter part: true long-range order exists only at $T = 0$, while at finite temperature the system exhibits quasi long-range order and eventually undergoes a Kosterlitz-Thouless transition for increasing temperature. Nevertheless, the dipole-dipole interactions give rise to the characteristic algebraic correlations, e.g., $\langle(-1)^{i-j}S_i^z S_j^z\rangle \sim 1/|\mathbf{r}|^3$ for the antiferromagnetic transverse spin correlation at zero temperature.

2.4 Phase transitions

Finally, we comment on the transitions between the different phases. The spin wave analysis predicts, that the excitation spectrum for each phase becomes unstable at the mean-field critical points: For the Heisenberg points at $\theta = \pi/4, 5\pi/4$, such a behavior is expected due to the enhanced symmetry and one indeed finds, that at the critical point, the excitation spectrum from the Ising phase coincides with the spectrum from the XY ground state. Consequently, the spin waves provide the same contribution to the ground state energy, see figure 2.1b. In turn, at the instability points θ_c and $\tilde{\theta}_c$, the excitation spectrum of the antiferromagnetic phase is different from the spectrum of the ferromagnetic phase. Consequently, the ground state energy within the spin wave analysis exhibits a jump, see figure 2.1a. Such a behavior is an indication for the appearance of an intermediate phase. However, this question can not be conclusively answered within the presented analysis due to the limited validity

of spin wave theory close to the transition points. However, the appearance of a first order phase transition can be excluded by arguments similar to the one used by Spivak and Kivelson [112].

3

Driving dipolar fermions into the Quantum Hall regime

Despite being ideal models for complicated solid state systems, ultracold quantum gases lack one important aspect of the electronic complex: because of the charge neutrality of the atoms, there are no mobile charge carriers that possess a direct coupling to the magnetic vector potential. Plenty of interesting effects, however, arise when charged particles are subject to high magnetic fields in low dimensional systems. The most prominent ones are the integer quantum Hall effect [7], as well as the fractional quantum Hall effect [21] as an example for the appearance of a topological state, potentially giving rise to fundamental excitations with non-Abelian statistics.

Several schemes have been proposed to simulate the effect of magnetic fields for neutral particles. Artificial gauge fields can be created by imprinting phases, making use of the Peierls substitution in optical lattices [36, 40, 132], or by tailoring spatially dependent Hamiltonians to generate geometric phases [133], for an overview see Dalibard et al. [134]. Rapidly rotating quantum gases provide an alternative route via Larmor's theorem, using the analogy between a charged particle in a constant magnetic field and a neutral particle in a rotating frame [30, 31]. Several theoretical proposals demonstrate the appearance of highly correlated quantum Hall states for dipolar bosons [135] and fermions [136, 137]. However, the experimental realization of quantum Hall states has been elusive so far. For rotating systems, the main problem is the precise control

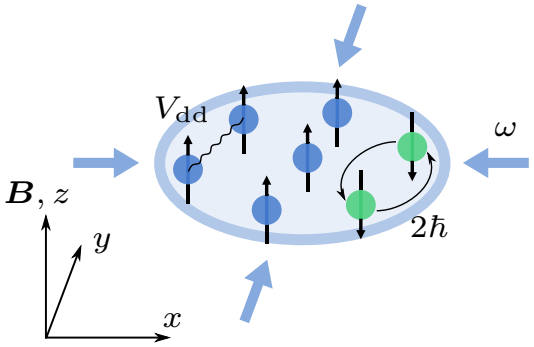

Fig. 3.1: Dipolar particles, trapped in a quasi-2D geometry with a radial confinement ω. When the external magnetic field $\mathbf{B}$ is tuned in resonance, dipolar interactions V_{dd} can induce spin relaxation processes, leading to a net angular momentum increase of $1\hbar$ per particle.

on the rotation frequency, which is required to reach the lowest Landau level without crossing the rotational instability [28].

We propose a new scheme to access the regime of fast rotation for a dipolar Fermi gas such as ^{161}Dy or ^{167}Er, where quantum degeneracy has been demonstrated recently [88, 90]. Starting from a spin-polarized state, dipolar interactions can lead to spin relaxation with a net angular momentum transfer [91]. This is known as the Einstein–de Haas effect [138] and has been proposed to create rotating Bose-Einstein condensates [139, 140]. We suggest to use this mechanism in a trapped, quasi-two-dimensional system to control the amount of angular momentum, and – by repeated application of the transfer scheme – reach the lowest Landau level (LLL). This scheme allows for direct control over the total angular momentum instead of the rotation frequency and circumvents the prime experimental difficulties toward the realization of the quantum Hall regime in harmonically trapped gases.

3.1 Setup

We consider a system of N fermionic atoms with magnetic dipole moments $\mathbf{d}$. While extensions to schemes with polar molecules are possible, the permanent dipole moments of the atoms lead to some simplifications. To shorten the discussion, we consider only two internal levels (pseudospin 1/2). The particles are confined in a quasi-two-dimensional harmonic trap with a radial frequency ω and an axial frequency ω_z. For strong z confinement $\hbar\omega_z \gg E_{\mathrm{F}}$, where E_{F} is the Fermi energy derived below, the system is effectively two dimensional, see figure 3.1. The interactions between the particles are described by the

dipolar interaction potential in equation (1.1)

$$V_{\mathrm{dd}}(\mathbf{R}) = \frac{\kappa}{|\mathbf{R}|^3}\left[\mathbf{d}_i \cdot \mathbf{d}_j - 3(\mathbf{d}_i \cdot \hat{\mathbf{R}})(\mathbf{d}_j \cdot \hat{\mathbf{R}})\right] \tag{3.1}$$

where $\mathbf{R} = \mathbf{R}_i - \mathbf{R}_j$ is the relative distance between the two particles. Note that a weak s-wave scattering length does not change the general behavior of our transfer scheme and is ignored in the following. For two internal levels, we can write the dipole moment $\mathbf{d} = \mu_{\mathrm{B}} g \mathbf{S}/\hbar = \mu_{\mathrm{B}} g \boldsymbol{\sigma}/2$ in terms of the Landé factor g and the Pauli matrices $\boldsymbol{\sigma}$.

3.2 The transfer process

In two dimensions, using the spin raising and lowering operators $\sigma^{\pm} = (\sigma^x \pm i\sigma^y)/2$, the interaction between these two-level dipoles reduces to

$$V_{\mathrm{dd}}(R,\phi) = \frac{C_{\mathrm{dd}}}{R^3}\left[\sigma_i^z\sigma_j^z - (\sigma_i^+\sigma_j^- + 3\,\mathrm{e}^{2i\phi}\,\sigma_i^-\sigma_j^- + \mathrm{h.c.})\right], \tag{3.2}$$

which is the expression given in equation (1.21) on page 23. Here, R and ϕ are polar coordinates in the xy plane and $C_{\mathrm{dd}} = \kappa\mu_{\mathrm{B}}^2 g^2/4$ characterizes the strength of the interaction. Note that this expression can also be derived from the full interaction (3.1) by integrating out the fast motion perpendicular to the xy plane in the limit $\omega_z \to \infty$.

The dipolar interaction features three different processes. The first term proportional to $\sigma_i^z\sigma_j^z$ describes spin-preserving collisions, while the second term $\sigma_i^+\sigma_j^-$ accounts for spin-exchange collisions. These terms conserve separately the total spin and the total angular momentum. Finally, the third operator $\mathrm{e}^{2i\phi}\,\sigma_i^-\sigma_j^-$ describes the relaxation process that transfers spin to orbital angular momentum, see figure 3.2a,b. The sum $L + S$ is still conserved and the spin flip leads to an orbital motion with an increase of relative angular momentum of $2\hbar$.

It is this process that allows us to drive the dipolar particles to higher angular momentum states. Assuming the gas is initially in a spin-polarized state with the external magnetic field pointing in the positive z direction, the particles will undergo spin relaxation when the field is adiabatically ramped through zero and finally pointing in the negative z direction. During this adiabatic ramping, the total orbital angular momentum is increased by $N\hbar$ with N the number of particles in the system. For the goal to reach the lowest Landau level regime, it is required to transfer $L^\star \equiv N(N-1)/2 \cdot \hbar$ angular momentum to the orbital

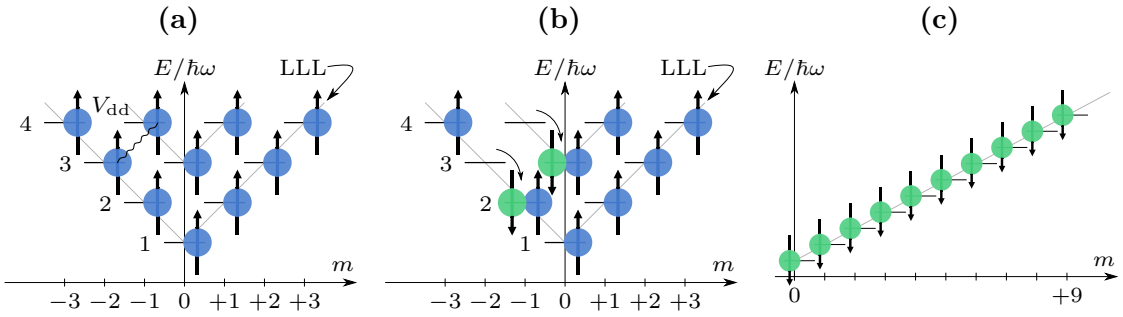

Fig. 3.2: **(a)** Energy levels of a 2D harmonic oscillator. **(b)** One of the possible spin-flip processes, bringing both particles to higher angular momentum states. **(c)** Eventually, after repeated application of the driving scheme, all particles occupy the lowest Landau level.

degrees of freedom, as described below. It is therefore necessary to reverse the magnetic field and the spins to their original position, in a way that guarantees repeated application of the transfer scheme without affecting the orbital angular momentum.

To achieve this, we propose rotating the magnetic field by 180° around an arbitrary axis lying in the xy plane (say, the y axis), slowly enough such that the spins rotate adiabatically, but fast enough such that the orbital degrees of freedom cannot follow. To satisfy the adiabaticity with respect to the spins and diabaticity with respect to the external degrees of freedom, the speed of the rotation γ_{rot} has to satisfy $\omega \ll \gamma_{\mathrm{rot}} \ll \omega_{\mathrm{L}}$, where $\omega_{\mathrm{L}} = g\mu_B B/\hbar$ is the Larmor frequency. After the rotation, the magnetic field has enclosed a D-shaped path in the xz plane. The spins are now pointing upward (in analogy to figure 3.2a but with increased angular momentum) and the transfer scheme can be applied again. Multiple repetitions are realistic and only limited by the finite lifetime of the trapped ensemble.

High angular momentum states are indeed related to the quantum Hall regime, as there is a close connection between the Landau levels and the states $|n, m\rangle$ of a two-dimensional harmonic oscillator in terms of a radial quantum number $n = 0, 1, \ldots$ and angular momentum $\hbar m$, see figure 3.2a. In particular, the ground state of N fermions filled into the harmonic oscillator with the constraint $L = L^\star$ is given by the many-body state

$$\Psi = \langle \{z_i\} | \, \mathcal{A} \prod_{m=0}^{N-1} |0, m\rangle = \mathcal{N} \left[\prod_{i<j} (z_i - z_j) \right] \mathrm{e}^{-\frac{1}{2}\sum |z_k|^2} . \tag{3.3}$$

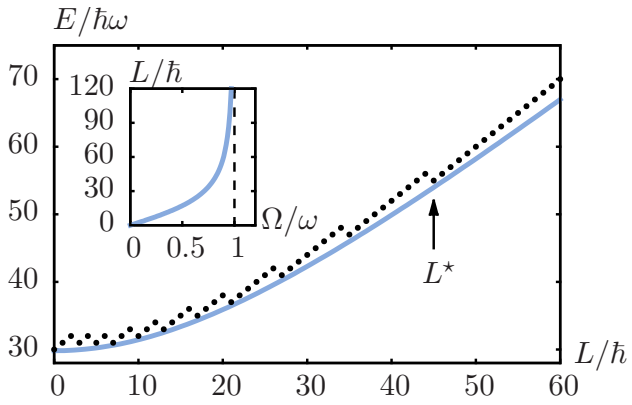

Fig. 3.3: Exact ground state energy (dots) for $N = 10$ particles at fixed angular momentum L, compared to the approximate expression (solid line) as given in equation (3.8). For $L > L^\star = 45\hbar$, the energy increases linearly. Inset shows L as a function of the rotation frequency Ω in the analytic model. L diverges at the critical rotation frequency $\Omega = \omega$, when the rotation exceeds the trap frequency.

Here $z_k = (X_k + iY_k)/l_{\mathrm{HO}}$ are complex coordinates of the particles, $\mathcal{A}$ is the antisymmetrizer, $\mathcal{N}$ is a normalization constant, and $l_{\mathrm{HO}} = \sqrt{\hbar/m\omega}$ is the harmonic oscillator length. This wave function is equivalent to the Laughlin wave function for integer filling $\nu = 1$, with $l_{\mathrm{HO}} = \sqrt{\hbar/m\omega}$ replacing the magnetic length $\sqrt{2}l_m = \sqrt{2\hbar c/eB}$ for electronic systems. Quite generally, the states with $n = 0$ and $m \geq 0$ correspond to the states in the lowest Landau level, see figure 3.2c. To reach the LLL regime, we have to repeat the transfer scheme at least $L^\star/N\hbar = (N-1)/2$ times.

3.2.1 Modeling the transfer

To quantify a single transfer process, our first aim is to calculate the total energy of N harmonically trapped fermions for a fixed total angular momentum L (polarized state, one spin component). For the noninteracting system, the energy can be obtained by simple summations. We start with the ground state for $L = 0$, where all energy shells up to the Fermi energy are completely filled. The energy of the single particle states $|n, m\rangle$ is given by $E_{nm} = \hbar\omega(2n+|m|+1)$. To avoid cluttering of notation, we introduce dimensionless quantities indicated by a $\hat{}$ sign. These quantities are measured in oscillatory units. That is, energy in units of $\hbar\omega$, angular momentum in units of $\hbar$, lengths in units of l_{HO} and time in units of ω^{-1}. The degeneracy of each energy level is simply given by $g(\hat{E}) = \hat{E}$. With $N = \sum g(\hat{E}) = \hat{E}_{\mathrm{F}}(\hat{E}_{\mathrm{F}} + 1)/2$ the Fermi energy is determined

by

$$\hat{E}_{\mathrm{F}} = \frac{1}{2}\left(\sqrt{8N+1}-1\right) \xrightarrow{N\gg 1} \sqrt{2N}. \tag{3.4}$$

The total energy for N particles is then given by

$$\hat{E}(N) = \sum_{\hat{E}=1}^{\hat{E}_{\mathrm{F}}} g(\hat{E})\hat{E} = \frac{N}{3}\sqrt{8N+1} \xrightarrow{N\gg 1} \frac{(2N)^{3/2}}{3} \tag{3.5}$$

which shows the known scaling of a trapped 2D Fermi gas [141]. Note that the energy for the unpolarized system is given by $2\,\hat{E}(N/2) = \frac{2}{3}N^{3/2}$. To derive the total energy $E(N,L)$ for $L \neq 0$, we define N_m as the number of particles with angular momentum m. The energy in terms of N_m is given by

$$\hat{E} = \sum_m \sum_{n=0}^{N_m-1} \hat{E}_{nm} = \sum_m N_m\left(N_m + |m|\right). \tag{3.6}$$

The exact ground state energy can be found combinatorially for small particle numbers by varying the N_m for fixed N and L. The result for $N = 10$ is shown in figure 3.3. For larger particle numbers this method is not feasible, but an analytic solution can be found for large particle numbers. Then, we can treat N_m as a continuous function. To find the minimum of equation (3.6) at fixed N and L, we introduce two Lagrange multipliers μ, Ω for the conditions $N = \sum_m N_m$ and $\hat{L} = \sum_m N_m m$, respectively. Taking the functional derivative with respect to N_m yields $N_m = (\hat{\mu} - |m| + \hat{\Omega}m)/2$. The parameters can be determined by solving the constraints and summing from $m_- = -\hat{\mu}/(1+\hat{\Omega})$ to $m_+ = \hat{\mu}/(1-\hat{\Omega})$, where $N_{m_\pm} = 0$. One finds

$$\hat{\Omega} = \frac{3\hat{L}}{\sqrt{\left(2N\right)^3 + \left(3\hat{L}\right)^2}}, \qquad \hat{\mu} = \frac{N^2}{\sqrt{\left(2N\right)^3 + \left(3\hat{L}\right)^2}}. \tag{3.7}$$

By using these relations and omitting correction terms of order $1/L$ and $\sqrt{N}$, we obtain the total energy

$$\hat{E}(N,\hat{L}) = \frac{1}{3}\sqrt{\left(2N\right)^3 + \left(3\hat{L}\right)^2}. \tag{3.8}$$

This result agrees with the exact behavior for $L = 0$ as derived in equation (3.5), and even for particle numbers as small as $N = 10$ it is close to the exact ground state energy, as shown in figure 3.3. For $L \geq L^\star$, the minimization

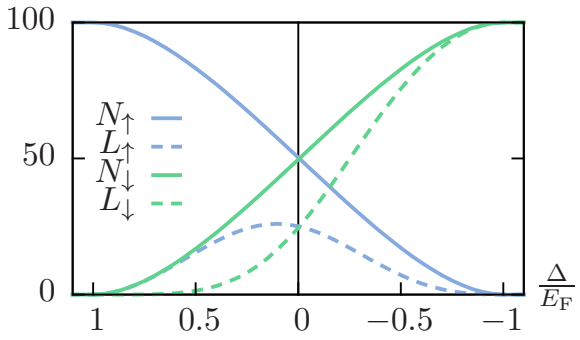

Fig. 3.4: Description of the transfer in the analytical model with $N = 100$ particles for decreasing energy splitting Δ between the two components $\uparrow$ and $\downarrow$. The transfer starts at $\Delta = E_F$ with particles continuously being transferred into the $\downarrow$ state as Δ is lowered to $-E_F$. Notice that during the transfer, both components rotate in the same direction. The crossing $N_\uparrow = N_\downarrow$ is not precisely at $\Delta = 0$ due to the initial bias.

problem becomes trivial as all particles occupy the lowest Landau level. The energy is exactly given by $\hat{E} = \hat{L}$, which is also obtained asymptotically from equation (3.8) in the limit $\hat{L} \gg N$.

It is now possible to quantify the link between our approach (fixed angular momentum) and rapidly rotating systems (fixed rotation frequency) explicitly. Both are connected by a Legendre transform and we should in fact interpret the Lagrange multiplier $\Omega = \frac{\partial E}{\partial L}$ as the rotation frequency. In a harmonic trap, the system becomes unstable if Ω exceeds the value of the trap frequency ω, as the harmonic confinement in the rotating frame is effectively given by $\omega - \Omega$. The angular momentum

$$\hat{L} = \frac{(2N)^{3/2}}{3} \frac{\hat{\Omega}}{\sqrt{1 - \hat{\Omega}^2}} \tag{3.9}$$

has a singularity for $\hat{\Omega} = \Omega/\omega = 1$ and large values of L can only be achieved by tuning Ω close to the critical value. It is this precise control on the rotation frequency that so far prevented the experimental realization of the quantum Hall regime in harmonically trapped gases. In contrast, for the present situation, the system is always stable as $\Omega(L) < \omega$ for all L. An arbitrary orbital angular momentum can be transferred to the system by the ramping scheme with high precision.

Starting from expression (3.8) for the energy, we are now able to describe the transfer process in the adiabatic limit. Let $N_\uparrow$ be the number of particles in

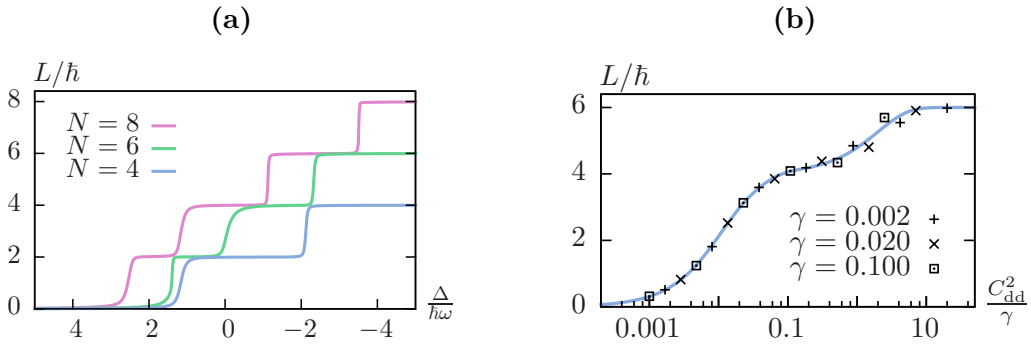

Fig. 3.5: (a) Full simulation of the transfer scheme for $N = 4, 6$, and 8 particles in the adiabatic limit $\gamma \to 0$. As the Zeeman splitting Δ is tuned through zero, the angular momentum increases in steps of $2\hbar$, indicating the transfer of two particle at a time. The interaction strength is given by $\hat{C}_{\mathrm{dd}} = 0.1$. **(b)** Angular momentum at the end of the transfer for $N = 6$ particles at different values of the Landau-Zener parameter $\lambda = \hat{C}_{\mathrm{dd}}^2/\hat{\gamma}$. The data points for different rates collapse onto a single curve. The solid line is a probabilistic model, fitted to the data points.

the spin-up state and $N_\downarrow = N - N_\uparrow$ the particles in the spin-down state. We describe both components separately and write the total energy as

$$E(N_\uparrow, L_\uparrow) + E(N_\downarrow, L_\downarrow) + \Delta \cdot N_\downarrow \tag{3.10}$$

where we have introduced the Zeeman energy shift $\Delta = \mu_{\mathrm{B}} g B$ (energy measured with respect to the energy of the lower Zeeman state). We assume that every particle eventually takes part in the transfer process (adiabaticity) and consequently one quanta of angular momentum is transferred per particle. Starting from the nonrotating state at $L = 0$, this imposes the transfer condition $L_\uparrow + L_\downarrow = L = N_\downarrow \hbar$. Adding this condition with another Lagrange multiplier, one can quantify the transfer process as a function of Δ, see figure 3.4. Coming from high fields where $\Delta > E_{\mathrm{F}}$, the transfer starts right at the Fermi energy. Note that during the transfer, while $E_{\mathrm{F}} > \Delta > -E_{\mathrm{F}}$, both components $(\uparrow, \downarrow)$ rotate in the same direction. Eventually all particles get transferred to the lower spin state and the total angular momentum equals $L = L_\downarrow = N\hbar$.

3.3 Numerical simulation

To justify the adiabaticity assumption above, we simulate the transfer process for small systems of few particles. We include all interactions mediated by $V_{\mathrm{dd}}(R, \phi)$,

and assume, that the strength of the interaction $\hat{C}_{\mathrm{dd}} = (C_{\mathrm{dd}}/l_{\mathrm{HO}}^3)/\hbar\omega \ll 1$ is weak compared to the Landau level splitting. Then, only a few excited states have to be taken into account. The system dynamics is described by

$$H = \sum_i \left[E_{nm} + \Delta(t)\,\delta_{\sigma,\downarrow}\right] c_i^\dagger c_i + \frac{1}{2}\sum_{ijkl} V_{ijkl}\, c_i^\dagger c_j^\dagger c_l c_k \tag{3.11}$$

where each of the indices $ijkl$ of the fermionic operators labels a set of quantum numbers (n, m, σ) and $\Delta(t)/\hbar\omega = -\gamma t$ is the time-dependent Zeeman shift, controlled by the linearly decreasing magnetic field. The calculation of the dipolar interaction matrix elements $V_{ijkl} \sim C_{\mathrm{dd}}$ is presented in appendix D. The only relevant parameters in this model are the transfer rate $\hat{\gamma} = \gamma/\omega$ and the interaction strength $\hat{C}_{\mathrm{dd}}$. For the perfect adiabatic transfer, in the limit $\gamma \to 0$, we can find the instantaneous ground state of H as Δ decreases. The results are shown in figure 3.5a for $N = 4, 6$, and 8 particles. The total angular momentum $L(\Delta)$ increases gradually from $L = 0$ to $L = N\hbar$ in steps of $2\hbar$, indicating that two particles are transferred at a time.

To obtain results for a finite transfer rate γ, we simulate the full time-dependent many-body problem. The total angular momentum $L(t \to \infty)$ at the end of the transfer for $N = 6$ particles is shown in figure 3.5b for different values of $\hat{C}_{\mathrm{dd}}$ and $\hat{\gamma}$. Remarkably, the data points collapse onto a single line using $\lambda = \hat{C}_{\mathrm{dd}}^2/\hat{\gamma}$. This parameter arises in the Landau-Zener formula of a single level crossing, and the collapse indicates that each pair transfer is dominated by an individual avoided level crossing.

3.3.1 Probabilistic Landau-Zender model

We can derive a very simple model that accounts for this behavior and describes the final angular momentum observed in the full simulation (see solid line). To derive the total amount of angular momentum after the transfer we assume that each 2-particle process is described by an independent Landau-Zener (avoided) crossing, neglecting any interference effects. For each Landau-Zener process, we define the probability to transfer the n-th pair of particles by $P_n = 1 - \mathrm{e}^{-\lambda/\lambda_n}$ with $\lambda = \hat{C}_{\mathrm{dd}}^2/\hat{\gamma}$ the Landau-Zener parameter and λ_n an effective coupling strength, describing the n-th pair-transfer process. The total angular momentum for N particles after one cycle is then given by weighting each possible outcome

$(\hat{L} = 0, \hat{L} = 2, \ldots, \hat{L} = N)$ by the respective probability

$$\begin{aligned}\hat{L}_N &= \sum_{n=1}^{N/2-1} 2n\, P_1 \cdots P_n(1 - P_{n+1}) + N P_1 \cdots P_{N/2} \\ &= 2P_1\left(1 + P_2\left(1 + P_3\left(1 + \ldots\left(1 + P_{N/2}\right)\right)\right)\right). \end{aligned} \tag{3.12}$$

For $N = 6$ particles this reduces to

$$\begin{aligned}\hat{L}_6 &= 2P_1(1 + P_2(1 + P_3)) \\ &= 2\left(1 - e^{-\lambda/\lambda_1}\right)\left(1 + \left(1 - e^{-\lambda/\lambda_2}\right)\left(2 - e^{-\lambda/\lambda_3}\right)\right). \end{aligned} \tag{3.13}$$

The assumption of independent crossings can now be justified a-posteriori. By fitting $\hat{L}_6$ to the simulation data we find $\lambda_1 = 0.0056$, $\lambda_2 = 0.025$, $\lambda_3 = 1.74$ with $\lambda_1 \ll \lambda_2 \ll \lambda_3$. While we suspect this approximation to break down for larger N, the model describes the transfer for small particle numbers in good agreement with the simulation.

3.4 Experimental realization and detection

The preparation of the integer quantum Hall state with an orbital angular momentum of $\hat{L}^\star = N(N-1)/2$ is finally achieved by a sequence of ramping cycles: Starting with an unpolarized sample with the fermions equally distributed between the two spin states, i.e., $N_\uparrow = N_\downarrow = N/2$, a first transfer increases the orbital angular momentum by only $\hat{L} = N/2$. Then, $N/2 - 1$ subsequent cycles will transfer exactly the required orbital angular momentum to reach the integer quantum Hall state.

In an experimental realization with ^{161}Dy atoms, the number of cycles can be significantly reduced due to the total spin of $F = 21/2$ in the hyperfine ground state. Although calculations for 22 internal levels are too complex, we expect no qualitative modifications, except that $21\hbar$ of angular momentum are transferred per particle and cycle. Other highly dipolar fermions used in cold atom experiments are ^{167}Er and ^{53}Cr with a total angular momentum of $F = 19/2$ and $9/2$, respectively [142, 143]. They could therefore provide $19\hbar$ or $9\hbar$ of angular momentum per atom and transfer. One thing to keep in mind for Lanthanides is the immense number of Feshbach resonances, which could pose a problem for our transfer scheme [144, 145].

The two important experimental requirements are a precise magnetic field control [146] as well as a deterministic preparation scheme for a certain particle

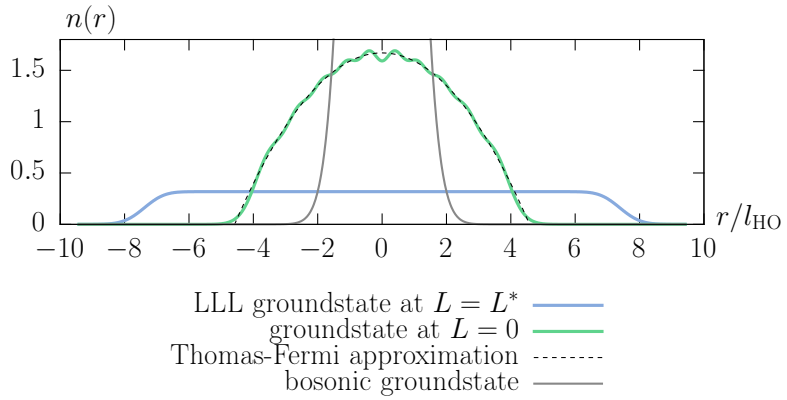

Fig. 3.6: Density distribution $n(r)$ for different non-interacting states of $N = 55$ particles. The fermionic LLL state at $L = L^\star$ has a perfectly flat density of $1/\pi l_{\mathrm{HO}}^2$ in a circular region of radial size $\sqrt{N} l_{\mathrm{HO}} \approx 7.4 l_{\mathrm{HO}}$ while the $L = 0$ ground-state is close to the well-known parabolic Thomas-Fermi distribution. The bosonic ground state is shown for comparison.

number, as demonstrated in [147]. For the magnetic field ramp we can estimate an optimal minimum value for the rate $\hat{\gamma} = 2\hat{E}_{\mathrm{F}}/\hat{t}_{\mathrm{e}} = 2\sqrt{2N}/\omega t_{\mathrm{e}}$ by observing that the Zeeman splitting has to be tuned at least once from E_{F} to $-E_{\mathrm{F}}$ within the experimental accessible time t_{e}, which is limited by the lifetime of the atoms in the trap. The Landau-Zener parameter is finally given by

$$\lambda = \frac{\omega t_{\mathrm{e}}}{2\sqrt{2N}} \left(\frac{l_{\mathrm{DDI}}}{4 l_{\mathrm{HO}}} \right)^2 \tag{3.14}$$

where the length $l_{\mathrm{DDI}} = m\kappa d^2/\hbar^2$ parametrizes the strength of the interaction [88]. In a setup with $N \sim 10$ fermionic ^{161}Dy atoms, a long lifetime of $t_{\mathrm{e}} = 10\mathrm{s}$ and a radial frequency of $\omega = 3\mathrm{kHz}$ are needed to reach values of λ on the order of 1. We comment, however, that the transfer scheme works already for smaller values of λ.

A particularly interesting property of the integer quantum Hall state, potentially useful to detect the successful generation, is the perfectly flat density $n = 1/\pi l_{\mathrm{HO}}^2$ within a circular region of radial size $\sqrt{N} l_{\mathrm{HO}}$, shown in figure 3.6.

3.5 Fractional Quantum Hall states

By simply continuing the transfer scheme, it is possible to reach states with $L > L^\star$. In this regime, highly correlated ground states appear that are closely

Species	cycles	particles	obtained state (ν)
^{161}Dy ($F = 21/2$)	1	64	1
	1	$22^\star$	$1/3$
	1	10	$1/7$
	1	8	$1/9$
	2	$22^\star$	$1/5$
	3	$22^\star$	$1/7$
^{167}Er ($F = 19/2$)	1	58	1
	1	$20^\star$	$1/3$
	2	$20^\star$	$1/5$
^{53}Cr ($F = 9/2$)	1	28	1
	1	$10^\star$	$1/3$
	2	$10^\star$	$1/5$

Table 3.1: Playing with numbers: Examples of accessible final fractional states with more than 4 particles for a perfectly working transfer scheme. For $N^\star = 2F+1$ particles, every FQHE state can be obtained with $m = 1/\nu$ cycles.

connected to fractional quantum Hall effect (FQHE) states. We consider a situation where we start from an unpolarized state and run the initial half-cycle to the polarized state (transferring $F \cdot N$ angular momentum). The subsequent k cycles transfer $2F \cdot N$ of angular momentum. A FQHE state with a filling of $\nu = 1/m$ has a total angular momentum of $m \cdot L^\star$. Consequently, $k = \frac{1}{2}\left(\frac{m(N-1)}{2F} - 1\right)$ cycles are needed to generate a $\nu = 1/m$ state with N particles. Table 3.1 shows a few possible scenarios for the generation of fractional states for small numbers of particles and a perfectly working transfer scheme.

The obtained (non-interacting) states in the lowest Landau level at $L > L^\star$ are highly degenerate, as there are many possibilities to distribute the total angular momentum among the particles. In fact, it is easy to show that the degeneracy $g(N, \Delta L)$ of the state with N particles and an excess angular momentum of $\Delta L = L - L^\star$ is given by the number of integer partitions of the number ΔL into at most N integers. Each term in such an integer partition is related to the angular momentum offset of a particle from its initial position at $\Delta L = 0$. As an example, consider the case of $N = 3$ particles and a total angular momentum of $L = L^\star + \Delta L = 3 + 4$. Then, we have an excess angular momentum of $\Delta L = 4$

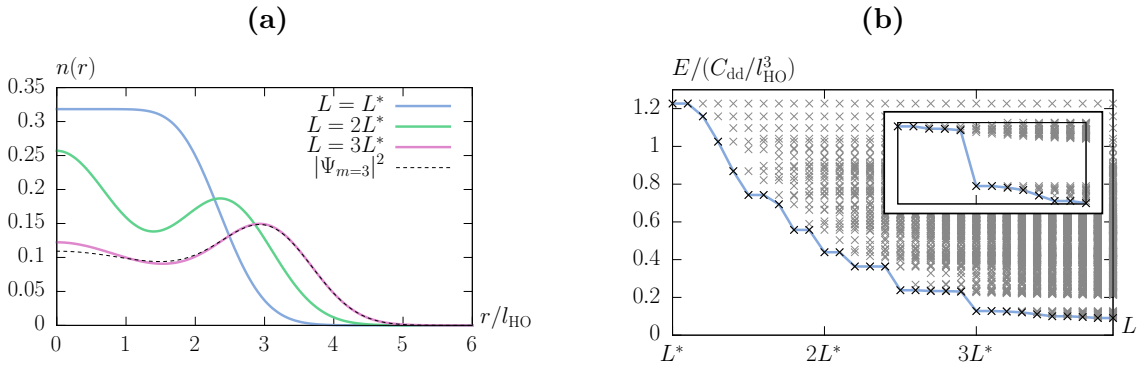

Fig. 3.7: **(a)** Density distributions for interacting ground states of $N = 6$ particles at total angular momentum $L = L^\star, 2L^\star$ and $3L^\star$. The Laughlin wave function at $m = 3$ ($\nu = 1/3$) is shown for comparison. **(b)** Ground state energy and excitation spectrum of $N = 5$ particles for increasing angular momentum. The inset shows the opening gap at $L = 3L^\star$, corresponding to a filling of $\nu = 1/3$.

and the degeneracy of the state is given by $g(3, 4) = 4$ with the following four possible integer partitions and their related states $|m_1, m_2, m_3\rangle$:

$$\begin{aligned} 4 &\longleftrightarrow |0, 1, 6\rangle\,, & 2 + 2 &\longleftrightarrow |0, 3, 4\rangle\,, \\ 1 + 3 &\longleftrightarrow |0, 2, 5\rangle\,, & 1 + 1 + 2 &\longleftrightarrow |1, 2, 4\rangle\,. \end{aligned} \tag{3.15}$$

For $N = 4$ particles (or more) with the same $\Delta L = 4$, there would be one additional integer partition $1 + 1 + 1 + 1$, leading to five degenerate states. In general, this degeneracy grows exponentially with the number of particles and angular momentum, as the asymptotic behavior for $\Delta L = N$ shows [148]:

$$g(N, N) \sim \frac{1}{4N\sqrt{3}}\, \mathrm{e}^{\pi\sqrt{\frac{2N}{3}}}\,. \tag{3.16}$$

3.5.1 Exact diagonalization in the lowest Landau level

The dipolar interaction lifts this huge degeneracy and highly correlated ground states appear [135–137, 149–151]. In our setup, it is possible to directly tune to certain angular momentum values instead of obtaining L from a given rotation frequency Ω. We can calculate the ground state at a fixed angular momentum L for small particle numbers by exact diagonalization in the degenerate subspace. Again, we assume that the strength of the interaction $\hat{C}_{\mathrm{dd}} = (C_{\mathrm{dd}}/l_{\mathrm{HO}}^3)/\hbar\omega \ll 1$

is weak compared to the Landau level splitting. The matrix elements of the dipolar interaction in the lowest Landau level are given in equation (D.11).

Figure 3.7a shows the density distribution of the interacting ground states for six particles. While the density for $L = L^\star$ is flat in the center, the distribution spreads to higher radii for increasing L. The density distribution at $L = 3L^\star$ is close to the corresponding Laughlin wave function at a filling of $\nu = 1/3$. Figure 3.7b shows the ground state energy and the excitation spectrum for five particles at different total angular momentum. The decreasing energy is a consequence of the spreading density at higher angular momentum. At $L = 3L^\star$ it is possible to see evidence for a gap opening. For details like overlap calculations, we refer to work by Osterloh et al. [137] and Qiu et al. [149].

4

Topological band structures from dipolar exchange interactions

A well established concept for the generation of two-dimensional topologically ordered states exhibiting anyonic excitations are flat bands characterized by a topological invariant in combination with strong interactions [152, 153]. The prime example is the fractional quantum Hall effect, where strong magnetic fields generate Landau levels [154]. Furthermore, lattice models without Landau levels have been proposed for the realization of topological bands [32, 155–172]. Notably, spin-orbit coupling has emerged as an experimentally promising tool for band structures with topological invariants [49–51, 173–175]. In this chapter, we show that dipolar interactions, exhibiting intrinsic spin-orbit coupling, can be exploited for the realization of topological bands with cold polar molecules.

In cold gases experiments, the phenomenon that dipolar interactions exhibit spin-orbit coupling is at the heart of demagnetization cooling [91, 92, 146, 176], and has been identified as the driving mechanism for the Einstein-de Haas effect in Bose-Einstein condensates [P4, 140] and the pattern formation in spinor condensates [139, 177, 178]. Recently, it has been pointed out that dipolar spin-orbit coupling can be observed in band structures realized with polar molecules [75]. These ideas are motivated by the experimental success in cooling and trapping polar molecules in optical lattices [70, 96–100].

Here, we show that a system of polar molecules gives rise to topological band structures, exploiting the spin-orbit coupling of dipolar interactions in combi-

nation with a term that breaks time-reversal symmetry. The main advantages of our realization are its robustness and the low experimental requirements, while many alternative theoretical proposals with cold gases require strong spatially inhomogeneous laser fields with variations on the scale of one lattice constant [166, 172, 179–184]. We point out that our proposal can also be applied to Rydberg atoms in similar setups [80, 185, 186].

4.1 Introduction to topological band structures

As an introduction to topological band structures, we shortly review the theory for a two-band model. For a detailed overview of this topic, see reviews by Hasan and Kane [51] and Bernevig [187]. Consider the following generic tunneling Hamiltonian

$$H = \sum_{i \neq j} \psi_i^\dagger T_{ij} \psi_j, \tag{4.1}$$

where $\psi_i^\dagger = (b_{i,+}^\dagger, b_{i,-}^\dagger)$ is a spinor-operator acting on lattice site i at position $\mathbf{R}_i$, involving two creation operators which are related to an internal degree of freedom or to the specific position for a lattice with a two-site unit cell. The tunneling elements are described by the two-by-two matrix T_{ij}. As will become clear later, we can assume that T_{ij} is traceless, since we are only interested in the topological properties. Using the translational symmetry, the model can be block-diagonalized in momentum space by introducing the Fourier representation $\psi_{\mathbf{k}} = \frac{1}{\sqrt{N_s}} \sum_j \psi_j \, \mathrm{e}^{i\mathbf{k}\mathbf{R}_j}$, with N_s the number of lattice sites:

$$H = \sum_{\mathbf{k}} \psi_{\mathbf{k}}^\dagger H_{\mathbf{k}} \psi_{\mathbf{k}}, \qquad H_{\mathbf{k}} = \sum_{i \neq 0} T_{i0} \, \mathrm{e}^{-i\mathbf{k}\mathbf{R}_i} \, . \tag{4.2}$$

Since the Bloch-Hamiltonian is a traceless Hermitian two-by-two matrix, it can always be written as the product $H_{\mathbf{k}} = \mathbf{n}_{\mathbf{k}} \cdot \boldsymbol{\sigma}$ of a three-dimensional real vector $\mathbf{n}_{\mathbf{k}}$ and the vector of Pauli matrices $\boldsymbol{\sigma}$. Note that the vector $\mathbf{n}_{\mathbf{k}} \in \mathbb{R}^3$ includes the full information about this system. In particular, the two band dispersion relation is simply given by $E_{\mathbf{k},\pm} = \pm|\mathbf{n}_{\mathbf{k}}|$.

A seemingly trivial observation in topological band theory is the realization that $\mathbf{n}_{\mathbf{k}}$ contains more information than just the dispersion relation. To see this, we assume that (for a certain set of parameters) the model has no band-crossing, such that the vector $\mathbf{n}_{\mathbf{k}}$ is nonzero for all $\mathbf{k}$ in the Brillouin zone. Then, we can “factor out” the information about the dispersion relation and consider the

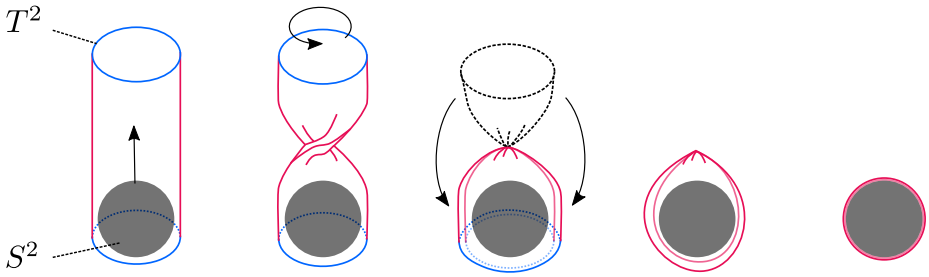

Fig. 4.1: Visualization of (an equivalence class of) mappings $T^2 \to S^2$ from a torus to a sphere with a nontrivial winding number $C = 2$. We start by placing the sphere inside the torus, which has been cut along the blue circle. Twisting the upper half of the torus by 2π and folding down, we can seal the torus along the blue circle and contract the glued joint to a single point. Now, each point on the torus T^2 lies on (points to) a specific position on the surface of the sphere. The torus covers the sphere twice, hence the winding number of two.

normalized vector $\hat{\mathbf{n}}_\mathbf{k} = \mathbf{n}_\mathbf{k}/|\mathbf{n}_\mathbf{k}|$. Mathematically, this is a mapping $\hat{\mathbf{n}}\colon T^2 \to S^2$ from a two-torus T^2 (the structure of the two-dimensional Brillouin zone) to the two-sphere S^2 (because the three-dimensional vector is normalized). Continuous functions of this kind can be classified with topological methods. It is possible to visualize a mapping $T^2 \to S^2$ (see figure 4.1 for an example), but it is easier to continue this discussion with a conceptually simpler mapping $S^2 \to S^2$ from a sphere to itself. It can be shown that the classification is in fact equivalent [188]. In algebraic topology, continuous functions with the general structure $S^k \to S^n$ are classified by the k-th homotopy group of the n-sphere, denoted by $\pi_k(S^n)$. Functions $f\colon S^1 \to S^1$ from the unit-circle to itself, for example, are classified by the first homotopy group (called the fundamental group) of S^1. It is well known that $\pi_1(S^1) \cong \mathbb{Z}$, because mappings of this kind can be classified by a winding number

$$\nu = \frac{1}{2\pi}\int_0^{2\pi} \mathrm{d}k\, \partial_k f(k) = \frac{f(2\pi) - f(0)}{2\pi} \in \mathbb{Z} \tag{4.3}$$

that counts how many times the origin is encircled as we integrate over $k \in S^1$. For our two-dimensional model, we are interested in the second-homotopy group of the two-sphere. It turns out that $\pi_2(S^2) \cong \mathbb{Z}$. Consequently, different mappings $\hat{\mathbf{n}}_\mathbf{k}$ (that is, different band structures) can be classified by a topological index $C \in \mathbb{Z}$ called the Chern number. In a similar way to the one-dimensional example, the Chern number can be calculated as a winding number of the

vector $\hat{\mathbf{n}}_\mathbf{k}$ via:

$$C = \frac{1}{4\pi} \int_{\mathrm{BZ}} \mathrm{d}^2\mathbf{k}\, (\partial_{k_x} \hat{\mathbf{n}}_\mathbf{k} \times \partial_{k_y} \hat{\mathbf{n}}_\mathbf{k}) \cdot \hat{\mathbf{n}}_\mathbf{k}\,. \tag{4.4}$$

Similar to a winding number of a closed path $\gamma\colon S^1 \to \mathbb{R}^2 \setminus \{\mathbf{0}\}$ in the punctured plane, the Chern number cannot change unless the vector $\mathbf{n}_\mathbf{k}$ is zero for a certain point $\mathbf{k}$ in the Brillouin zone. This shows that the space of all possible Hamiltonians $H_\mathbf{k}$ factors into discrete classes of adiabatically equivalent models, characterized by their Chern number: band structures that can be deformed into one another without closing the bandgap.

It is this kind of robustness that makes topological properties interesting for applications. The physical properties that follow from a nontrivial Chern number are robust against small perturbations in the above-mentioned sense. The most important link to physical properties is the bulk-edge correspondence [33]. It guarantees the existence of edge states at the boundaries between different topological phases. In particular, for a finite two-band system, the number of states at the edge of the system is equal to the Chern number (imagine the vacuum outside as being topologically trivial). A related consequence of the nonzero Chern number appears in a fermionic system with a completely filled lowest band (Chern insulator). Here, the Hall conductance is directly related to the Chern number via $\sigma_{xy} = \frac{e^2}{h} C$.

Another way to look at the topological properties of the band structure and the meaning of the Chern number is through the theory of Berry phases [18, 19]. Given the Bloch eigenstates $|u_\mathbf{k}\rangle$ of the lower band, i.e. $H_\mathbf{k}\,|u_\mathbf{k}\rangle = E_{\mathbf{k},-}\,|u_\mathbf{k}\rangle$, we can define the Berry vector potential by $\mathbf{A}(\mathbf{k}) = i\,\langle u_\mathbf{k}|\nabla_\mathbf{k}|u_\mathbf{k}\rangle$. Using this, we can calculate the Berry phase along a closed path $\partial\mathcal{S}$ in the Brillouin zone via

$$\gamma(\mathcal{S}) \equiv \int_{\partial\mathcal{S}} \mathrm{d}\mathbf{k} \cdot \mathbf{A}(\mathbf{k}) = \int_\mathcal{S} \mathrm{d}^2k\, B(\mathbf{k}) \tag{4.5}$$

where $B(\mathbf{k}) = (\nabla_\mathbf{k} \times \mathbf{A}(\mathbf{k}))_z = \partial_{k_x} A^y(\mathbf{k}) - \partial_{k_y} A^x(\mathbf{k})$ is the Berry curvature. For the two-band model, the Berry curvature is given by

$$B(\mathbf{k}) = \frac{1}{2} (\partial_{k_x} \hat{\mathbf{n}}_\mathbf{k} \times \partial_{k_y} \hat{\mathbf{n}}_\mathbf{k}) \cdot \hat{\mathbf{n}}_\mathbf{k}. \tag{4.6}$$

Comparing this with equation (4.4), we see that the Chern number can be seen as the total Berry curvature $\gamma(T^2)$ in the Brillouin zone divided by 2π. Now let $\mathcal{S}$ be a region $\mathcal{S} \subset T^2$ and $\mathcal{S}^c = T^2 \setminus \mathcal{S}$ be its complement. Then, the sum of

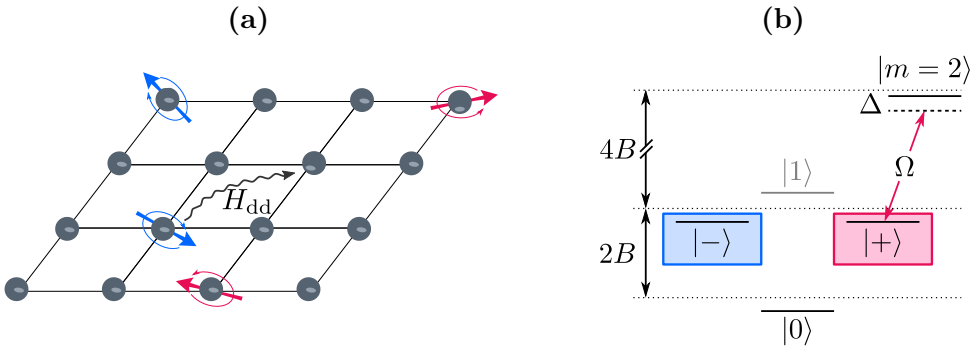

Fig. 4.2: **(a)** Setup: Each lattice site of a two-dimensional optical lattice is occupied by a single polar molecule. The molecules can be excited into two different rotational states. Dipole-dipole interactions induce long-range tunneling links for the excitations. **(b)** Rotational level structure of each molecule with applied electric field and additional microwave field with Rabi frequency Ω and detuning Δ.

the Berry phases $\gamma(\mathcal{S})$ along $\partial\mathcal{S}$ and $\gamma(\mathcal{S}^c)$ along the reversed path $\partial\mathcal{S}^c$ has to be an integer multiple of 2π. On the other hand $\gamma(\mathcal{S}) + \gamma(\mathcal{S}^c) = \gamma(T^2) = 2\pi C$. This shows that the Chern number has to be an integer.

An important aspect for topological phases is the role of symmetries [189–191]. For the purposes of this chapter, we are mainly interested in time-reversal symmetry. A Hamiltonian H is time-reversal symmetric, if there exists an anti-unitary operator $\mathcal{T}$ such that $\mathcal{T}^{-1}H\mathcal{T} = H$. For the Bloch Hamiltonian, this translates to the condition $U^\dagger H^*_{\mathbf{k}} U = H_{-\mathbf{k}}$, where U is a unitary operator. Such a condition forces the vector $n_{\mathbf{k}}$ to lie in a plane. For $U = \sigma_x$, for example, we have $n^z_{\mathbf{k}} = 0$ whereas for $U = \mathbb{1}$ we have $n^y_{\mathbf{k}} = 0$. Consequently, the mapping $\mathbf{n}_{\mathbf{k}}$ cannot cover the whole sphere and the Chern number is zero. A more physical way to see this, is that the Berry curvature (and hence the Chern number) is odd under time-reversal. Therefore, breaking of time-reversal symmetry is a necessary requirement for a nonzero Chern number.

4.2 Setup

We consider a two-dimensional system of ultracold polar molecules in a deep optical lattice with one molecule pinned at each lattice site, as shown in figure 4.2a. The remaining degree of freedom is given by the internal rotational

excitations of the molecules with the Hamiltonian

$$H_i^{\mathrm{rot}} = B\mathbf{J}_i^2 - \mathbf{d}_i \cdot \mathbf{E}\,. \tag{4.7}$$

Here, B is the rotational splitting, $\mathbf{J}_i$ is the angular momentum of the ith molecule and $\mathbf{d}_i$ is its dipole moment which is coupled to the applied static and microwave electric fields $\mathbf{E} = \mathbf{E}_{\mathrm{s}} + \mathbf{E}_{\mathrm{ac}}(t)$. In the absence of external fields, the eigenstates $|J, m\rangle$ of H_i^{rot} are conveniently labeled by the total angular momentum J and its projection m. Applying a static electric field mixes states with different J. The projection m, however, can still be used to characterize the states. In the following, we focus on the lowest state $|0\rangle$ with $m = 0$ and the two degenerate excited states $|\pm\rangle$ with $m = \pm 1$, see figure 4.2b. The first excited $m = 0$ state, called $|1\rangle$, will be used later.

The full system, including pairwise dipole-dipole interactions between the polar molecules, is described by $H = \sum_i H_i^{\mathrm{rot}} + \frac{1}{2}\sum_{i\neq j} H_{ij}^{\mathrm{dd}}$. As we have seen in equation (1.6) on page 19, the interaction for the two-dimensional setup with the electric field perpendicular to the lattice can be expressed as

$$\begin{aligned} H_{ij}^{\mathrm{dd}} = \frac{\kappa}{|\mathbf{R}_{ij}|^3}\Big[& d_i^0 d_j^0 + \frac{1}{2}\big(d_i^+ d_j^- + d_i^- d_j^+\big) \\ & - \frac{3}{2}\big(d_i^- d_j^-\, \mathrm{e}^{2i\phi_{ij}} + d_i^+ d_j^+\, \mathrm{e}^{-2i\phi_{ij}}\big)\Big] \end{aligned} \tag{4.8}$$

with $\kappa = 1/4\pi\epsilon_0$. As before, ϕ_{ij} denotes the in-plane polar angle of the vector $\mathbf{R}_{ij} \equiv |\mathbf{R}_{ij}| \cdot (\cos\phi_{ij}, \sin\phi_{ij})^t$ which connects the two molecules at lattice sites i and j, and the operators $d^0 = d^z$ and $d^\pm = \mp(d^x \pm i d^y)/\sqrt{2}$ are the spherical components of the dipole operator. The intrinsic spin-orbit coupling is visible in the second line of equation (4.8), where a change in internal angular momentum by ± 2 is associated with a change in orbital angular momentum encoded in the phase factor $e^{\mp 2i\phi_{ij}}$.

For molecules with a permanent dipole moment d in an optical lattice with spacing a, the characteristic interaction energy $V = \kappa d^2/a^3$ is much weaker than the rotational splitting B. For strong electric fields, the energy separation between the states $|\pm\rangle_i$ and $|1\rangle_i$ is also much larger than the interaction energy. Then the number of $|\pm\rangle$ excitations is conserved. As described in section 1.3.3, this allows us to map the Hamiltonian to a bosonic model: The lowest energy state $\prod_i |0\rangle_i$ with all molecules in the ground rotational state is the vacuum state, while excitations of a polar molecule into the state $|\pm\rangle_i$ are described by hard-core boson operators $b_{i,\pm}^\dagger = |\pm\rangle_i\langle 0|_i$. Note that these effective bosonic particles have a spin angular momentum of $m = \pm 1$.

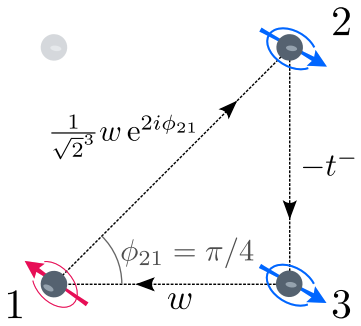

Fig. 4.3: Exemplary tunneling process along the smallest possible loop on the square lattice. The excitation hops from orbital $(\mathbf{1}, +)$ over $(\mathbf{2}, -)$ to $(\mathbf{3}, -)$ and back to $(\mathbf{1}, +)$. The spin-orbit coupling leads to a non-trivial flux $\phi_{\text{flux}} = \arg(\prod t_{ij}) = -\pi/2$, where t_{ij} are the indicated tunneling rates. Reversing all orbitals $+ \leftrightarrow -$ changes the sign to $\phi_{\text{flux}} = \pi/2$.

4.3 Bosonic model

The dipole-dipole interaction gives rise to an effective hopping Hamiltonian for the bosonic particles due to the dipolar exchange terms: $d_i^+ d_j^-$, for example, leads to a (long-range) tunneling $b_{i,+}^\dagger b_{j,+}$ for the +-bosons while the term $d_i^- d_j^-\, e^{2i\phi_{ij}}$ generates spin-flip tunneling processes $b_{i,-}^\dagger b_{j,+}\, e^{2i\phi_{ij}}$ with a phase that depends on the direction of tunneling. For the study of the single particle band structure we can drop the term proportional to $d^0 d^0$ which describes a static dipolar interaction between the bosons. Then, as shown in equation (1.30) on page 26, the interaction Hamiltonian reduces to

$$H^{\text{dd}} = \sum_{i \neq j} \frac{a^3}{R_{ij}^3}\, \psi_i^\dagger \begin{pmatrix} -t^+ & w\, e^{-2i\phi_{ij}} \\ w\, e^{2i\phi_{ij}} & -t^- \end{pmatrix} \psi_j \,, \tag{4.9}$$

where we use the spinor notation $\psi_j^\dagger = \left(b_{j,+}^\dagger, b_{j,-}^\dagger\right)$. The energy scale of the hopping rates t^+, t^-, and w is given by $V = \kappa d^2/a^3$. The exact expressions depend on the microscopic parameters and will be given in the next section. The off-diagonal terms in equation (4.9) lead to a spin-orbit coupling which can induce a non-trivial "magnetic" flux along certain paths in the lattice, see figure 4.3.

4.3.1 Time-reversal symmetry breaking by the microwave field

We have seen that a crucial aspect for the generation of topological bands with a nonzero Chern number is the breaking of time-reversal symmetry. In our setup, this is achieved by coupling the state $|+\rangle$ to the rotational state $|m = 2\rangle$ with an off-resonant microwave field with Rabi frequency $\Omega \equiv 2E_{\text{ac}}\, |\langle m = 2|d^+|+\rangle|$ and detuning Δ, see figure 4.2b. For a large detuning $\Delta \gg \Omega, V$, the number of $|+\rangle$ (and $|-\rangle$) excitations is still conserved. In the rotating frame, within the

rotating wave approximation, the AC-dressed $|+\rangle$ state is given by

$$|+\rangle_{\mathrm{ac}} = (1-\epsilon^2/2)\,|+\rangle - \epsilon\,|m=2\rangle \tag{4.10}$$

up to second order in $\epsilon = \Omega/2\Delta$. Note that the coupling of the $|-\rangle$ state to the third $m=0$ state can be neglected due to a large detuning from the difference in Stark shifts between $m=0$ and $m=2$. Therefore, the states $|0\rangle$ and $|-\rangle$ are essentially unaffected by the microwave. To avoid cluttering of notation, we also drop the *ac* label of the $|+\rangle$ state.

Then, the transition dipole moment for the $|+\rangle$ state is slightly reduced, compared to the $|-\rangle$ state. Using the definition in equation (1.24), we have $q_+ = |\langle +|d^+|0\rangle| = q_-(1-\epsilon^2/2)$. In turn, the nearest-neighbor tunneling rates from equation (1.29) are given by

$$t^+ = \frac{\kappa q_-^2}{2a^3}(1-\epsilon^2), \qquad t^- = \frac{\kappa q_-^2}{2a^3}, \qquad w = \frac{3\kappa q_-^2}{2a^3}(1-\epsilon^2/2). \tag{4.11}$$

Note that $t^+ = t^-$ without the applied microwave (time-reversal symmetric point). The microwave coupling also lifts the degeneracy between the two excitations $|\pm\rangle_i$ and provides an energy splitting given by the AC Stark shift, equal to $2\mu \equiv \Omega^2/4\Delta$. We remark that this energy shift 2μ can also be independently controlled via magnetic fields [77, 97].

4.4 Topological band structure

In momentum space with $\psi_{\mathbf{k}} = \frac{1}{\sqrt{N_s}}\sum_j \psi_j\, \mathrm{e}^{i\mathbf{k}\mathbf{R}_j}$, including the internal energy H_i^{rot} of the excitations $|\pm\rangle_i$, the Hamiltonian (4.9) can be rewritten as

$$H = \sum_{\mathbf{k}} \psi_{\mathbf{k}}^\dagger \big(n_{\mathbf{k}}^0\, \mathbb{1} + \mathbf{n}_{\mathbf{k}}\cdot\boldsymbol{\sigma}\big)\psi_{\mathbf{k}} \tag{4.12}$$

where the real vector $\mathbf{n}_{\mathbf{k}}$ characterizes the spin-orbit coupling terms and takes the form

$$\mathbf{n}_{\mathbf{k}} = \begin{pmatrix} w\,\mathrm{Re}\,\epsilon_{\mathbf{k}}^2 \\ w\,\mathrm{Im}\,\epsilon_{\mathbf{k}}^2 \\ \mu + t\,\epsilon_{\mathbf{k}}^0 \end{pmatrix}. \tag{4.13}$$

Here, we have introduced the difference in tunneling rates $t = (t^- - t^+)/2 > 0$. The spin-independent hopping is determined by $n_{\mathbf{k}}^0 = -\bar{t}\,\epsilon_{\mathbf{k}}^0$ with the average

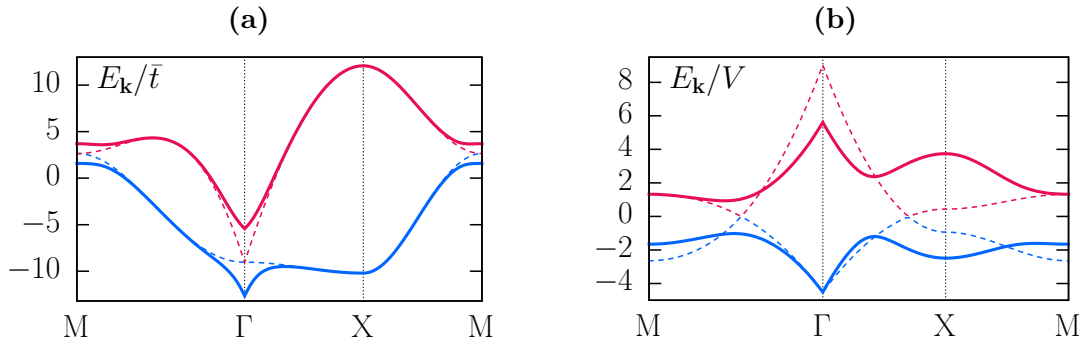

Fig. 4.4: (a) Dispersion relation for the $|+\rangle$ and $|-\rangle$ states on the square lattice. The dashed line shows the time-reversal invariant point $t = \mu = 0$ with band touching at the Γ and M point. The band minima are located at the two X points $(\pi/a, 0)$ and $(0, \pi/a)$. The solid line shows the gapped topological bands in the time-reversal-broken system for $w/\bar{t} = 3, \mu = 0$ and $t/\bar{t} = 0.4$. For $t/\bar{t} \gtrsim 0.13$, the band minimum is at the Γ point. **(b)** Dispersion relation for the $|+\rangle$ and $|1\rangle$ states for electric field angles $\Theta_0 = 0$ (dashed) and $\Theta_0 = \pi/4$ (solid), respectively. The latter has a lower band with flatness $f \approx 1$. Note: The two 'X' points $(\pi/a, 0)$ and $(0, \pi/a)$ are not equivalent in this model as the electric field breaks the x/y symmetry.

tunneling rate $\bar{t} = (t^+ + t^-)/2$. The behavior of both $n^0_\mathbf{k}$ and $\mathbf{n}_\mathbf{k}$ is determined by the previously used dipolar dispersion relation, extended to include a nonzero angular momentum transfer m [P1, P6, 75, 124]

$$\epsilon^m_\mathbf{k} = \sum_{j\neq 0} \frac{a^3}{|\mathbf{R}_j|^3} \mathrm{e}^{i\mathbf{k}\mathbf{R}_j + im\phi_j} \,. \tag{4.14}$$

The precise determination of this function can be achieved by an Ewald summation technique, providing a non-analytic low momentum behavior $\epsilon^0_\mathbf{k} \approx \epsilon^0_0 - 2\pi|\mathbf{k}|a$ and $\epsilon^2_\mathbf{k} \approx -\frac{2\pi}{3}|\mathbf{k}|a\,\mathrm{e}^{2i\varphi}$. Here, $\epsilon^0_0 \approx 9.03$ and φ is defined by $\hat{\mathbf{k}} = (\cos\varphi, \sin\varphi)^t$. For details, see appendix A.

In the presence of time-reversal symmetry, represented by $\mathcal{T} = \sigma_x\mathcal{K}$ with $\mathcal{K}$ being complex conjugation, the system reduces to the one discussed by Syzranov et al. [75]. At the $\mathcal{T}$-invariant point, i.e. $t = \mu = 0$, the two energy bands of the system exhibit a band touching at the high-symmetry points $\mathbf{\Gamma} = (0, 0)$ and $\mathbf{M} = (\pi/a, \pi/a)$ where $\epsilon^2_\mathbf{k}$ vanishes, see figure 4.4a. The touching at the Γ point is linear due to the low-momentum behavior of $\epsilon^m_\mathbf{k}$. The lower band at the Γ point is flat due to the exact cancellation of the linear terms. Note that each of the touching points splits into two Dirac points if the square lattice is stretched into a rectangular lattice.

Breaking of time-reversal symmetry by the microwave field leads to an opening of a gap between the two bands. The dispersion relation is given by

$$E_{\pm}(\mathbf{k}) = -\bar{t}\,\epsilon^0_{\mathbf{k}} \pm \sqrt{w^2\left|\epsilon^2_{\mathbf{k}}\right|^2 + \left(\mu + t\,\epsilon^0_{\mathbf{k}}\right)^2} \tag{4.15}$$

and shown in figure 4.4a. It is gapped whenever the vector $\mathbf{n_k} \neq 0$. The first two components can only vanish at the Γ or M point. Consequently, the gap closes if and only if the third component is zero at one of these two points. We find the two transition points

$$\begin{aligned} \mu/t &= -\epsilon^0_0 \approx -9.03, \\ \mu/t &= -\epsilon^0_{\mathbf{M}} = \left(1 - 1/\sqrt{2}\right)\epsilon^0_0 \approx +2.65. \end{aligned} \tag{4.16}$$

In the gapped system, the Chern number can be calculated as the winding number of the normalized vector $\hat{\mathbf{n}}_\mathbf{k} = \mathbf{n_k}/|\mathbf{n_k}|$ as specified in equation (4.4). We find that the Chern number of the lower band is $C = 2$ for $-\epsilon^0_0 < \mu/t < -\epsilon^0_{\mathbf{M}}$, and zero outside this range. The non-trivial topology solely results from dipolar spin-orbit coupling and time-reversal symmetry breaking.

Please note that it is necessary to truncate the summation in the expression for $\epsilon^m_\mathbf{k}$ in order to perform the calculation of the Chern number. It is easy to check, however, that the remaining terms are not strong enough to close a gap. Conversely, the cutoff radius needs to be larger than $\sqrt{2}a$, because the next-to-nearest neighbor terms are crucial for the nontrivial Chern number and may not be neglected (the y component of $\mathbf{n_k}$ is zero otherwise).

4.5 Flat bands

One of the challenges is to find a specific setup that optimizes the flatness of the topological bands. This can be achieved either by focusing on different lattice structures (see next section) or by an alternative choice for the two excitations. Instead of considering $|+\rangle$ and $|-\rangle$, we choose a model including the $|+\rangle$ and $|1\rangle$ states. This is possible for weak electric fields, if the $|-\rangle$ state is shifted by a microwave field, or by exploiting the coupling between the nuclear spins of the polar molecules and the rotational degree of freedom [77, 97]. As described in section 1.3.4 (excluding the $|-\rangle$ state), this leads to the single-particle Hamiltonian

$$H^{\mathrm{dd}} = \sum_{i\neq j} \frac{a^3}{R^3_{ij}}\, \psi^\dagger_i \begin{pmatrix} -t^+ f_0 & w f_1^* \\ w f_1 & -t^1 f_0 \end{pmatrix} \psi_j\,, \tag{4.17}$$

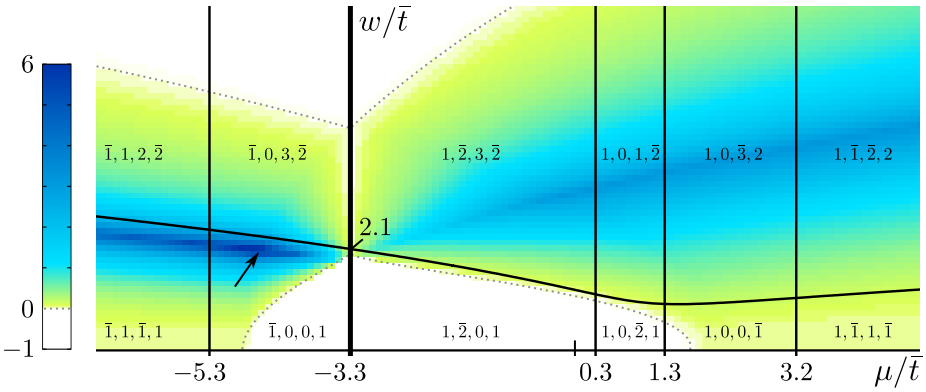

Fig. 4.5: Topological phase diagram in the honeycomb lattice for $t/\bar{t} = 0.54$. The labels give the Chern numbers of the four bands (bar indicates negative number) from bottom to top while the solid lines correspond to touching points between two bands. The color indicates the flatness f of the lowest band. The arrow shows the parameters of the flat-band model in figure 4.7b.

where $f_m = f_m(\phi_{ij} - \Phi_0, \Theta_0)$ are the functions defined in equation (1.12) on page 21, depending on the electric field direction Θ_0, Φ_0 and the tunneling rates

$$t^+ = \frac{\kappa q_+^2}{2a^3}, \quad t^1 = -\frac{\kappa q_1^2}{a^3}, \quad w = \frac{3\kappa q_+ q_-}{\sqrt{2}a^3}. \tag{4.18}$$

This model intrinsically breaks time-reversal symmetry and has the advantage that the $|+\rangle$ and $|1\rangle$ states have different signs for the tunneling strength, making the $\mathcal{T}$-breaking parameter $t = (t^+ - t^1)/2$ large compared to $\bar{t} = (t^+ + t^1)/2$. For an electric field direction perpendicular to the lattice, this system is gapless because $f_1(\phi_{ij}, 0) = 0$. Opening the gap is achieved by rotating the electric field away from the z-axis by an angle Θ. The dispersion relation for $\Theta = 0$ and $\pi/4$ is shown in figure 4.4b. The lower band has a flatness ratio of $f = \text{bandgap/bandwidth} \approx 1$.

4.6 Dependence on the lattice geometry

Returning to the simple setup in figure 4.2b, the influence of the lattice geometry on the topological properties can be exemplified by studying the case of the honeycomb lattice. Due to the two distinct sublattices, we generally obtain four bands in the presence of broken time-reversal symmetry. Depending on the microscopic parameters, the bands exhibit a rich topological structure, characterized by their Chern numbers. Note that the Chern numbers are

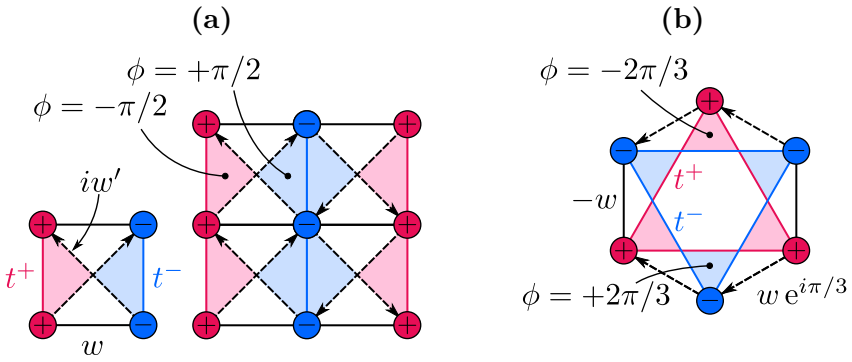

Fig. 4.6: Hopping strengths and flux pattern of a single layer in different lattices. Tunneling elements without arrow are real numbers. Complex hoppings have the indicated strength along the arrow and the complex conjugate in the opposite direction. **(a)** Square lattice: A single layer can be constructed by stripes of one component along one of the primitive vectors, effectively doubling the unit cell. The second layer is given by a translation along the second primitive vector. **(b)** Honeycomb lattice: By distributing the $|+\rangle, |-\rangle$ orbitals to the two distinct sublattices it is possible to retain the symmetry of the lattice. The second layer is given by a 60° rotation.

calculated with a numerical method similar to the one for the disordered system. In figure 4.5, we show a two-dimensional cut through the topological phase diagram, spanned by the parameters $t/\bar{t}, w/\bar{t}$ and $\mu/\bar{t}$. We find a multitude of different topological phases with large areas of flatness $f > 0$ for the lowest band. A flatness $f < 0$ indicates that the maximum of the lowest band is higher than the minimum of the second band. In contrast to the square lattice, an energy splitting $\mu \neq 0$ is sufficient for a nonzero Chern number; $t \neq 0$ is not necessarily needed. Figure 4.7b shows the dispersion relation with a lowest band of flatness $f \approx 6.4$ and a Chern number $C = -1$. The different behavior of the same model on the square and hexagonal lattice will be explained in section 4.7.1.

4.7 Classification and double-layer picture

Topological band structures can be classified by considering equivalence classes of models that can be continuously deformed into each other without closing the energy gap [51]. In particular, the Chern number of a single band can only change if it touches another band. Using this idea, we show that the square-lattice model in its $C = 2$ phase is adiabatically equivalent to a system

of two uncoupled copies of a $C = 1$ layer.

To see this, imagine separating the two orbitals $|+\rangle$ and $|-\rangle$ per site spatially along the z-direction (without changing any tunneling rates) such that we obtain two separate square lattice layers, called A and B. Sorting all terms in the Hamiltonian into intra- and inter-layer processes, we can write

$$H = H_{\mathrm{A}} + H_{\mathrm{B}} + \lambda H_{\mathrm{AB}} \tag{4.19}$$

where $\lambda = 1$. The choice of which orbital resides in layer A (and B) can be made individually for each lattice site. In any case, the resulting two layers will be interconnected by an infinite number of tunneling links H_{AB}. The idea is to find a specific arrangement of the orbitals such that we can continuously let $\lambda \longrightarrow 0$ *without* closing a gap in the excitation spectrum, preserving the topological phase while disentangling the layers.

Focusing on layer A (layer B being simply the complement), one possible arrangement is shown in figure 4.6a. The $+$ $(-)$ orbitals are assigned to odd (even) columns along the y-direction. For the Chern number of such a single layer we find $C = 1$, using methods analogous to the ones described in section 4.4. The full system can be understood as two such layers, shifted by one lattice site in x-direction. With a unit cell twice the size of the original model, each layer contributes to one half of the full Brillouin zone, effectively doubling the Chern number to $C = 2$.

The single layer system has some interesting properties. In figure 4.6a we show that it is possible to find a staggered magnetic flux pattern which creates the same tunneling phases as the dipole-dipole interaction, including tunneling up to the next-to-nearest neighbor level. The resulting single layer model is reminiscent of the famous Haldane model [32], adapted to the square lattice [156, 166, 179–183, 192, 193]. Using a site-dependent microwave dressing, it has been shown that a model similar to our single-layer system can be realized, giving rise to a $\nu = 1/2$ fractional Chern insulating phase [166, 183]. It is rather remarkable that uniform dipole-dipole interactions give rise to a model usually requiring strong modulations on the order of the lattice spacing.

4.7.1 Hexagonal lattice

The relation to the bilayer system also allows us to explain the different behavior on the hexagonal lattice. Applying the same procedure, a single layer can be constructed which retains the original symmetry of the honeycomb lattice, see

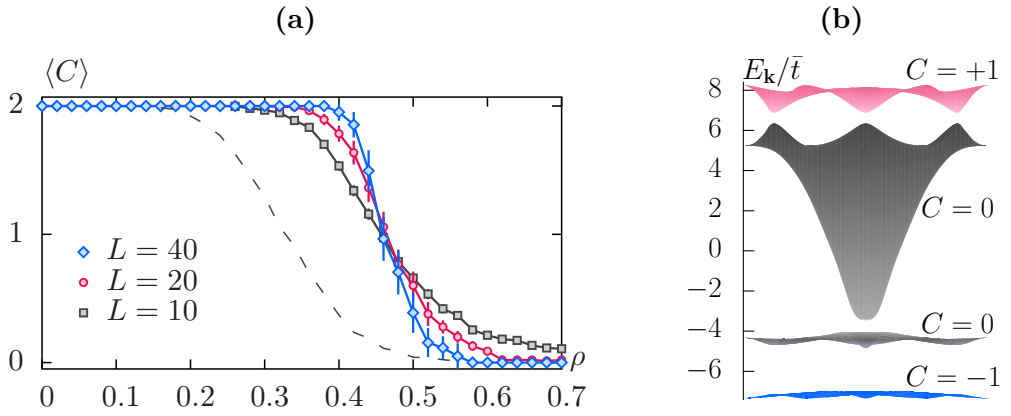

Fig. 4.7: **(a)** Sample-averaged Chern number $\langle C \rangle$ in the disordered system for increasing density ρ of defects. A single realization either yields $C = 2$ or $C = 0$. Bars indicate two standard errors. The results are shown for square lattices of size $L \times L$ with $L = 10, 20, 40$ and a cutoff radius for the interaction $R_c \lesssim L/2$ slightly smaller than half the system size to avoid self-interaction. The long-range tunneling stabilizes the topological phase for defect densities $\rho \lesssim 0.45$. As a comparison, the dashed line shows the results for a 10×10 grid with tunneling only included up to the next-to-nearest neighbor, leading to a significant destabilization. **(b)** Two-dimensional projection of the dispersion relation in the honeycomb lattice for $t/\bar{t} = 0.54$, $w/\bar{t} = 1.97$ and $\mu/\bar{t} = -4.54$. The lowest band has a flatness ratio of $f \approx 6.4$ and a Chern number of $C = -1$.

figure 4.6b. Here, the two bands of the single layer also have a Chern number of $C = \pm 1$. In contrast to the square lattice, however, the Brillouin zone of a single layer is the same as for the full (double layer) system with both orbitals at each site. Consequently, the four bands of the full system are constructed from the combination of two $C = 1$ and two $C = -1$ bands. As a result, the lowest band in the honeycomb lattice can have a Chern number of $C = 1$. Note that the inter-layer coupling in the bilayer honeycomb system is crucial to open a gap.

4.8 Influence of disorder

An experimental initialization with a perfectly uniform filling of one molecule per site is challenging. Consequently, we analyze the stability of the topological band structure for random samples with a nonzero probability ρ for an empty lattice site. The determination of the Chern number for the disordered system follows ideas from refs. [12, 14]. We start with a finite geometry of $L \times L$ lattice

sites and twisted boundary conditions

$$\begin{aligned}\psi(x+L,y) &= \mathrm{e}^{i\theta_x}\,\psi(x,y),\\ \psi(x,y+L) &= \mathrm{e}^{i\theta_y}\,\psi(x,y)\end{aligned} \tag{4.20}$$

for the single particle wave function. Next, we randomly remove ρL^2 lattice sites (dipoles). We are interested in the Chern number of the lower 'band', composed of the lowest $N_l = L^2(1-\rho)$ states (there are $2N_l$ states in total). To this end, we pretend to have a free fermionic system at half filling whose many-body ground state $\Psi = \Psi(\theta_x, \theta_y)$ is given by the Slater determinant of the lowest N_l states. Then, the Chern number can be calculated as

$$C = \frac{1}{2\pi}\iint \mathrm{d}\theta_x \mathrm{d}\theta_y\, F(\theta_x,\theta_y), \tag{4.21}$$

where $F(\theta_x,\theta_y)$ is the many-body Berry curvature depending on the boundary condition twists:

$$F(\theta_x,\theta_y) = \mathrm{Im}\left(\left\langle\frac{\partial\Psi}{\partial\theta_y}\middle|\frac{\partial\Psi}{\partial\theta_x}\right\rangle - \left\langle\frac{\partial\Psi}{\partial\theta_x}\middle|\frac{\partial\Psi}{\partial\theta_y}\right\rangle\right). \tag{4.22}$$

Note that equation (4.21) reduces to equation (4.4) in the translationally invariant case. For the numerical computations, we use a discretized version [194]. The results for the disordered system are summarized in figure 4.7a. We find that the long-range tunneling stabilizes the topological phase for defect densities $\rho \lesssim 0.45$. The long-range tunneling $\sim|\mathbf{R}|^{-3}$ is found to significantly enhance the stability compared to a model with artificial truncation at the next-to-nearest neighbor level.

4.9 Edge states

One way to detect the topological band structure experimentally is to create a local excitation close to the edge of the system. In the topologically nontrivial phase, the excitation will move along the edge in a specific direction due to the chiral nature of the edge state, a behavior that can be used as an indication of the topological nature of the bands [56]. A convenient way to investigate the structure of the edge states is a cylindrical geometry which is infinite in one direction (x) and has a finite number of lattice sites in the other (y). Then, the momentum k_x in the infinite direction can still be used to characterize

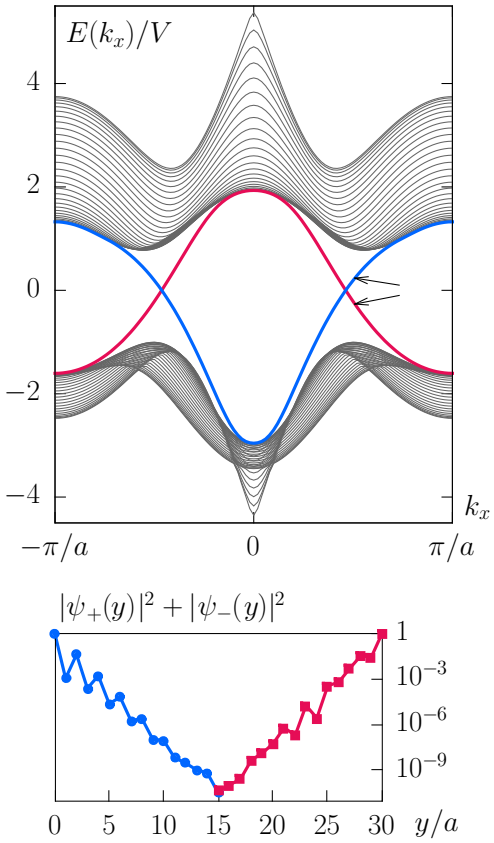

Fig. 4.8: Upper panel: Dispersion relation for the $|+\rangle$ and $|1\rangle$ states on a cylindrical square lattice geometry with infinite extent in the x direction and 31 sites in the y direction. As a function of the momentum k_x, there are 2×31 bands corresponding to two orbitals for each of the discrete sites in y direction. Four edge states cross the bandgap in the $C = 2$ phase (two for each edge), in accordance with the bulk-edge correspondence [33]. Lower panel: Exponentially decaying amplitude of the edge states at the two points indicated by the arrows. Due to the opposite group velocity on opposing sites of the cylinder, the two edge states have the same chirality.

the states. In figure 4.8 we show the spectrum for such a geometry in the $C = 2$ phase on the square lattice for the $|+\rangle, |1\rangle$ model. The remnants of the two-dimensional bulk bands are still visible as a projection consisting of a bundle of single one-dimensional bands. Four edge states cross the bandgap in accordance with the bulk-edge correspondence, as there are two states for each edge of the system. These would also be visible in a spectroscopic analysis, as a single mode between the broad continuum of the two bands. A characteristic property of edge states is the exponential decay from the boundary into the bulk of the system, see figure 4.8.

Figures 4.9a and 4.9b depict the two-dimensional structure of the edge-states in a small finite system for the square and honeycomb lattices. Figures 4.9c and 4.9d show the same system with a fraction of $\rho = 0.2$ of the lattice sites removed, demonstrating the robustness of the edge states against missing molecules. For more details on the edge states in our system, we refer to follow-up work by Weber [106].

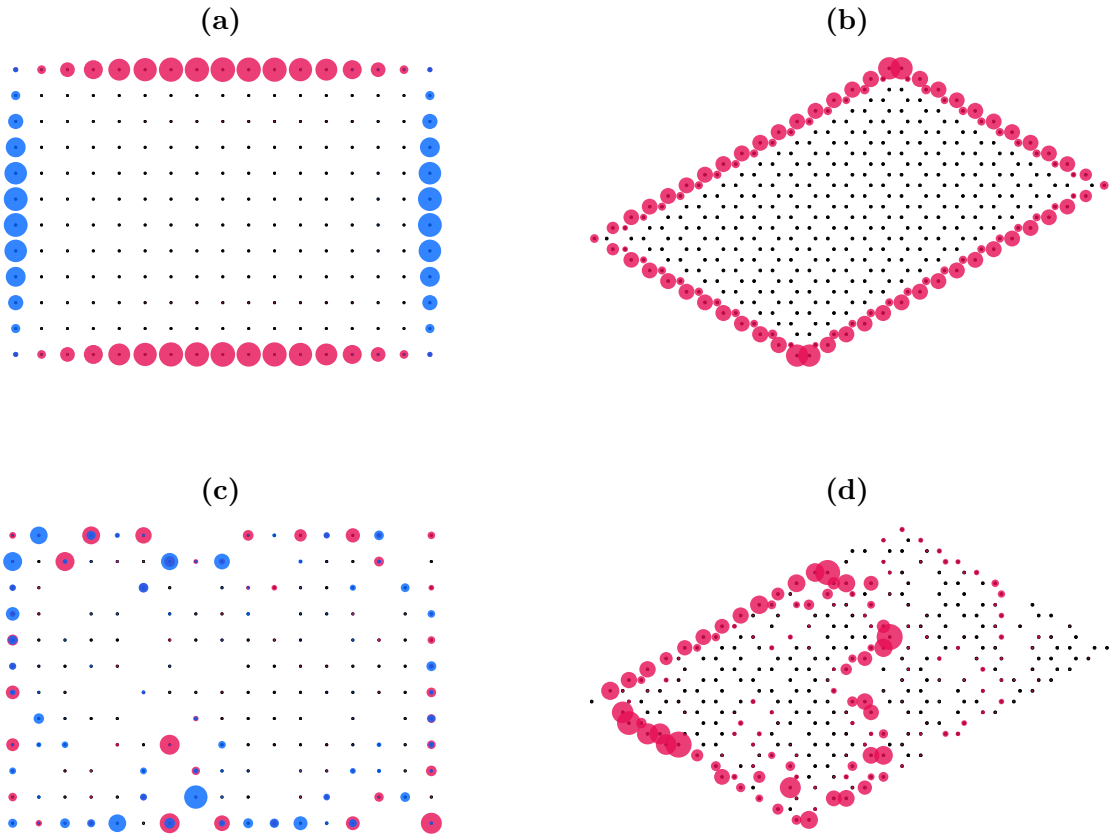

Fig. 4.9: Edge state amplitudes $|\psi_+(x,y)|^2$ (red) and $|\psi_-(x,y)|^2$ (blue) on finite rectangular patches. **(a)** On the square lattice for the $|+\rangle, |-\rangle$ model in the $C = 2$ phase with opposite orbitals on horizontal and vertical edges. The second edge state (not shown) has inverted orbitals. **(b)** Edge state on the honeycomb lattice between the lower two $C = -1$ and $C = 0$ bands, for the same parameters as in figure 4.7b. **(c)** Edge-state in the disordered system with a defect density of $\rho = 0.2$ on the square lattice for a certain disorder realization. **(d)** Edge state on the honeycomb lattice which travels along an interior edge which developed due to the missing lattice sites (defect density $\rho = 0.2$).

4.10 Many-body system

Finally, the most spectacular evidence of the topological nature would be the appearance of fractional Chern insulators in the interacting many-body system at a fixed density of excitations. In our system, the hard-core constraint naturally provides a strong on-site interaction for the bosons. In addition, the remaining static dipolar interactions are a tunable knob to control the interaction strength. The most promising candidate for a hard-core bosonic fractional Chern insulator in a band with $C = 2$ appears for a filling of $\nu = 2/3$, as suggested by numerical calculations [158, 160, 172], in agreement with the general classification scheme for interacting bosonic topological phases [195, 196]. A continuum trial wavefunction for such a state would be the Halperin $(l; m; n)$ state [156, 158, 166, 172, 197, 198] with

$$\Psi_{lmn} = \mathcal{N} \prod_{i \neq j} \left(z_i^{\downarrow} - z_j^{\downarrow}\right)^l \prod_{i \neq j} \left(z_i^{\uparrow} - z_j^{\uparrow}\right)^m \prod_{i,j} \left(z_i^{\uparrow} - z_j^{\downarrow}\right)^n \mathrm{e}^{-\frac{1}{4}\sum_{j,\alpha}\left|z_j^{\alpha}\right|^2} . \quad (4.23)$$

This state is a natural extension of the Laughlin wave function to a double-layer system where $z_i^{\downarrow} = x_i^{\downarrow} + i y_i^{\downarrow}$ and $z_i^{\uparrow}$ are the complex coordinates in the lower and upper layer and $\mathcal{N}$ is a normalization constant. In our system, the two layers are given by the deconstruction described in section 4.7. Since we are dealing with hard-core bosons, one would expect a $(2; 2; 1)$ state where $l = 2, m = 2$ is the lowest non-trivial state which is compatible with the bosonic statistics and $n = 1$ enforces the inter-layer hard-core constraint. For details about the hard-core bosonic Halperin state in a related system, see Yao et al. [172].

5

Realizing the Creutz ladder model with dipolar interactions

In this part we apply the ideas of chapter 4 to one-dimensional systems. Using a lattice with a double-chain structure, we show how dipolar exchange interactions can lead to the simulation of a homogeneous magnetic field and nontrivial topological band structures. The appearance of a constant magnetic field in a time-reversal invariant system is only possible because the system decomposes into two completely separate sectors. Each of them acquires a magnetic field of equal strength but opposite sign, in a similar way to the quantum spin Hall effect [48]. Furthermore, we show that each sector is a realization of a cross-linked ladder model introduced by Creutz [199–203]. This model has topological bands which can be perfectly flat. The topological properties and the resulting edge states are protected by inversion symmetry. We examine the properties of the double Creutz ladder and describe the modifications due to the long-range dipolar hoppings.

5.1 Setup

Consider the one-dimensional system depicted in figure 5.1. Single dipoles are located at each site of a double-chain lattice with spacing a and a separation of h between the two chains. The level scheme is the one discussed in chapter 4, but without any microwave field (see figure 4.2b on page 55). Every dipole initially

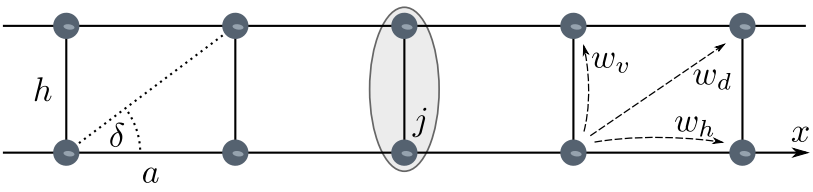

Fig. 5.1: Setup for the realization of the Creutz ladder. One dipole is pinned at each lattice site of a double chain with lattice spacing a in horizontal direction and a distance h between the two chains. A unit cell at site j includes both the upper and lower dipole. Horizontal (h), vertical (v) and diagonal (d) tunneling links are indicated for the idealized model with a cut-off $R_c = \sqrt{a^2 + h^2}$ and $t = 0$.

starts in the ground state $|0\rangle$ and can be excited into one of the two orbitals $|+\rangle$ or $|-\rangle$. We are only interested in the single-excitation dynamics and use the notation $|^{\alpha}\rangle_j = |\alpha\rangle_{j,\text{upper}} |0\rangle_{j,\text{lower}}$ to indicate a state at lattice site j where the dipole on the upper chain has been excited into the orbital $\alpha \in \{+, -\}$ and the dipole on the lower chain is still in the ground state. Conversely, $|_{\alpha}\rangle_j$ describes an excitation on the lower chain. Then, the four states $|^{+}\rangle_j, |^{-}\rangle_j, |_{+}\rangle_j, |_{-}\rangle_j$ define a complete local basis at lattice site j. Introducing hard-core bosons for each of these states and transforming to momentum space in the same way as in chapter 4, we find that the Bloch Hamiltonian takes the form

$$H(k) = \begin{pmatrix} -t\,\epsilon_k & w\,\epsilon_k & -t\,\eta_k^0 & w\,\eta_k^{-2} \\ w\,\epsilon_k & -t\,\epsilon_k & w\,\eta_k^{+2} & -t\,\eta_k^0 \\ -t\,\eta_k^0 & w\,\eta_k^{+2} & -t\,\epsilon_k & w\,\epsilon_k \\ w\,\eta_k^{-2} & -t\,\eta_k^0 & w\,\epsilon_k & -t\,\epsilon_k \end{pmatrix}. \tag{5.1}$$

Here, t is the orbital-preserving tunneling strength ($t \equiv t^+ = t^-$) and w is the orbital-changing tunneling rate, as defined in equation (4.11). The one-dimensional variant of the dipolar dispersion relation comes in two forms. The function

$$\epsilon_k = a^3 \sum_{x \neq 0} \frac{\mathrm{e}^{ikx}}{|x|^3} = 2 \sum_{j>0} \frac{\cos(kaj)}{|j|^3} \tag{5.2}$$

includes all processes within a single chain and the function

$$\eta_k^m = a^3 \sum_x \frac{\mathrm{e}^{ikx + im\phi_x}}{(x^2 + h^2)^{3/2}} = \frac{i^m}{(h/a)^3} + \sum_{j>0} \frac{2\cos(kaj + m\phi_j)}{(j^2 + (h/a)^2)^{3/2}} \tag{5.3}$$

covers all inter-chain processes. Here, $\phi_x = \arg(x + ih) = \phi_j = \arg(j + ih/a)$ is the polar angle of the position (x, h) of the dipole on the opposite chain. Note

that both functions are real-valued since $m = 0, \pm 2$. Moreover, $\epsilon_k = \epsilon_{-k}$ is symmetric in k whereas η_k^m satisfies the relation $\eta_k^m = \eta_{-k}^{-m}$.

5.2 Symmetries

The described system has an inversion symmetry (or 180° rotation symmetry), described by $H(-k) = \mathcal{P}H(k)\mathcal{P}^{-1}$, where the unitary operation $\mathcal{P} = \sigma_x \otimes \mathbb{1}$ flips the upper and lower chains. In addition, the system is time-reversal symmetric, i.e. $H(-k) = \mathcal{T}H(k)\mathcal{T}^{-1}$. Here, time-reversal is described by the anti-unitary operator $\mathcal{T} = U_{\mathcal{T}}\mathcal{K}$, where $\mathcal{K}$ is complex conjugation and $\mathcal{U}_{\mathcal{T}} = \mathbb{1} \otimes \sigma_x$ is a unitary operator that exchanges the two orbitals. The time-reversal operation satisfies $\mathcal{T}^2 = +\mathbb{1}$. The combination of these two symmetries gives rise to an operator $\mathcal{PT} = \sigma_x \otimes \sigma_x \mathcal{K}$ which commutes with the Bloch-Hamiltonian:

$$[\mathcal{PT}, H(k)] = 0 \qquad \Rightarrow \qquad [\sigma_x \otimes \sigma_x, H(k)] = 0. \tag{5.4}$$

The second commutation relation follows from the fact that $H(k)$ is real-valued. Using the knowledge about the symmetry, we can block-diagonalize the Hamiltonian. To do so, we change to a basis which diagonalizes the operator $\sigma_x \otimes \sigma_x$. We define

$$\begin{aligned} |\uparrow\rangle_\pm &= \frac{1}{\sqrt{2}}\left(|^+\rangle \pm |_-\rangle\right), \\ |\downarrow\rangle_\pm &= \frac{1}{\sqrt{2}}\left(|_+\rangle \pm |^-\rangle\right). \end{aligned} \tag{5.5}$$

Notice how these four states are invariant up to a phase under a combined flip of the chains $|^\alpha\rangle \leftrightarrow |_\alpha\rangle$ *and* the orbitals $+ \leftrightarrow -$. In the new basis $|\uparrow\rangle_-, |\downarrow\rangle_-, |\uparrow\rangle_+, |\downarrow\rangle_+$ the Hamiltonian takes the form

$$\begin{aligned} H(k) &= \begin{pmatrix} -t\,\epsilon_k - w\,\eta_k^{-2} & -t\,\eta_k^0 - w\,\epsilon_k & & \\ -t\,\eta_k^0 - w\,\epsilon_k & -t\,\epsilon_k - w\,\eta_k^{+2} & & \\ & & -t\,\epsilon_k + w\,\eta_k^{-2} & -t\,\eta_k^0 + w\,\epsilon_k \\ & & -t\,\eta_k^0 + w\,\epsilon_k & -t\,\epsilon_k + w\,\eta_k^{+2} \end{pmatrix} \\ &= -t\,\mathbb{1} \otimes M_k - w\,\sigma_z \otimes N_k \end{aligned} \tag{5.6}$$

where the left side of the tensor product selects the block (+ or − sign) and the right side selects $|\uparrow\rangle$ or $|\downarrow\rangle$. The two blocks $H_\mp(k) = -tM_k \mp wN_k$ are given in terms of the two matrices

$$M_k = \begin{pmatrix} \epsilon_k & \eta_k^0 \\ \eta_k^0 & \epsilon_k \end{pmatrix}, \qquad N_k = \begin{pmatrix} \eta_k^{-2} & \epsilon_k \\ \epsilon_k & \eta_k^{+2} \end{pmatrix}. \tag{5.7}$$

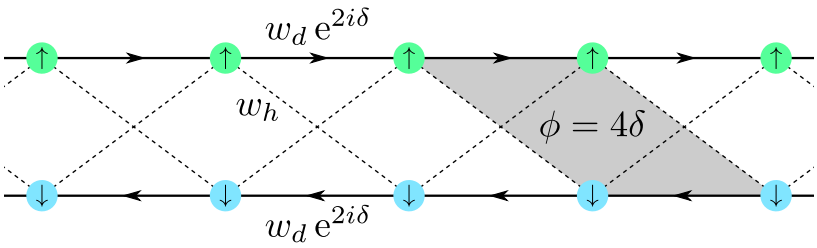

Fig. 5.2: Tunneling links for the two states $|\uparrow\rangle_+$ and $|\downarrow\rangle_+$. Notice that the two depicted chains live in an abstract space which is not to be confused with the real space of the original ladder. The tunneling along a single chain is determined by the *diagonal* elements of the real-space model while the inter-chain hopping is given by the *horizontal* elements. A constant magnetic flux of 4δ threads through each plaquette or unit cell in this abstract space.

5.3 Idealized model: mapping to the Creutz ladder

To understand the structure of the Hamiltonian, let us first assume that $t = 0$. We can focus on one of the blocks, say $H_+(k) = wN_k$ with the states $|\uparrow\rangle_+, |\downarrow\rangle_+$. Furthermore, we introduce a cut-off $R_c = \sqrt{a^2 + h^2}$ in the dipolar tunneling, such that only terms within one plaquette remain, see figure 5.1. We use the symbols $w_h = w$ to denote the horizontal (intra-chain) tunneling, $w_v = w\cot^3(\delta)$ for the vertical (inter-chain) coupling and $w_d = w\cos^3(\delta)$ for the strength of the diagonal (inter-chain) tunneling. The angle δ is given by $\tan\delta = h/a$.

We can visualize the model in the new basis by considering a ladder in an abstract space, where the upper chain is made up of $|\uparrow\rangle_+$ states and the lower chain is made up of $|\downarrow\rangle_+$ states. The resulting system with tunneling elements between the new basis states is shown in figure 5.2. Notice how the phases induced by the dipolar exchange interactions lead to the appearance of a *constant* artificial magnetic field with a flux of 4δ per unit cell, determined entirely by the geometric angle of the original real-space model.

It turns out that the model in this abstract space is identical to a cross-linked ladder model in a magnetic field; a system that has been introduced by Creutz [199]. For the simplified case we have considered so far ($t = 0$ and artificial cut-off), the parameters of the original model are given by $K = w_h = w, M = 0$ and $r = w_d/w_h = \cos^3(\delta)$. The magnetic flux per unit cell in the Creutz model is given by 2θ which translates to 4δ in our model.

By performing the summation for the dipolar dispersion relation up to the

cut-off radius explicitly, we get

$$\begin{aligned}\epsilon_k &= 2w_h\cos(ka),\\ \eta_k^m &= -w_v + 2w_d\cos(ka+m\delta), \qquad m=\pm 2.\end{aligned} \tag{5.8}$$

Using these expressions, we can write the lower block of the Hamiltonian as

$$\begin{aligned}H_+(k) &= \begin{pmatrix} -w_v + 2w_d\cos(ka-2\delta) & 2w_h\cos(ka) \\ 2w_h\cos(ka) & -w_v+2w_d\cos(ka+2\delta)\end{pmatrix}\\ &= +\mathbb{1}\ \times(-w_v+2w_d\cos(2\delta)\cos(ka))\\ &\quad +\sigma_z\times 2w_d\sin(2\delta)\sin(ka)\\ &\quad +\sigma_x\times 2w_h\cos(ka).\end{aligned} \tag{5.9}$$

From the expansion into the $\mathbb{1},\sigma_z,\sigma_x$ components, we can directly get the dispersion relation

$$\begin{aligned}E_\pm(k) = &-w_v + 2w_d\cos(2\delta)\cos(ka)\\ &\pm\sqrt{\left(2w_d\sin(2\delta)\sin(ka)\right)^2+\left(2w_h\cos(ka)\right)^2}.\end{aligned} \tag{5.10}$$

5.3.1 Perfectly flat bands

The Creutz ladder supports two perfectly flat bands. To see this, we first set the displacement between the two chains equal to the lattice constant, i.e. $h=a$. Then, the angle δ is given by $\pi/4$. This results in a flux of π per unit cell. In this case, equation (5.10) simplifies to

$$E_\pm(k) = -w_v \pm\sqrt{\left(2w_d\sin(ka)\right)^2+\left(2w_h\cos(ka)\right)^2}. \tag{5.11}$$

We can see that the system has flat bands if $w_d=w_h$, in which case the energy is given by $E_\pm(k)=-w_v\pm 2w_h$. The dispersion relation for $w_d=w_h$ and $w_d=2^{-3/2}w_h$ is shown in figure 5.3a.

In the flat band case, the horizontal tunneling elements in figure 5.2 are given by iw_h, whereas the cross-link tunneling elements are given by w_h. This leads to a destructive interference of all paths going from $|\uparrow\rangle_j$ to $|\uparrow\rangle_{j\pm2}$ or $|\downarrow\rangle_{j\pm2}$, as shown in figure 5.3b (we suppress the + index on the states as we only work in a single block). Consequently, the excitations are localized on single plaquettes. Each plaquette hosts two states

$$\left|P_j^\pm\right\rangle = \frac{1}{2}\left(i\,|\uparrow\rangle_j + |\downarrow\rangle_j \pm |\uparrow\rangle_{j+1} \pm i\,|\downarrow\rangle_{j+1}\right). \tag{5.12}$$

with exact energies $E_\pm=\langle P_j^\pm|H|P_j^\pm\rangle=-w_v\pm 2w_h$.

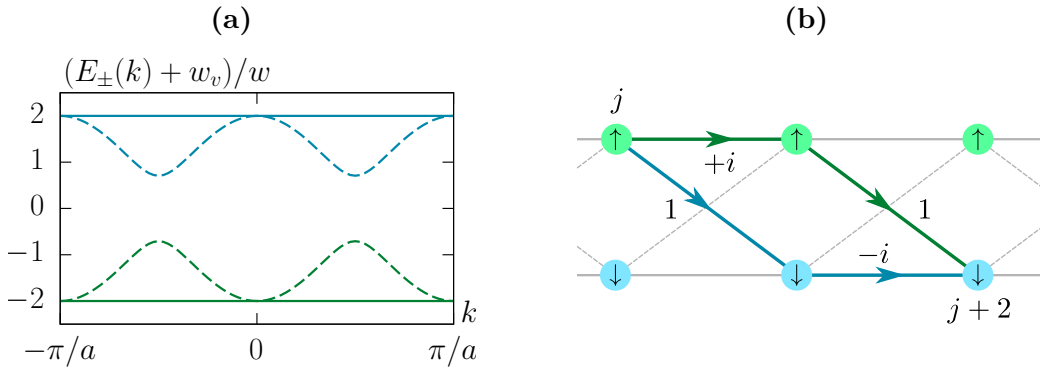

Fig. 5.3: (a) Dispersion relation for a single two-by-two block $H_+(k)$ for $\delta = \pi/4$ and $w_d = w_h$ (solid lines, perfectly flat bands) and $w_d = 2^{-3/2} w_h$, which is the generic value that is obtained for a simple setup where $\sqrt{2}$ is the distance along the diagonal. **(b)** Destructive interference of the two paths going from j to $j+2$ in the flat band limit for $\delta = \pi/4$ and $w_d = w_h$, cf. original figure by Creutz [199]. The indicated tunneling elements are in units of w.

5.3.2 Edge states

A finite system of length L has $2L$ lattice sites but only $L-1$ plaquettes. This means that only $2L-2$ states can be described in terms of the plaquette states $\left|P_j^{\pm}\right\rangle$. Consequently, two states are left over. These are the two edge states at each end of the ladder. In the flat-band limit, the left-hand side edge state is given by "half" a plaquette state

$$|E\rangle_+ = \frac{1}{\sqrt{2}} \left(|\uparrow\rangle_{1,+} + i\, |\downarrow\rangle_{1,+} \right) = \frac{1}{2} \left(|^+\rangle_1 + |_-\rangle_1 + i|_+\rangle_1 + i|^-\rangle_1 \right). \tag{5.13}$$

We can see that the excitation is shared among all four orbitals in the original basis. The localization at the edge is only exact in the flat-band limit. In the following, we look at the full model including the long-range dipolar hopping.

5.4 The full dipolar model

Leaving the idealized model, we remove the artificial cut-off and also add the orbital-preserving tunneling terms proportional to t. Then, we can write the block $H_+(k)$ from equation (5.6) as

$$\begin{aligned} H_+(k) &= -tM_k + wN_k \\ &= (-t\,\epsilon_k + w\,\eta_k^s)\,\mathbb{1} - w\,\eta_k^a\,\sigma_z + (w\,\epsilon_k - t\,\eta_k^0)\sigma_x. \end{aligned} \tag{5.14}$$

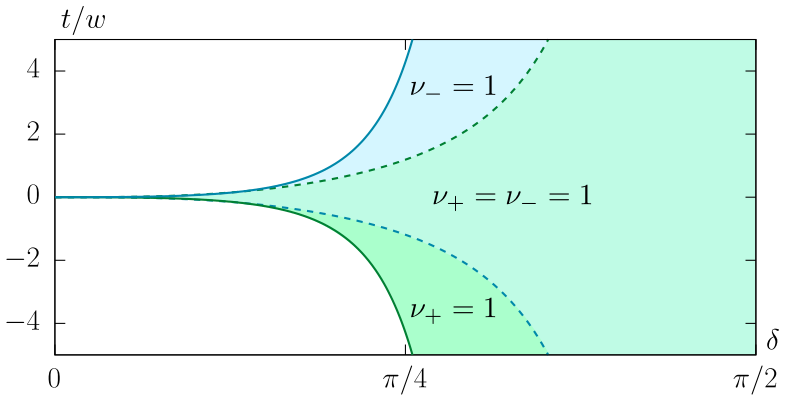

Fig. 5.4: Topological winding numbers of the double Creutz ladder system as a function of the angle $\delta = \arctan(h/a)$ and the ratio of tunneling rates t/w. The lines indicate band touchings at the $k = 0$ or $k = \pi/a$ point for the H_--ladder (blue) and H_+-ladder (green). The shaded areas have nontrivial winding numbers $\nu_\pm$ for one of the Creutz ladders or both of them.

We have introduced the symmetric and anti-symmetric combinations

$$\eta_k^s = \frac{1}{2}\left(\eta_k^2 + \eta_k^{-2}\right), \qquad \eta_k^a = \frac{1}{2}\left(\eta_k^2 - \eta_k^{-2}\right). \tag{5.15}$$

Then, the dispersion relation for the lower block is given by

$$E_\pm(k) = -t\,\epsilon_k + w\,\eta_k^s \pm \sqrt{(w\,\eta_k^a)^2 + (w\,\epsilon_k - t\,\eta_k^0)^2}. \tag{5.16}$$

By replacing w with $-w$, we immediately get the dispersion relation for the upper block $H_-(k)$, namely

$$E'_\pm(k) = -t\,\epsilon_k - w\,\eta_k^s \pm \sqrt{(w\,\eta_k^a)^2 + (w\,\epsilon_k + t\,\eta_k^0)^2}. \tag{5.17}$$

5.4.1 Topological structure

Following the strategy of section 4.4, equation (5.14) can be written in the form $H_+(k) = n_k^0 \cdot \mathbb{1} + \mathbf{n}_k \cdot \boldsymbol{\sigma}$. Here, $n_k^0 = \frac{1}{2}\operatorname{tr} H_+(k)$ is the diagonal part and $\mathbf{n}_k$ is given by

$$\mathbf{n}_k = \begin{pmatrix} w\,\epsilon_k - t\,\eta_k^0 \\ 0 \\ -w\,\eta_k^a \end{pmatrix}. \tag{5.18}$$

To determine the topological 'phase diagram', we look for points where $\mathbf{n}_k = 0$. The odd function η_k^a in the z-component can only be zero at $k = 0$ and $k = \pi/a$.

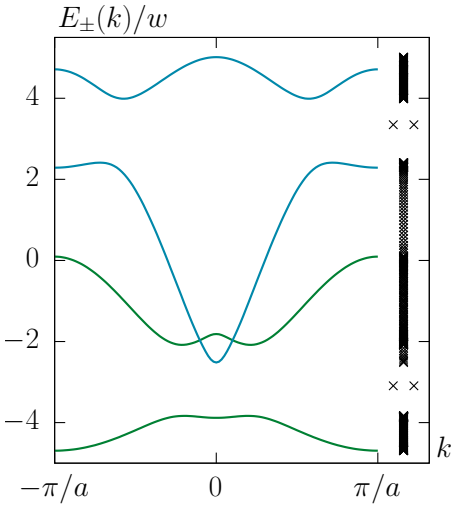

Fig. 5.5: Dispersion relation of the full dipolar model for realistic parameters with $h/a = 0.72$ and $t/w = 1/3$. Both ladders (blue and green bands) have winding numbers of $\nu = 1$. Note that the bands are allowed to cross due to the block-diagonal structure of the full Hamiltonian. The point-spectrum on the right side shows the energies of a finite ladder with the same parameters and a length of $L = 100$. Two edge states appear in the bandgap of each sector.

Consequently, the bandgap closes if $n_0^x = 0$ or $n_{\pi/a}^x = 0$, leading to the two conditions

$$\begin{aligned} t/w &= \frac{\epsilon_0}{\eta_0^0} = \frac{2\zeta(3)}{\eta_0^0}, \\ t/w &= \frac{\epsilon_{\pi/a}}{\eta_{\pi/a}^0} = -\frac{3\zeta(3)}{2\,\eta_{\pi/a}^0}. \end{aligned} \tag{5.19}$$

Similar conditions hold for the H_- block, where the signs are simply reversed. If t/w is not at one of the critical values, we can normalize the vector and define the winding number

$$\nu = \frac{1}{2\pi} \int_{-\pi/a}^{\pi/a} \mathrm{d}k \; (\hat{n}_k^x \partial_k \hat{n}_k^z - \hat{n}_k^z \partial_k \hat{n}_k^x)\,. \tag{5.20}$$

For values t/w between the two critical values, each ladder has a non-trivial winding number of $\nu = 1$. The resulting topological phase diagram for both sectors is shown in figure 5.4. It has overlapping regions where both of the ladders have topologically nontrivial winding numbers.

5.4.2 Symmetry protection

In both blocks of the full Hamiltonian, the symmetries found in section 5.2 are given by $\mathcal{P} = \sigma_x$ and $\mathcal{T} = \sigma_x \mathcal{K}$ with respect to the new basis. For the winding number in equation (5.20) to be a well-defined topological index, we rely on the fact that the $\mathbf{n}_k$ vector lies in the xz plane, i.e. $n_y(k) = 0$. As we shall see

shortly, this is a consequence of time-reversal symmetry and inversion symmetry. For a Hamiltonian $H(k) = \mathbf{n}_k \cdot \boldsymbol{\sigma}$, the two symmetries lead to the following conditions on the $\mathbf{n}_k$ vector:

$$\begin{aligned} \mathcal{P} \qquad\qquad & \qquad\qquad \mathcal{T} \\ n^x_{-k} &= +n^x_k, & n^x_{-k} &= +n^x_k, \\ n^y_{-k} &= -n^y_k, & n^y_{-k} &= +n^y_k, \\ n^z_{-k} &= -n^z_k, & n^z_{-k} &= -n^z_k. \end{aligned} \tag{5.21}$$

Consequently, n^x_k needs to be an even function of k, n^z_k needs to be an odd function of k and $n^y_k = 0$ for all k. If the condition $n^y_k = 0$ is violated by breaking one of the two symmetries, the winding number ν is no longer a useful index, as it can change without a closing of the bandgap.

5.4.3 Symmetry classification

One might wonder to which symmetry class our model belongs according to the general classification scheme [189–191]. We have seen that the full model is time-reversal symmetric with $\mathcal{T}^2 = +\mathbb{1}$. In the language of the classification scheme, the inversion symmetry can also be regarded as a time-reversal symmetry with $\mathcal{T}_2 = \mathcal{P}\mathcal{K}$ and $\mathcal{T}_2^2 = +\mathbb{1}$. This construction is possible because the Hamiltonian is real-valued. Considering just a single time-reversal symmetry is sufficient, as the combination of two time-reversal symmetries always gives rise to a unitary symmetry [191]. In our case this is just the operator $\sigma_x \otimes \sigma_x$ which we used to block-diagonalize the Hamiltonian. The full dipolar model consequently belongs to symmetry class AI, apparently without any topological index in one dimension [189–191]. Note that this is not in contradiction to the existence of the winding number defined above: the presence of inversion symmetry can lead to the appearance of additional symmetry-protected topological phases. In fact, adding inversion symmetry to the class AI leads to a $\mathbb{Z}$ topological index [204, 205].

At a certain fine-tuned point, the *idealized* model becomes "particle-hole" symmetric. To see this, consider a single block $H_+(k)$ from equation (5.9) at π-flux, i.e. $\delta = \pi/4$. Subtracting the constant energy shift $-w_v$, we have

$$H'_+(k) = H_+(k) + w_v\mathbb{1} = \begin{pmatrix} 2w_d \sin ka & 2w_h \cos ka \\ 2w_h \cos ka & -2w_d \sin ka \end{pmatrix}. \tag{5.22}$$

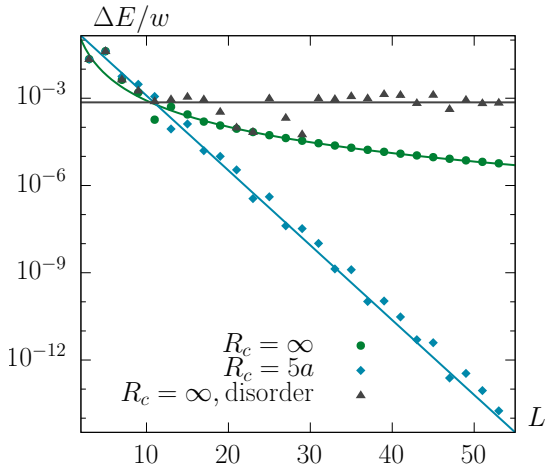

Fig. 5.6: Scaling behavior of the energy difference ΔE between the two edge states. In the full dipolar model without any cut-off ($R_c = \infty$), the energy scales algebraically with L^{-3} (green line is a fit to $\Delta E_1/L^3$). If a cut-off $R_c = 5a < L$ is introduced, the scaling turns exponential. For a disordered system with a random on-site potential $\mu_{\text{rand}}/w \approx 0.01$, the edge states split off with a constant ΔE.

This Hamiltonian satisfies $\mathcal{C}H'_+(k)\mathcal{C}^{-1} = -H'_+(-k)$ where $\mathcal{C}$ is the anti-unitary operator $\mathcal{C} = \sigma_z\mathcal{K}$ that squares to $+\mathbb{1}$. In combination with time-reversal symmetry, this also leads to a chiral symmetry $\mathcal{S} = i\sigma_y$ which anti-commutes with the Hamiltonian. Summarizing these results, we find that the idealized model at the point $\delta = \pi/4$ belongs to the symmetry class BDI, because $\mathcal{T}^2 = 1$ and $\mathcal{C}^2 = 1$ (same conclusion as Tovmasyan [201]). In a one-dimensional system, the BDI class has a $\mathbb{Z}$ topological index. However, since the "fake" particle-hole symmetry $\mathcal{C}$ only appears at a fine-tuned point in the presence of inversion symmetry, this topological index is symmetry-protected in the same way as the winding number of the full dipolar model. This is very similar to the case of the Su-Schrieffer-Heeger model [206], which can also be classified as BDI, but only in the presence of inversion symmetry [207].

5.4.4 Edge state properties

Figure 5.5 shows the dispersion relation of the full dipolar model in the region where $\nu_+ = \nu_- = 1$. The point spectrum for a finite ladder of length L shows the appearance of four edge states; two for each block of the Hamiltonian. In the following, we focus on the two edge states with the lower energy. In the presence of long-range dipolar hopping, the edge states are not exactly localized at the edge, but the amplitudes decay with $1/x^3$ into the bulk. In consequence, the coupling between the two edge states is proportional to $1/L^3$. This leads to an energy difference ΔE which scales like $1/L^3$ with the length of the ladder. Conversely, the edge state amplitude decays exponentially into the bulk if the dipolar interaction is artificially cut off at a finite distance $R_c < L$, leading to

an exponentially small energy difference. Finally, if the inversion symmetry is broken, the edge states split off independently of L with a constant energy offset ΔE. Such a symmetry breaking could be introduced by a random on-site potential, for example. The energy scaling results are summarized in figure 5.6.

5.4.5 Outlook

We have shown that dipolar exchange interactions can lead to the appearance of a constant magnetic flux in a very simple setup on a double-chain lattice. The artificial magnetic field can be tuned by changing a single geometric parameter: the height between the two chains. Moreover, the system can be understood as two decoupled copies of a Creutz-ladder with opposite-sign parameters. This model can have bands with topologically nontrivial winding numbers and edge states that are protected by inversion symmetry. The many-body physics of our model can be understood by studying hard-core bosons on the Creutz-ladder. In the short-range version, this has been subject of a work by Tovmasyan et al. [201].

6

Rydberg electron-induced atom losses

This chapter contains a brief description and a technical addendum to a side-project concerning a single Rydberg electron that is coupled to a Bose Einstein condensate [P3]. In the experiment, performed by Jonathan Balewski and coworkers, a single atom within a Rubidium condensate is excited to a high-n Rydberg state whose extent includes several thousands of ground state atoms. Due to the interaction with the ground state atoms, the electron creates excitations in the BEC which eventually can be measured as particle loss. Understanding the nature of the excitations and computing the particle losses is the scope of this chapter. For a detailed overview on this topic, see Balewski et al. [P3, 208] as well as Karpiuk et al. and Gaj et al. [209, 210].

6.1 Interaction between electron and ground state atoms

In the s-wave approximation, the contact interaction between the electronic density $\rho(\mathbf{r}) = |\Psi(\mathbf{r})|^2$ in the Rydberg ns state and the ground state atoms is described by the interaction potential $V(\mathbf{r}) = g\rho(\mathbf{r})$, where $g = 2\pi\hbar^2 a/\mu$ is the coupling constant that is determined by the electron-atom scattering length a and the reduced mass $\mu \approx m_e$. Within a local density approximation with a constant atomic density

$$n(\mathbf{r}) = \frac{1}{V}\sum_{\mathbf{p},\mathbf{q}} \mathrm{e}^{i\mathbf{q}\mathbf{r}}\, a^\dagger_{\mathbf{p}+\mathbf{q}} a_{\mathbf{p}} \tag{6.1}$$

with annihilation operators $a_{\mathbf{p}}$ and quantization volume V, the interaction can be expressed as a convolution in momentum space, where

$$H_{\text{int}} = g \int \mathrm{d}^3 r \, n(\mathbf{r})\rho(\mathbf{r}) = \frac{g}{V} \sum_{\mathbf{p},\mathbf{q}} a^\dagger_{\mathbf{p}+\mathbf{q}} a_{\mathbf{p}} \rho_{\mathbf{k}}. \tag{6.2}$$

Neglecting constant energy shifts and two-particle excitations, we can write the interaction in terms of Bogoliubov operators $b_{\mathbf{q}} = u_q a_{-\mathbf{q}} - v_q a^\dagger_{\mathbf{q}}$ and the BEC particle number N_0 as

$$H_{\text{int}} \approx \frac{g\sqrt{N_0}}{V} \sum_{\mathbf{q}\neq 0} \rho_{\mathbf{q}} \big(u_q - v_q\big)\big(b^\dagger_{\mathbf{q}} + b_{-\mathbf{q}}\big). \tag{6.3}$$

6.2 BEC excitations and atom losses

To estimate the number of excitations induced by the presence of the Rydberg electron which has a finite lifetime of $\tau = 1/\gamma$, we first consider the probability to excite a certain mode with quasi momentum $\mathbf{q}$, when a perturbation of the type $H_{\text{int}}\, \mathrm{e}^{-\gamma t}$ is applied. In lowest order we have

$$P_{0\to\mathbf{q}} = \left| -\frac{i}{\hbar} \int_0^\infty \mathrm{d}t \; \mathrm{e}^{i\omega_q t - \gamma t} \, \langle \mathbf{q} | H_{\text{int}} | 0 \rangle \right|^2. \tag{6.4}$$

Here, $|0\rangle$ describes the many particle ground state and $|\mathbf{q}\rangle = b^\dagger_{\mathbf{q}} |0\rangle$ is the excited state with energy

$$E_q = \hbar\omega_q = \sqrt{\epsilon_q^2 + 2n_0 g_c \epsilon_q}. \tag{6.5}$$

We have introduced the recoil energy $\epsilon_q = \hbar^2 q^2 / 2m_{\text{Rb}}$, the BEC density $n_0 = N_0/V$ and the atom-atom coupling constant $g_c = 4\pi\hbar^2 a_{\text{Rb}}/m_{\text{Rb}}$ with the s-wave scattering length a_{Rb}. For the probability we find

$$P_{0\to\mathbf{q}} = \frac{g^2 \rho^2_{\mathbf{q}}}{V^2\hbar^2} \int \mathrm{d}\omega \, S(\mathbf{q},\omega) \, |C(\omega)|^2 = \frac{g^2\rho^2_{\mathbf{q}}}{V^2\hbar^2} N_0 \frac{\epsilon_q}{E_q} \, |C(\omega_q)|^2 \,, \tag{6.6}$$

where $S(\mathbf{q},\omega) = N_0 \, \epsilon_q / E_q \cdot \delta(\omega - \omega_q)$ is the dynamic structure factor of the BEC and $C(\omega) = 1/(\gamma - i\omega)$ is the Fourier transform of the exponential decay. During the time-of-flight process, the atom-atom interactions quickly become negligible and the Bogoliubov modes are converted in to real particles. Using

$N = \sum_{\mathbf{k}} a_{\mathbf{k}}^\dagger a_{\mathbf{k}}$, we find that $\langle \mathbf{q}|N|\mathbf{q}\rangle - \langle 0|N|0\rangle = u_q^2 + v_q^2$ additional particles are in the excited state. The total number of lost atoms therefore be expressed as

$$L = \sum_{\mathbf{q}} P_{0\to\mathbf{q}}\,(u_q^2 + v_q^2). \tag{6.7}$$

Replacing the sum by an integral, we find

$$L = \frac{1}{2\pi^2}\frac{n_0 g^2}{\hbar^2}\int \mathrm{d}q\, q^2 \rho_q^2 \frac{1+(q\xi)^2}{2+(q\xi)^2}\,|C(\omega_q)|^2 \equiv \int \mathrm{d}q\, P(q)(u_q^2+v_q^2) \tag{6.8}$$

where $\xi = 1/\sqrt{8\pi n_0 a_{\mathrm{Rb}}}$ is the healing length of the condensate. For high principal quantum numbers we can use an asymptotic expression for the Fourier transform of the electronic density (see equation (6.23) for details)

$$\rho_q = J_0(qR_e/2)\,\mathrm{sinc}(qR_e/2) \tag{6.9}$$

where $R_e = 2n^2 a_0$ denotes the classical electron radius. Then, we find

$$L/\tau^2 = \frac{2}{\pi^2}\frac{n_0 g^2}{R_e^2\hbar^2}\int \mathrm{d}q\, J_0(qR_e/2)^2 \sin(qR_e/2)^2 \frac{1+(q\xi)^2}{2+(q\xi)^2}\frac{1}{1+\omega_q^2/\gamma^2}, \tag{6.10}$$

where we have separated the main dependency on the two experimentally accessible quantities on the left hand side. To understand what kind of excitations are generated by the Rydberg electron, figure 6.1 shows the excitation weight $P(q) \sim P_{0\to q} q^2$ as a function of q. The main excitation peak is located at $q \approx 2/R_e < 1/\xi$, which lies well in the phonon regime for all principal quantum numbers investigated in the experiment.

6.2.1 Refinements

Some experimental details require extensions to equation (6.10) given above. They are described in the following.

Atomic density: First, to account for density inhomogeneities due to the external potential in a simple way, we replace the BEC density n_0 by its mean value

$$\overline{n} = n_0\left[1 - \left(\frac{2R_e}{5R_\rho}\right)^2 - \left(\frac{R_e}{5R_z}\right)^2\right] \tag{6.11}$$

on a sphere of radius R_e centered in the middle of the cylindrical cloud with Thomas-Fermi radii R_ρ and R_z in radial and axial direction, respectively.

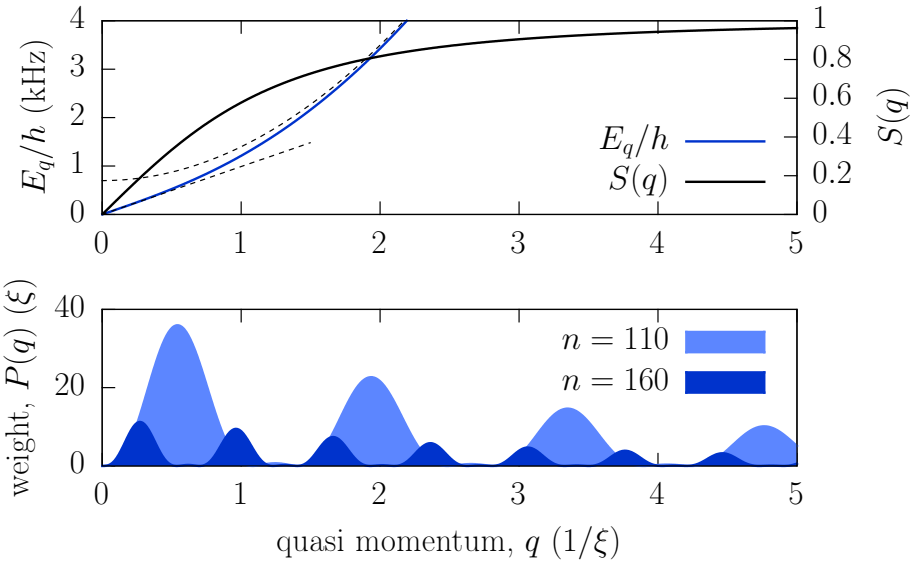

Fig. 6.1: Weight of the different excitation momenta q for two principal quantum numbers $n = 110$ and 160. The Bogoliubov excitation spectrum with linear and quadratic regimes is shown as a reference.

Field ionization: Second, in the experimental sequence, the interaction between the Rydberg electron and the ground state atoms is suddenly terminated after a certain time t_c at which the field ionization occurs. To account for this, the function $C(\omega)$ is modified accordingly:

$$|C(\omega)|^2 = \left| \int_0^{t_c} \mathrm{d}t \; \mathrm{e}^{i\omega t - \gamma t} \right|^2 = \frac{1 + \mathrm{e}^{-2\gamma t_c} - 2\,\mathrm{e}^{-\gamma t_c} \cos(\omega t_c)}{\gamma^2 + \omega^2}. \tag{6.12}$$

Lower cutoff: The last correction concerns the way the losses are detected in the experiment. In the absorption images, excitations at small momenta cannot be distinguished from the condensate fraction due to finite momentum components in the Thomas-Fermi profile. A lower cutoff may thus be introduced in the radial q integration. It turns out that this correction is negligible and almost all excitations will be detected as losses.

Finally, figure 6.2 shows the quantity L/τ^2 in a comparison between experiment and theory. The agreement is reasonably well if the measured lifetimes are taken into account (see also related work by Karpiuk et al. [209]).

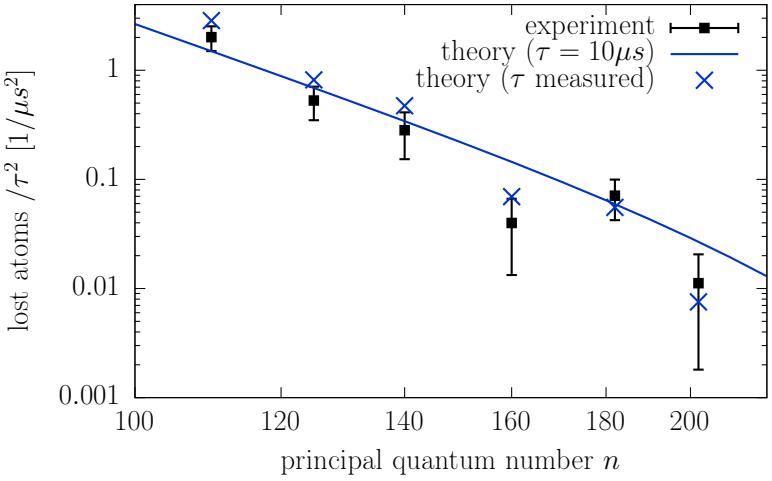

Fig. 6.2: Atom losses divided by the square of the Rydberg lifetime τ. Comparison between experiment [208] and theory. For the solid line, a lifetime of $\tau = 10\mu s$ is assumed while the crosses take the measured Rydberg lifetime into account.

6.3 Fourier transform of the Rydberg electronic density

To find the number of losses in equation (6.8), the Fourier transform of the electronic density in the Rydberg state is required. To calculate this quantity, we start with the wave function of the Hydrogen ns state which is given by

$$\Psi(r) = \frac{\mathrm{e}^{-\frac{r}{n}}}{\sqrt{\pi\, n^5}}\, L^1_{n-1}\left(\frac{2r}{n}\right). \tag{6.13}$$

In this section, we have set $a_0 = 1$ to avoid cluttering of notation. The three-dimensional Fourier transform for spherically symmetric functions is directly given by a Hankel transformation in the radial coordinate. With $\rho(r) = |\Psi(r)|^2$, we have

$$\begin{aligned}
\rho_q &= \int \mathrm{d}^3 r\ \mathrm{e}^{-i\mathbf{qr}}\, \rho(r) = \frac{4\pi}{q} \int_0^\infty \mathrm{d}r\, r \sin(qr)\rho(r) \\
&= \frac{4}{q\, n^5} \int_0^\infty \mathrm{d}r\, r \sin(qr)\, \mathrm{e}^{-\frac{2r}{n}}\ L^1_{n-1}\left(\frac{2r}{n}\right)^2 \\
&= \frac{1}{q\, n^3} \int_0^\infty \mathrm{d}x\, x \sin\left(\frac{qn}{2}x\right) \mathrm{e}^{-x}\ L^1_{n-1}(x)^2
\end{aligned} \tag{6.14}$$

where we have used the reduced length $x = \frac{2r}{n}$ in the last step.

6.3.1 Universal solution in the classical limit

For large $n \longrightarrow \infty$ we expect the Fourier transform ρ_q to be a universal function of the rescaled momentum $k = 2n^2 q$, where the factor $2n^2$ is the classical electron radius (in units of a_0). Using this transformation, we find

$$\rho_k = \frac{2}{kn} \int_0^\infty \mathrm{d}x\, x \sin\left(\frac{kx}{4n}\right) \mathrm{e}^{-x}\; L_{n-1}^1(x)^2\,. \tag{6.15}$$

With the explicit expression for the Laguerre polynomial

$$L_{n-1}^1(x) = \sum_{\alpha=1}^{n} \binom{n}{\alpha} \frac{(-x)^{\alpha-1}}{(\alpha-1)!} \tag{6.16}$$

we can expand the square $L_{n-1}^1(x)^2$:

$$\begin{aligned}\rho_k = \frac{2}{kn} \sum_{\alpha=1}^{n} \sum_{\beta=1}^{n} \frac{(-1)^{\alpha+\beta}}{(\alpha-1)!(\beta-1)!} \binom{n}{\alpha} \binom{n}{\beta} \\ \cdot \int_0^\infty \mathrm{d}x\, \sin\left(\frac{kx}{4n}\right) \mathrm{e}^{-x}\, x^{\alpha+\beta-1}.\end{aligned} \tag{6.17}$$

We can now evaluate the remaining integral

$$\begin{aligned}\int_0^\infty \mathrm{d}x\, \sin\left(\frac{kx}{4n}\right) \mathrm{e}^{-x}\, x^{\alpha+\beta-1} &= \mathrm{Im}\left[\int_0^\infty \mathrm{d}x\; \mathrm{e}^{-(1-ik/4n)x}\, x^{\alpha+\beta-1}\right] \\ &= \mathrm{Im}\left[\frac{(\alpha+\beta-1)!}{\left(1-\frac{ik}{4n}\right)^{\alpha+\beta}}\right]\end{aligned} \tag{6.18}$$

leading to

$$\begin{aligned}\rho_k = \frac{1}{2n^2} \sum_{\alpha=1}^{n} \sum_{\beta=1}^{n} (-1)^{\alpha+\beta} \frac{(\alpha+\beta-1)!}{(\alpha-1)!(\beta-1)!} \binom{n}{\alpha} \binom{n}{\beta} \\ \cdot \mathrm{Im}\left(\frac{1}{\kappa\,(1-i\kappa)^{\alpha+\beta}}\right)\end{aligned} \tag{6.19}$$

where we have defined $\kappa = \frac{k}{4n}$ to simplify the structure. We can now expand this expression into a series around $\kappa = 0$. All odd orders vanish identically. For even ν, the coefficient of ν-th order is given by

$$\rho_k^{(\nu)}/\nu! = \frac{(-1)^{\nu/2}}{2n^2(4n)^\nu(\nu+1)!} \sum_{\alpha=1}^{n} \sum_{\beta=1}^{n} \frac{(-1)^{\alpha+\beta}(\alpha+\beta+\nu)!}{(\alpha-1)!(\beta-1)!} \binom{n}{\alpha} \binom{n}{\beta}. \tag{6.20}$$

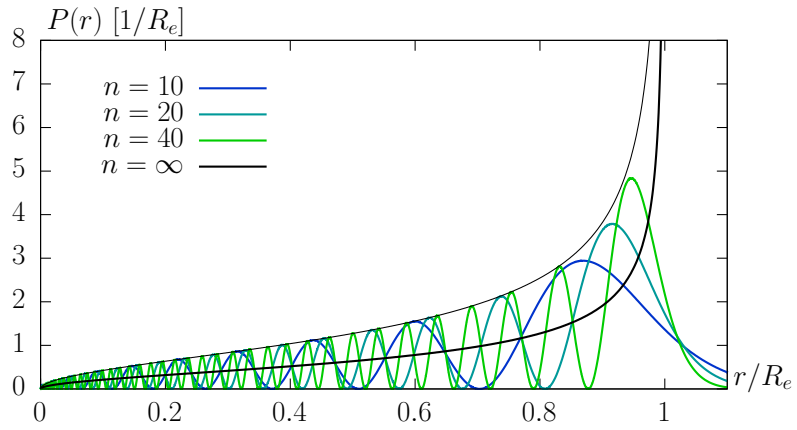

Fig. 6.3: Radial probability distribution $P_n(r)$ for principal quantum number $n = 10, 20$ and 40. The black solid line shows the classical probability distribution $P_\infty(r)$ which diverges at the classical turning point $R_e = 2n^2 a_0$. The envelope is given by $2P_\infty(r)$.

Finally, we can take the classical limit $n \longrightarrow \infty$, allowing us to express the double infinite series as

$$\rho_k^{(\nu)}/\nu! = \frac{(-1)^{\nu/2}}{(4n)^\nu(\nu+1)!}\binom{2\nu+1}{\nu}. \tag{6.21}$$

The power series in ν can now be summed to give the final result

$$\rho_k = \sum_{\nu=0,2,\ldots}^{\infty} \frac{(-1)^{\nu/2}}{(4n)^\nu(\nu+1)!}\binom{2\nu+1}{\nu}k^\nu = J_0\left(\frac{k}{2}\right)\mathrm{sinc}\left(\frac{k}{2}\right) \tag{6.22}$$

where J_0 is the zeroth-order Bessel function. Transforming back to the momentum variable q, we find a concise form for the Fourier transform of the electronic density in the classical limit:

$$\rho_q = J_0\left(qn^2\right)\mathrm{sinc}\left(qn^2\right). \tag{6.23}$$

6.3.2 Classical probability distribution

An interesting application of the expression for ρ_q in equation (6.23) is to derive the classical probability function of the Hydrogen atom. By Fourier transforming the universal function ρ_k back to real space we find

$$\rho(x) = \frac{1}{16\pi^2\, n^6\, x^{3/2}(1-x)^{1/2}} \tag{6.24}$$

as a function of the reduced coordinate $x = r/R_e = r/2n^2$. As expected, the probability distribution diverges at the classical turning point $x = r/R_e = 1$. It can easily be checked, that $\rho(x)$ is properly normalized:

$$4\pi \int_0^{R_e} \mathrm{d}r\, \rho(r/R_e) r^2 = 1. \tag{6.25}$$

The radial probability function is given by

$$P(r) = 4\pi\rho(r/R_e)r^2 = \frac{2}{\pi R_e}\sqrt{\frac{r/R_e}{1 - r/R_e}} \tag{6.26}$$

and is shown in figure 6.3, where it is compared with the exact expressions for a finite principal quantum number n.

A

Dipolar dispersion relation

A.1 Definition and properties

This appendix is concerned with the properties of the dipolar dispersion relation [P1, P6, 75]

$$\epsilon_{\mathbf{k}}^{m} = \sum_{j\neq 0} \frac{a^3}{|\mathbf{R}_j|^3} \, \mathrm{e}^{i\mathbf{k}\mathbf{R}_j + im\phi_j}, \qquad m \in \{0, \pm 2\} \tag{A.1}$$

on a general two-dimensional Bravais lattice. Here, a is the lattice constant, $\mathbf{R}_j = (X_j, Y_j)^t$ is the position of the j-th lattice site and $\phi_j = \arg(X_j + iY_j)$ is the polar angle in the lattice plane, i.e. the angle between the vector $\mathbf{R}$ and the positive x axis. Note that $\epsilon_{\mathbf{k}}^{\pm 2}$ changes under a redefinition of the angle $\phi_j \longrightarrow \phi_j + \phi_0$. The absolute value $\left|\epsilon_{\mathbf{k}}^{\pm 2}\right|$ is invariant, however. For the remainder of this section we will measure lengths in units of a and suppress the j index, such that

$$\epsilon_{\mathbf{k}}^{m} = \sum_{\mathbf{R}\neq 0} \frac{1}{R^3} \, \mathrm{e}^{i\mathbf{k}\mathbf{R} + im\phi_{\mathbf{R}}}, \tag{A.2}$$

where $R = |\mathbf{R}|$ and the sum runs over all lattice sites except the origin. Using $\phi_{-\mathbf{R}} = \phi_{\mathbf{R}} + \pi$ and the inversion symmetry of Bravais lattices, we can derive the following properties of the dispersion relation (m is always even):

$$\begin{aligned} \epsilon_{-\mathbf{k}}^{m} &= \epsilon_{\mathbf{k}}^{m}, \\ \epsilon_{\mathbf{k}}^{-m} &= \left(\epsilon_{\mathbf{k}}^{m}\right)^{*}. \end{aligned} \tag{A.3}$$

The second property also shows that $\epsilon_{\mathbf{k}}^{0} \in \mathbb{R}$.

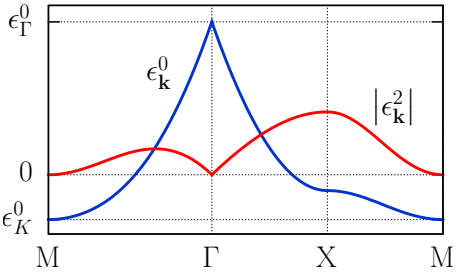

Fig. A.1: Plot of the function $\epsilon^m_{\mathbf{k}}$ on a high-symmetry path in the Brillouin zone of the square lattice. The linear behavior at $\mathbf{k} = \mathbf{\Gamma}$ is apparent as well as the zeros of $\epsilon^2_{\mathbf{k}}$ at $\mathbf{k} = \mathbf{\Gamma}, \mathbf{M}$.

A.2 Symmetries and zeros

Let $\mathcal{S}$ be a symmetry operation which leaves the lattice invariant, i.e. $\mathcal{S}\{\mathbf{R}\} = \{\mathbf{R}\}$. Since the scalar product is left invariant, we can derive the property

$$\epsilon^m_{\mathcal{S}\mathbf{k}} = \sum_{\mathbf{R}\neq 0} R^{-3}\, \mathrm{e}^{i\mathbf{k}\mathbf{R} + im\phi_{\mathcal{S}\mathbf{R}}}\,. \tag{A.4}$$

Now let $\mathcal{S} = C_p$ be a rotation by $2\pi/p$. Then, we find

$$\epsilon^m_{\mathcal{S}\mathbf{k}} = \mathrm{e}^{2\pi i m/p}\, \epsilon^m_{\mathbf{k}}. \tag{A.5}$$

If $\mathbf{k}^*$ is a high-symmetry point which is left invariant under the rotation, that is $\mathcal{S}\mathbf{k}^* = \mathbf{k}^* + \mathbf{G}$ with an arbitrary reciprocal lattice vector $\mathbf{G}$, we find $\epsilon^m_{\mathbf{k}^*} = \mathrm{e}^{2\pi i m/p}\, \epsilon^m_{\mathbf{k}^*}$, leading to a condition for zeros of the dispersion relation:

$$\epsilon^m_{\mathbf{k}^*} = 0 \qquad \text{if } m \notin p\mathbb{Z}. \tag{A.6}$$

For $m = \pm 2$, we can use any symmetry C_n with $n > 2$.

Triangular lattice: The points $\mathbf{\Gamma} = (0, 0)$ as well as $\mathbf{K} = (4\pi/3, 0)$ and $\mathbf{K}' = -\mathbf{K}$ are invariant under C_3 rotations. Therefore, $\epsilon^2_0 = \epsilon^2_{\mathbf{K}} = \epsilon^2_{\mathbf{K}'} = 0$ on the triangular lattice.

Square lattice: The points $\mathbf{\Gamma}$ and $\mathbf{M} = (\pi, \pi)$ are invariant under C_4 rotations, leading to the two zeros $\epsilon^2_0 = \epsilon^2_{\mathbf{M}} = 0$, see figure A.1.

A.3 Low-momentum behavior

For small $|\mathbf{k}| \ll 1$ we can make a crude approximation and replace the discrete Fourier series by a continuous Fourier transform (we will re-derive the results

in this section in a "cleaner" way later). We set $\mathbf{kR} = kR\cos(\phi - \psi)$ where $\phi \approx \phi_{\mathbf{R}}$ is the angle between $\mathbf{R}$ and the x-axis and ψ is the corresponding angle between $\mathbf{k}$ and the k_x-axis. Then

$$\begin{aligned}\epsilon_{\mathbf{k}}^m &= \sum_{\mathbf{R}\neq 0} R^{-3}\,\mathrm{e}^{i\mathbf{kR}+im\phi_{\mathbf{R}}} \approx \int_{R_c}^{\infty}\mathrm{d}R \int_0^{2\pi}\mathrm{d}\phi\ \mathrm{e}^{ikR\cos(\phi-\psi)+im\phi}/R^2 \\ &= k\,\mathrm{e}^{im\psi}\int_{z_c}^{\infty}\mathrm{d}z \int_0^{2\pi}\mathrm{d}\phi\ \mathrm{e}^{iz\cos(\phi)+im\phi}/z^2 \\ &= 2\pi k(-1)^{m/2}\,\mathrm{e}^{im\psi}\int_{z_c}^{\infty}\mathrm{d}z\, J_{|m|}(z)/z^2 \end{aligned} \tag{A.7}$$

where we have to introduce a lower cutoff R_c for the radial integration which we cannot determine (J_m is the Bessel function of the first kind). Consequently, this calculation is only useful if we find quantities like $\epsilon_{\mathbf{k}}^m - \epsilon_0^m$ which (a) allow us to safely take the limit $z_c = kR_c \longrightarrow 0$ while keeping R_c constant and (b) do not depend on R_c in this limit.

$m = 0$**:** In the case of $\epsilon_{\mathbf{k}}^0$, the integral in the expression

$$\epsilon_{\mathbf{k}}^0 \approx 2\pi k\int_{z_c}^{\infty}\mathrm{d}z\, J_0(z)/z^2 \tag{A.8}$$

diverges as z_c^{-1} in the limit $z_c \longrightarrow 0$. However, we can subtract this diverging part and calculate

$$\epsilon_{\mathbf{k}}^m - \frac{2\pi}{R_c} \approx 2\pi k\left[\int_{z_c}^{\infty}\mathrm{d}z\,\frac{J_0(z)}{z^2} - \frac{1}{z_c}\right] = -2\pi k, \tag{A.9}$$

giving us the correct expression for the linear part in k, i.e. $\epsilon_{\mathbf{k}}^0 = \epsilon_0^0 - 2\pi|\mathbf{k}|$.

$m = 2$**:** For any $|m| > 1$, the integral can be evaluated in the limit $z_c \longrightarrow 0$. We find

$$\epsilon_{\mathbf{k}}^m \approx \frac{2\pi(-1)^{m/2}}{m^2-1}k\,\mathrm{e}^{im\psi} \tag{A.10}$$

which allows us to determine $\epsilon_{\mathbf{k}}^{\pm 2} \approx -\frac{2\pi}{3}|\mathbf{k}|\,\mathrm{e}^{\pm 2i\psi}$.

A.4 Exact results and Ewald summation

This section is mainly of interest for a numerically efficient determination of the function $\epsilon_{\mathbf{k}}^m$ as well as a precise description of the low momentum behavior. To start, it is convenient to rewrite $\epsilon_{\mathbf{k}}^m$ such that the explicit angular dependence is removed from the sum. With $\mathbf{R} = (X, Y)^t$ and $\mathrm{e}^{im\phi_{\mathbf{R}}} = (X + iY)^m / R^m$ we can write

$$\begin{aligned}\epsilon_{\mathbf{k}}^m &= \sum_{\mathbf{R}\neq 0} \frac{(X+iY)^m}{R^{3+m}} \mathrm{e}^{i\mathbf{k}\mathbf{R}} = \sum_{\mathbf{R}\neq 0} \frac{(-i\partial_{k_x} + \partial_{k_y})^m}{R^{3+m}} \mathrm{e}^{i\mathbf{k}\mathbf{R}} \\ &= (-i)^m (\partial_{k_x} + i\partial_{k_y})^m \chi^{3+m}(\mathbf{k}) \end{aligned} \tag{A.11}$$

where $\chi^s(\mathbf{k}) = \sum_{\mathbf{R}\neq 0} \mathrm{e}^{i\mathbf{k}\mathbf{R}} R^{-s}$. In the following, we will see how to derive exact results for the function $\chi^{3+m}(\mathbf{k})$.

A.4.1 Exact values on the square lattice

At the $\mathbf{\Gamma} = (0, 0)$ point, the exact value of the function $\chi^s(0) = 4\beta(s/2)\zeta(s/2)$ can be expressed with the help of the Riemann ζ-function and the Dirichlet β-function [211]. This immediately leads to

$$\epsilon_0^0 = \chi^3(0) = 4\zeta(3/2)\beta(3/2) \approx 9.03. \tag{A.12}$$

To get the exact value at the $\mathbf{M} = (\pi, \pi)$ point, we denote the two sublattices of the bipartite square lattice by A and B. Both have a lattice constant of $\sqrt{2}$. By A, we denote the sublattice that includes the origin and B is the sublattice which includes the nearest neighbors of the origin. The full lattice is denoted by $A + B$. Then, $\epsilon_0^0 = \epsilon_0^0(A + B) = \epsilon_0^0(A) + \epsilon_0^0(B)$ and $\epsilon_{\mathbf{M}}^0 = \epsilon_0^0(A) - \epsilon_0^0(B)$. With $\epsilon_0^0(A) = 2^{-3/2}\epsilon_0^0$, we find

$$\epsilon_{\mathbf{M}}^0 = 2\epsilon_0^0(A) - \epsilon_0^0 = \left(1/\sqrt{2} - 1\right)\epsilon_0^0 \approx -2.65. \tag{A.13}$$

Using a similar technique with four sublattices, we can also find

$$\epsilon_{\mathbf{X}}^0 = \frac{1}{4}\left(1 - \sqrt{2}\right)\epsilon_0^0 \approx -0.94 \tag{A.14}$$

at the $\mathbf{X} = (\pi, 0)$ point. These exact values can serve as a useful benchmark for any kind of approximation.

A.4.2 Ewald summation

This section uses techniques introduced by Müller [124] and extends the results to $m \neq 0$. First, using the relation

$$\frac{1}{R^s} = \frac{1}{\Gamma(s/2)} \int_0^\infty \mathrm{d}\lambda\, \lambda^{s/2-1}\, \mathrm{e}^{-\lambda R^2}, \qquad s > 0 \tag{A.15}$$

we can rewrite

$$\begin{aligned} \chi^s(\mathbf{k}) &= \frac{1}{\Gamma(s/2)} \sum_{\mathbf{R}\neq 0} \left(\int_0^\eta + \int_\eta^\infty \right) \mathrm{d}\lambda\, \lambda^{s/2-1}\, \mathrm{e}^{-\lambda R^2 + i\mathbf{k}\mathbf{R}} \\ &= \frac{\eta^{s/2}}{\Gamma(s/2)} \sum_{\mathbf{R}\neq 0} \left(\int_1^\infty \mathrm{d}\lambda\, \lambda^{-s/2-1}\, \mathrm{e}^{-\eta R^2/\lambda} \right. \\ &\qquad \left. + \int_1^\infty \mathrm{d}\lambda\, \lambda^{s/2-1}\, \mathrm{e}^{-\eta\lambda R^2} \right) \mathrm{e}^{i\mathbf{k}\mathbf{R}} \end{aligned} \tag{A.16}$$

where we have substituted $\lambda \to \eta/\lambda$ in the first and $\lambda \to \eta\lambda$ in the second integral. The parameter $\eta > 0$ determines the border between the real-space and the k-space summation. Using the Poisson summation formula we transform

$$\sum_{\mathbf{R}\neq 0} \mathrm{e}^{-\eta R^2/\lambda + i\mathbf{k}\mathbf{R}} = \sum_{\mathbf{R}} (\dots) - 1 = \frac{\pi\lambda}{\eta} \sum_{\mathbf{q}} \mathrm{e}^{-\frac{\lambda}{4\eta}|\mathbf{q}+\mathbf{k}|^2} - 1, \tag{A.17}$$

which leads to

$$\begin{aligned} \chi^s(\mathbf{k}) = \frac{\eta^{s/2}}{\Gamma(s/2)} \left(\frac{\pi}{\eta} \sum_{\mathbf{q}} E_{s/2}\left(\frac{|\mathbf{q}+\mathbf{k}|^2}{4\eta} \right) - \frac{2}{s} \right. \\ \left. + \sum_{\mathbf{R}\neq 0} E_{1-s/2}\big(R^2\eta\big)\, \mathrm{e}^{i\mathbf{k}\mathbf{R}} \right). \end{aligned} \tag{A.18}$$

Here, we have introduced the exponential integral function

$$E_n(z) = \int_1^\infty \mathrm{d}t\, \frac{\mathrm{e}^{-zt}}{t^n}. \tag{A.19}$$

Both sums in equation (A.18) are fast-converging since high values of $\mathbf{q}$ and $\mathbf{R}$, respectively, are exponentially suppressed by E_n. Using this expression, we can accurately plot the function $\epsilon_{\mathbf{k}}^m$ in the Brillouin zone, see figure A.1.

A.4.3 Non-analytic behavior at low momenta

Setting $s = 3 \Leftrightarrow m = 0$ in equation (A.18), we find:

$$\epsilon^0_{\mathbf{k}} = \chi^3(\mathbf{k}) = 2\pi \left(\sum_{\mathbf{q}} E_{3/2}\left(\frac{|\mathbf{q}+\mathbf{k}|^2}{4\pi} \right) - \frac{2}{3} + \sum_{\mathbf{R}\neq 0} E_{-1/2}\left(\pi R^2\right) \mathrm{e}^{i\mathbf{k}\mathbf{R}} \right) \tag{A.20}$$

where we have explicitly chosen $\eta = \pi$. We can combine the two sums by writing the $\mathbf{q} = 0$ term separately and by making the replacement $\mathbf{q} \longrightarrow 2\pi\mathbf{R}$ for the rest of the $\mathbf{q}$-sum:

$$\begin{aligned} \epsilon^0_{\mathbf{k}} = {} & 2\pi E_{3/2}(k^2/4\pi) - \frac{4\pi}{3} \\ & + 2\pi \sum_{\mathbf{R}\neq 0} \left(E_{3/2}(\pi\,|\mathbf{R}+\mathbf{k}/2\pi|^2) + E_{-1/2}\left(\pi R^2\right) \mathrm{e}^{i\mathbf{k}\mathbf{R}} \right). \end{aligned} \tag{A.21}$$

Expanding the definitions of the exponential integral function, this can be written as

$$\begin{aligned} \epsilon^0_{\mathbf{k}} = {} & -2\pi|\mathbf{k}|\,\mathrm{erfc}(|\mathbf{k}|/2\sqrt{\pi}) + 4\pi \left(e^{-\frac{|\mathbf{k}|^2}{4\pi}} - \frac{1}{3} \right) \\ & + 2\pi \sum_{\mathbf{R}\neq 0} \int_1^\infty \mathrm{d}\lambda \left[\lambda^{-3/2}\, \mathrm{e}^{-\pi\lambda|\mathbf{R}+\mathbf{k}/2\pi|^2} + \lambda^{1/2}\, \mathrm{e}^{-\pi\lambda R^2 + i\mathbf{k}\mathbf{R}} \right]. \end{aligned} \tag{A.22}$$

This is the result stated in equation (2.3) on page 30. For general (even) m, i.e. for any odd $s = 3 + m$, we can expand

$$E_{s/2}(z) = \Gamma(1 - s/2)\, z^{s/2-1} + \sum_{k=0}^{\infty} \frac{(-1)^{k+1} z^k}{k!(1 + k - s/2)} \tag{A.23}$$

which means that the $\mathbf{q} = 0$ term has a contribution

$$\frac{\eta^{s/2}}{\Gamma(s/2)} \frac{\pi}{\eta} \Gamma(1 - s/2) \left(\frac{|\mathbf{k}|^2}{4\eta} \right)^{s/2-1} = \frac{2^{2-s}\pi\,\Gamma(1 - s/2)}{\Gamma(s/2)}\, |\mathbf{k}|^{s-2}. \tag{A.24}$$

Substituting $s = 3 + m$ and taking m derivatives, the prefactor of the linear term becomes

$$\frac{\pi\,(1+m)!!\,\Gamma[-(m+1)/2]}{\Gamma[(3+m)/2]} = 2\pi \frac{(-2)^{1+m/2}(1+m/2)!}{(2+m)!}. \tag{A.25}$$

For $m = 0$ the prefactor is given by -2π, see equation (A.22), and for $m = 2$ we find $2\pi/3$. Both results are in accordance with the estimation in section A.3.

B

Spin-wave analysis

We present the derivation of the spin wave excitation spectrum within the spin wave analysis for the system described in chapter 2. The basic approach is to start with the ground states exhibiting perfect order, which are the correct ground states for the classical model at the four points $\theta = 0, \pm\pi/2, \pi$. Then, we introduce bosonic creation and annihilation operators creating a spin excitation above the ground state according to the Holstein-Primakoff transformation. The spin Hamiltonian then reduces to a Bose-Hubbard model. In lowest order, we can ignore the interactions between the bosonic particles, and obtain a quadratic Hamiltonian in the bosonic operators, which is diagonalized using a Bogoliubov-Valantin transformation. The latter transformation deforms the ground state and introduces fluctuations into the system.

B.1 XY antiferromagnetic phase

In the following, we demonstrate the spin wave analysis for the most revealing case: the antiferromagnetic XY phase. The generalization to the other ground states is straightforward. Without loss of generality, we choose the antiferromagnetic order to point along the x direction. The square lattice is bipartite, and we denote the two sublattices as A and B. Then, the anti-ferromagnetic mean-field ground-state is given by $|G\rangle = \prod_{i\in A} |\leftarrow\rangle_i \prod_{j\in B} |\rightarrow\rangle_j$ with spins on sublattice A pointing in the negative x direction, i.e., $S^x |\leftarrow\rangle = -\hbar/2 |\leftarrow\rangle$, and spins on sublattice B pointing in the positive x direction ($S^x |\rightarrow\rangle = \hbar/2 |\rightarrow\rangle$).

Excitations on sublattice A are created by flipping a spin with the ladder operator $S^{x+} = S^z - iS^y$, while excitations on sublattice B are created via $S^{x-} = S^z + iS^y$. We apply a Holstein-Primakoff transformation to bosonic operators

$$\begin{aligned} S_i^z &= \frac{\hbar}{2}(a_i + a_i^\dagger)\,\varphi(n_i), \\ S_i^y &= \frac{\hbar}{2i}(a_i - a_i^\dagger)\,e^{i\mathbf{K}\mathbf{R}_i}\,\varphi(n_i), \end{aligned} \tag{B.1}$$

where the phase $e^{i\mathbf{K}\mathbf{R}_i} = e^{-i\mathbf{K}\mathbf{R}_i}$ accounts for the sublattice-dependent sign with $\mathbf{K} = (\pi/a, \pi/a)$. The factor $\varphi(n_i) = 1 - n_i$ is introduced to guarantee bosonic commutation relations for the operators a_i. Here, we are interested in the leading order of the spin wave expansion, and can therefore set $\varphi(n_i) \approx 1$. The bosonic operators reduce to

$$\begin{aligned} a_i &= (S^z + iS^y e^{i\mathbf{K}\mathbf{R}_i})/\hbar, \\ a_i^\dagger &= (S^z - iS^y e^{i\mathbf{K}\mathbf{R}_i})/\hbar, \end{aligned} \tag{B.2}$$

and the number operator $n_i = a_i^\dagger a_i = \frac{1}{2} + S_x e^{i\mathbf{K}\mathbf{R}_i}/\hbar$.

Expanding the spin Hamiltonian in terms of the bosonic operators leads to a Bose-Hubbard Hamiltonian for the spin wave excitations. In leading order, we can neglect the interactions between the bosons and obtain the quadratic Hamiltonian

$$\begin{aligned} H/J = &\sin\theta\,\epsilon_{\mathbf{K}} \left(\frac{3N}{4} - \frac{1}{2}\sum_i \left[a_i^\dagger a_i + a_i a_i^\dagger\right] \right) \\ &+ \frac{1}{4}\sum_{i\neq j} \frac{\chi_{ij}\left(a_i^\dagger a_j + a_i a_j^\dagger\right) + \eta_{ij}\left(a_i a_j + a_i^\dagger a_j^\dagger\right)}{|\mathbf{R}_{ij}/a|^3} \end{aligned} \tag{B.3}$$

with $\mathbf{R}_{ij} = \mathbf{R}_i - \mathbf{R}_j$, N the number of lattice sites, and the coupling the terms $\chi_{ij} = \cos\theta + \sin\theta e^{i\mathbf{K}\mathbf{R}_{ij}}$ and $\eta_{ij} = \cos\theta - \sin\theta e^{i\mathbf{K}\mathbf{R}_{ij}}$ including the anti-ferromagnetic ordering. Introducing the Fourier representation

$$a_i = \frac{1}{\sqrt{N}}\sum_{\mathbf{q}} a_{\mathbf{q}} e^{-i\mathbf{q}\mathbf{R}_i}, \tag{B.4}$$

the terms involving the bosonic operators in equation (B.3) reduce to

$$\begin{aligned} \frac{1}{4}\sum_{\mathbf{q}} \Big[&\left(\cos\theta\,\epsilon_{\mathbf{q}} + \sin\theta\,\epsilon_{\mathbf{q}+\mathbf{K}} - 2\sin\theta\epsilon_{\mathbf{K}}\right)\left(a_{\mathbf{q}}^\dagger a_{\mathbf{q}} + a_{\mathbf{q}} a_{\mathbf{q}}^\dagger\right) \\ &+ \left(\cos\theta\,\epsilon_{\mathbf{q}} - \sin\theta\,\epsilon_{\mathbf{q}+K}\right)\left(a_{\mathbf{q}} a_{-\mathbf{q}} + a_{\mathbf{q}}^\dagger a_{-\mathbf{q}}^\dagger\right)\Big]. \end{aligned} \tag{B.5}$$

The diagonalization of this Hamiltonian is straightforward using a standard Bogoliubov transformation with $b_{\mathbf{q}}^\dagger = u_{\mathbf{q}}\, a_{\mathbf{q}}^\dagger - v_{\mathbf{q}}\, a_{-\mathbf{q}}$. Then, the Hamiltonian takes the form

$$H = \frac{3JN \sin\theta\, \epsilon_{\mathbf{K}}}{4} + \sum_{\mathbf{q}} E_{\mathbf{q}}^{\text{XY-AF}} \left(b_{\mathbf{q}}^\dagger b_{\mathbf{q}} + \frac{1}{2} \right) \tag{B.6}$$

with the spin-wave excitation spectrum $E_{\mathbf{q}}^{\text{XY-AF}}$. In addition, the coefficients for the Bogoliubov transformation are given by

$$u_{\mathbf{q}}, v_{\mathbf{q}} = \pm \sqrt{\frac{1}{2} \left(\frac{\cos\theta\, \epsilon_{\mathbf{q}} + \sin\theta\, (\epsilon_{\mathbf{q}+K} - 2\epsilon_{\mathbf{K}})}{2\, \mathcal{E}_{\mathbf{q}}} \pm 1 \right)}, \tag{B.7}$$

with $\mathcal{E}_{\mathbf{q}} \equiv E_{\mathbf{q}}^{\text{XY-AF}}/J$. The property $u_{\mathbf{q}}^2 - v_{\mathbf{q}}^2 = 1$ asserts that the transformation is canonical. In addition, the ground state obeys the condition $b_{\mathbf{q}} |\text{vac}\rangle = 0$, and the ground state energy per spin at zero temperature $T = 0$ reduces to $e_{\text{XY-AF}}$, see table 2.1.

We are now able to validate the spin wave approach self-consistently: the deformation of the ground state by the spin wave analysis provides a suppression Δm of the anti-ferromagnetic order $m \equiv \Delta m - \frac{1}{2} = \left\langle S_i^x e^{i\mathbf{K}\mathbf{R}_i} \right\rangle / \hbar$, given by

$$\Delta m = \int \frac{\mathrm{d}\mathbf{q}}{v_0} \left\langle a_{\mathbf{q}}^\dagger a_{\mathbf{q}} \right\rangle = \int \frac{\mathrm{d}\mathbf{q}}{v_0} \left[v_{\mathbf{q}}^2 + (2v_{\mathbf{q}}^2 + 1) f_{\mathbf{q}} \right], \tag{B.8}$$

where $f_{\mathbf{q}} = \left\langle b_{\mathbf{q}}^\dagger b_{\mathbf{q}}^\dagger \right\rangle = \left[\exp(E_{\mathbf{q}}^{\text{XY-AF}}/T) - 1 \right]^{-1}$ accounts for the thermal occupation of the spin waves. At zero temperature $T = 0$, this expression converges and we obtain $\Delta m \approx 0.03$ for $\theta = \tilde{\theta}_c$ as well as $\Delta m = 0.39$ for $\theta \approx \frac{\pi}{4}$. In turn, at finite temperatures $T > 0$, the low momentum behavior of the integrand scales as $|\mathbf{q}|^{-2}$, and therefore Δm diverges logarithmically: the long range order is destroyed by the thermal spin wave fluctuations, and gives rise to the well known quasi long-range order in analogy to short range XY models.

B.2 Correlation functions

Finally, the spin wave analysis also allows us to analyze the correlation functions $c_{\alpha\alpha}(\mathbf{R}_{ij}) = \langle S_i^\alpha S_j^\alpha e^{i\mathbf{K}\mathbf{R}_{ij}} \rangle$. Using the translational invariance of our system, the correlation functions reduce to

$$c_{\alpha\alpha}(\mathbf{r}) = \int \frac{\mathrm{d}\mathbf{q}}{v_0}\, c_{\alpha\alpha}(\mathbf{q} + \mathbf{K})\, e^{-i\mathbf{q}\mathbf{r}} \tag{B.9}$$

with $c_{\alpha\alpha}(\mathbf{q}) = \langle S^\alpha_{\mathbf{q}} S^\alpha_{-\mathbf{q}} \rangle$. Combining the Holstein Primakoff transformation from equation (B.1) and the Bogoliubov transformation, the correlation functions can be expanded in terms of the coefficients $u_{\mathbf{q}}$ and $v_{\mathbf{q}}$ as

$$\begin{aligned} c_{zz}(\mathbf{q}+\mathbf{K}) &= \frac{1}{4}(u_{\mathbf{q}+\mathbf{K}} + v_{\mathbf{q}+\mathbf{K}})^2 \coth\left(\frac{J\mathcal{E}_{\mathbf{q}}}{2T}\right), \\ c_{yy}(\mathbf{q}+\mathbf{K}) &= \frac{1}{4}(u_{\mathbf{q}} - v_{\mathbf{q}})^2 \coth\left(\frac{J\mathcal{E}_{\mathbf{q}}}{2T}\right). \end{aligned} \tag{B.10}$$

The long distance behavior $|\mathbf{r}| \to \infty$ of the correlation function is determined by the low momentum behavior of the above expressions

$$\begin{aligned} (u_{\mathbf{q}+\mathbf{K}} + v_{\mathbf{q}+\mathbf{K}})^2 &\sim |\mathbf{q}| + \text{const.} \\ (u_{\mathbf{q}} - v_{\mathbf{q}})^2 &\sim \frac{1}{|\mathbf{q}|} \end{aligned} \tag{B.11}$$

and describes the leading non-analytic part. The latter can be replaced using the following relation, which derives via an Ewald summation,

$$|\mathbf{q}|^\gamma \sim \sum_{j\neq 0} \frac{e^{i\mathbf{q}\mathbf{R}_j}}{|\mathbf{R}_j|^{2+\gamma}} \tag{B.12}$$

for $|\mathbf{q}| \to 0$ and $\gamma > -2$; (for $\gamma = 0, 2, 4, \ldots$ the left side is replaced by $|\mathbf{q}|^\gamma \log|\mathbf{q}|$). At zero temperature $T = 0$, the integration in equation (B.9) is straightforward and provides the scaling behavior $c_{zz}(\mathbf{r}) \sim |\mathbf{r}|^{-3}$ and $c_{yy}(\mathbf{r}) \sim |\mathbf{r}|^{-1}$.

C

Classical dipolar XY model

The classical XY model with ferromagnetic long-range dipolar couplings is given by

$$H = -Ja^3 \sum_{i \neq j} \frac{\mathbf{S}_i \cdot \mathbf{S}_j}{|\mathbf{R}_i - \mathbf{R}_j|^3} = -J \sum_{i \neq j} \frac{\cos(\theta_i - \theta_j)}{|\mathbf{r}_{ij}|^3}. \tag{C.1}$$

Here, $J > 0$ is the coupling constant, $\mathbf{S}_i = (\cos\theta_i, \sin\theta_i)^t$ are classical spins restricted to two dimensions and $\mathbf{r}_{ij} = (\mathbf{R}_i - \mathbf{R}_j)/a$ is the dimensionless relative distance, used for conciseness.

C.1 High temperature expansion

With the reduced inverse temperature $\beta = J/kT$, we can write the partition function as

$$Z = \int \prod_k \frac{\mathrm{d}\theta_k}{2\pi} \exp\left(\beta \sum_{i \neq j} \cos(\theta_i - \theta_j) |\mathbf{r}_{ij}|^{-3}\right). \tag{C.2}$$

In the high temperature limit $\beta \ll 1$, keeping only linear terms in β, the two-point correlation function $\langle \mathbf{S}_\alpha \mathbf{S}_\beta \rangle$ is given by

$$\begin{aligned} \langle \mathbf{S}_\alpha \mathbf{S}_\beta \rangle &= \langle \cos(\theta_\alpha - \theta_\beta) \rangle \\ &= \frac{1}{Z} \int \prod_k \frac{\mathrm{d}\theta_k}{2\pi} \cos(\theta_\alpha - \theta_\beta) \prod_{i \neq j} \left(1 + \beta \cos(\theta_i - \theta_j) |\mathbf{r}_{ij}|^{-3}\right) \end{aligned} \tag{C.3}$$

After integration over all angles, only two terms in the expansion of the product over $i \neq j$ contribute to the lowest order: $\beta \cos(\theta_\alpha - \theta_\beta)|\mathbf{r}_{\alpha\beta}|^{-3}$ and $\beta \cos(\theta_\beta - \theta_\alpha)|\mathbf{r}_{\beta\alpha}|^{-3}$. Then, the correlation function is given by

$$\langle \mathbf{S}_\alpha \mathbf{S}_\beta \rangle = \frac{2\beta}{Z} \int \prod_k \frac{\mathrm{d}\theta_k}{2\pi} \cos(\theta_\alpha - \theta_\beta)^2 \, |\mathbf{r}_{\alpha\beta}|^{-3} = \frac{\beta}{Z} \frac{1}{|\mathbf{r}_{\alpha\beta}|^3} = \frac{\beta}{|\mathbf{r}_{\alpha\beta}|^3}. \tag{C.4}$$

In the last step, we have used that $Z = 1 + \mathcal{O}(\beta^3)$, as the smallest loop includes three terms.

D

Harmonic oscillator matrix elements of the dipolar interaction

D.1 Talmi-Moshinsky transformation

In this section, we show how to simplify the matrix elements of the dipolar interaction $V_{ijkl} = \langle ij|V_{\mathrm{dd}}|kl\rangle$ with each index $ijkl$ representing a set of 2D harmonic oscillator quantum numbers $i = (n_i, m_i, \sigma_i)$ and

$$V_{\mathrm{dd}}(R,\phi) = \frac{C_{\mathrm{dd}}}{R^3}\left[\sigma_1^z\sigma_2^z - (\sigma_1^+\sigma_2^- + 3\,\mathrm{e}^{2i\phi}\,\sigma_1^-\sigma_2^- + \mathrm{h.c.})\right] \tag{D.1}$$

the dipolar interaction in terms of $\mathbf{R} = \mathbf{R}_1 - \mathbf{R}_2 = (R\cos\phi, R\sin\phi)$, the relative vector between the two particles and its polar coordinates. The spin-part is easily resolved and we can concentrate on matrix elements of the form

$$V^{\Delta m} \equiv \langle n_1' m_1' n_2' m_2'|\frac{\mathrm{e}^{i\Delta m\,\phi}}{R^3}|n_1 m_1 n_2 m_2\rangle \tag{D.2}$$

with the difference in angular momentum $\Delta m = 0, \pm 2$. It is useful to change the basis to center-of-mass and relative coordinate states with

$$\mathbf{Q} = \frac{\mathbf{R_1} + \mathbf{R_2}}{\sqrt{2}}, \qquad \mathbf{q} = \frac{\mathbf{R_1} - \mathbf{R_2}}{\sqrt{2}}. \tag{D.3}$$

Note the symmetric definition with the additional factor of $1/\sqrt{2}$ compared to the usual definition of the relative vector. Due to the quadratic character

of the potential, the new degrees of freedom $\mathbf{Q}$ and $\mathbf{q}$ are subject to the same harmonic potential. Thus, the product state $|n_1 m_1 n_2 m_2\rangle = |n_1 m_1\rangle\,|n_2 m_2\rangle$ can be decomposed in terms of harmonic oscillator states $|NM\rangle\,|nm\rangle$ of the $\mathbf{Q}, \mathbf{q}$ coordinates via

$$|n_1 m_1 n_2 m_2\rangle = \sum_{N,M,n,m} T_{NMnm}^{n_1 m_1 n_2 m_2}\,|NMnm\rangle \tag{D.4}$$

where the $T_{NMnm}^{n_1 m_1 n_2 m_2}$ are called Talmi-Moshinsky coefficients [212, 213]. Since the center-of-mass is not affected by the interaction, the relevant matrix elements are

$$\langle n'm'|\frac{\mathrm{e}^{i\Delta m\phi}}{(\sqrt{2}q)^3}|nm\rangle = \delta_{m+\Delta m,m'}\int_0^\infty \mathrm{d}q\,\frac{R_{n'}^{m'}(q)R_n^m(q)\,q}{\left(\sqrt{2}q\right)^3} \tag{D.5}$$

where the radial functions R_n^m are given in terms of the generalized Laguerre polynomials $L_n^{|m|}$ as

$$R_n^m(q) = \sqrt{\frac{2n!}{(n+|m|)!}}\,q^{|m|}\exp\left(-\frac{q^2}{2}\right)\cdot L_n^{|m|}(q^2). \tag{D.6}$$

The matrix element $V^{\Delta m}$ is thus given by

$$V^{\Delta m} = \sum_{N,M,n,n',m} (T^*)_{NMn'(m+\Delta m)}^{n_1' m_1' n_2' m_2'}\cdot T_{NMnm}^{n_1 m_1 n_2 m_2}\cdot\int_0^\infty \mathrm{d}q\,\frac{R_{n'}^{m+\Delta m}(q)R_n^m(q)\,q}{\left(\sqrt{2}q\right)^3}. \tag{D.7}$$

where the remaining integral can be calculated analytically for specific values of n, n', m and Δm.

D.2 Lowest Landau level

In the lowest Landau level where $n_i = 0$ for all particles, this expression can be further simplified. The decomposition of a state $|0m_1 0m_2\rangle$ into relative and center of mass coordinates shows that only $|0M0m\rangle$ states appear due to energy conservation. If we consider a single spin component, the only relevant matrix element is the $\sigma_i^z\sigma_j^z$ part with $\Delta m = 0$ and

$$V^0 = 2^{-3/2}\sum_{M,m}(T^*)_{Mm}^{m_1' m_2'}\cdot T_{Mm}^{m_1 m_2}\langle m|q^{-3}|m\rangle. \tag{D.8}$$

For $m \geq 0$ the integration yields

$$\langle m|q^{-3}|m\rangle = \frac{2}{m!}\int_0^\infty \mathrm{d}q\, q^{2m-2}\,\mathrm{e}^{-q^2} = \frac{\Gamma\left(m-\frac{1}{2}\right)}{\Gamma\left(m+1\right)} \tag{D.9}$$

For $m = 0$, the integration diverges as the integrand behaves like q^{-2} for small q. However, if we consider the antisymmetrized matrix element

$$\overline{V}_{m_1',m_2',m_1,m_2} \equiv V_{m_1',m_2',m_1,m_2} - V_{m_2',m_1',m_1,m_2}, \tag{D.10}$$

the diverging term for $m = 0$ cancels, as any of the other even-m terms, and we are left with

$$\overline{V}_{m_1',m_2',m_1,m_2} = 2^{-1/2}\sum_{m=1,3,\ldots}^{m_1+m_2} (T^*)^{m_1'm_2'}_{Mm}\cdot T^{m_1m_2}_{Mm}\frac{\Gamma\left(m-\frac{1}{2}\right)}{\Gamma\left(m+1\right)} \tag{D.11}$$

where $m_1 + m_2 = m_1' + m_2'$ and $M = m_1 + m_2 - m$. The Talmi-Moshinsky coefficients in the lowest Landau level are given by

$$T^{m_1m_2}_{Mm} = \left(\frac{-1}{\sqrt{2}}\right)^{m+m_1}\sqrt{\frac{m_1!\,m_2!}{m!\,M!}}\sum_{k=0}^{m_1}(-1)^k\binom{M}{k}\binom{m}{m_1-k} \tag{D.12}$$

Bibliography

[P1] D. Peter, S. Müller, S. Wessel, and H. P. Büchler. "Anomalous Behavior of Spin Systems with Dipolar Interactions". Phys. Rev. Lett. **109** (2012), 025303. arXiv: 1203.1624 (cit. on pp. 15, 29, 59, 89).

[P2] D. Peter, K. Pawłowski, T. Pfau, and K. Rzażewski. "Mean-field description of dipolar bosons in triple-well potentials". J. Phys. B **45** (2012), 225302. arXiv: 1201.2615.

[P3] J. B. Balewski, A. T. Krupp, A. Gaj, D. Peter, H. P. Büchler, R. Löw, S. Hofferberth, and T. Pfau. "Coupling a single electron to a Bose-Einstein condensate". Nature **502** (2013), 664. arXiv: 1306.5181 (cit. on p. 81).

[P4] D. Peter, A. Griesmaier, T. Pfau, and H. P. Büchler. "Driving Dipolar Fermions into the Quantum Hall Regime by Spin-Flip Induced Insertion of Angular Momentum". Phys. Rev. Lett. **110** (2013), 145303. arXiv: 1302.1308 (cit. on p. 51).

[P6] D. Peter, N. Y. Yao, N. Lang, S. D. Huber, M. D. Lukin, and H. P. Büchler. "Topological bands with Chern number C=2 by dipolar exchange interactions". Phys. Rev. A **91** (2015), 053617. arXiv: 1410.5667 (cit. on pp. 15, 29, 59, 89).

[P5] M. Klinsmann, D. Peter, and H. P. Büchler. "Ferroelectric quantum phase transition with cold polar molecules" (2014). arXiv: 1412.0521 (cit. on pp. 17, 26).

[7] K. Klitzing, G. Dorda, and M. Pepper. "New Method for High-Accuracy Determination of the Fine-Structure Constant Based on Quantized Hall Resistance". Phys. Rev. Lett. **45** (1980), 494 (cit. on pp. 11, 37).

[8] K. von Klitzing. "The quantized Hall effect". Rev. Mod. Phys. **58** (1986), 519 (cit. on p. 11).

[9] R. B. Laughlin. "Quantized Hall conductivity in two dimensions". Phys. Rev. B **23** (1981), 5632 (cit. on p. 11).

[10] B. I. Halperin. "Quantized Hall conductance, current-carrying edge states, and the existence of extended states in a two-dimensional disordered potential". Phys. Rev. B **25** (1982), 2185 (cit. on p. 11).

[11] D. Thouless, M. Kohmoto, M. Nightingale, and M. den Nijs. "Quantized Hall Conductance in a Two-Dimensional Periodic Potential". Phys. Rev. Lett. **49** (1982), 405 (cit. on p. 11).

[12] Q. Niu, D. J. Thouless, and Y.-S. Wu. "Quantized Hall conductance as a topological invariant". Phys. Rev. B **31** (1985), 3372 (cit. on pp. 11, 64).

[13] M. Kohmoto. "Topological invariant and the quantization of the Hall conductance". Ann. Phys. (N. Y). **160** (1985), 343 (cit. on p. 11).

[14] J. E. Avron and R. Seiler. "Quantization of the Hall Conductance for General, Multiparticle Schrödinger Hamiltonians". Phys. Rev. Lett. **54** (1985), 259 (cit. on pp. 11, 64).

[15] M. Kohmoto. "Zero modes and the quantized Hall conductance of the two-dimensional lattice in a magnetic field". Phys. Rev. B **39** (1989), 11943 (cit. on p. 11).

[16] J. Bellissard, A. van Elst, and H. Schulz-Baldes. "The Non-Commutative Geometry of the Quantum Hall Effect". J. Math. Phys. **35** (1994), 533. arXiv: 9411052 [cond-mat] (cit. on p. 11).

[17] J. Avron, D. Osadchy, and R. Seiler. "A topological look at the quantum Hall effect". Phys. Today **56** (2003), 38. arXiv: 1201.1690v1 (cit. on p. 11).

[18] M. V. Berry. "Quantal Phase Factors Accompanying Adiabatic Changes". Proc. R. Soc. A Math. Phys. Eng. Sci. **392** (1984), 45 (cit. on pp. 11, 54).

[19] J. Zak. "Berry's phase for energy bands in solids". Phys. Rev. Lett. **62** (1989), 2747 (cit. on pp. 11, 54).

[20] D. C. Tsui, H. L. Stormer, and A. C. Gossard. "Two-dimensional magnetotransport in the extreme quantum limit". Phys. Rev. Lett. **48** (1982), 1559 (cit. on p. 11).

[21] R. B. Laughlin. "Anomalous Quantum Hall Effect: An Incompressible Quantum Fluid with Fractionally Charged Excitations". Phys. Rev. Lett. **50** (1983), 1395 (cit. on pp. 12, 37).

[22] X. G. Wen and Q. Niu. "Ground-state degeneracy of the fractional quantum Hall states in the presence of a random potential and on high-genus Riemann surfaces". Phys. Rev. B **41** (1990), 9377 (cit. on p. 12).

[23] X.-G. Wen. "Topological orders and Edge excitations in FQH states". Adv. Phys. **44** (1995), 67. arXiv: 9506066 [cond-mat] (cit. on p. 12).

[24] R. Willett, J. P. Eisenstein, H. L. Störmer, D. C. Tsui, A. C. Gossard, and J. H. English. "Observation of an even-denominator quantum number in the fractional quantum Hall effect". Phys. Rev. Lett. **59** (1987), 1776 (cit. on p. 12).

[25] G. Moore and N. Read. "Nonabelions in the fractional quantum hall effect". Nucl. Phys. B **360** (1991), 362 (cit. on p. 12).

[26] A. Y. Kitaev. "Fault-tolerant quantum computation by anyons". Ann. Phys. (N. Y). **303** (2003), 2 (cit. on p. 12).

[27] J. Larmor. *Aether and matter*. Cambridge University Press, 1900 (cit. on p. 12).

[28] V. Schweikhard, I. Coddington, P. Engels, V. P. Mogendorff, and E. A. Cornell. "Rapidly rotating Bose-Einstein condensates in and near the lowest Landau level". Phys. Rev. Lett. **92** (2004), 040404. arXiv: 0308582 [cond-mat] (cit. on pp. 13, 38).

[29] V. Bretin, S. Stock, Y. Seurin, and J. Dalibard. "Fast rotation of a Bose-Einstein condensate." Phys. Rev. Lett. **92** (2004), 050403 (cit. on p. 13).

[30] N. Cooper. "Rapidly rotating atomic gases". Adv. Phys. **57** (2008), 539 (cit. on pp. 13, 37).

[31] A. Fetter. "Rotating trapped Bose-Einstein condensates". Rev. Mod. Phys. **81** (2009), 647 (cit. on pp. 13, 37).

[32] F. D. M. Haldane. "Model for a Quantum Hall Effect without Landau Levels: Condensed-Matter Realization of the "Parity Anomaly"". Phys. Rev. Lett. **61** (1988), 2015 (cit. on pp. 13, 51, 63).

[33] Y. Hatsugai. "Chern number and edge states in the integer quantum Hall effect". Phys. Rev. Lett. **71** (1993), 3697 (cit. on pp. 13, 54, 66).

[34] R. Peierls. "Zur Theorie des Diamagnetismus von Leitungselektronen". Zeitschrift für Phys. **80** (1933), 763 (cit. on p. 13).

[35] N. Cooper. "Optical Flux Lattices for Ultracold Atomic Gases". Phys. Rev. Lett. **106** (2011), 175301 (cit. on p. 13).

[36] M. Aidelsburger, M. Atala, S. Nascimbène, S. Trotzky, Y.-a. Chen, and I. Bloch. "Experimental Realization of Strong Effective Magnetic Fields in an Optical Lattice". Phys. Rev. Lett. **107** (2011), 255301 (cit. on pp. 13, 37).

[37] M. Aidelsburger, M. Atala, M. Lohse, J. T. Barreiro, B. Paredes, and I. Bloch. "Realization of the Hofstadter Hamiltonian with Ultracold Atoms in Optical Lattices". Phys. Rev. Lett. **111** (2013), 185301 (cit. on p. 13).

[38] H. Miyake, G. a. Siviloglou, C. J. Kennedy, W. C. Burton, and W. Ketterle. "Realizing the Harper Hamiltonian with Laser-assisted Tunneling in Optical Lattices". Phys. Rev. Lett. **111** (2013), 185302. arXiv: 1308.1431 (cit. on p. 13).

[39] C. J. Kennedy, W. C. Burton, W. C. Chung, and W. Ketterle. "Observation of Bose-Einstein Condensation in a Strong Synthetic Magnetic Field" (2015). arXiv: 1503.08243v1 (cit. on p. 13).

[40] J. Struck, C. Ölschläger, M. Weinberg, P. Hauke, J. Simonet, A. Eckardt, M. Lewenstein, K. Sengstock, and P. Windpassinger. "Tunable Gauge Potential for Neutral and Spinless Particles in Driven Optical Lattices". Phys. Rev. Lett. **108** (2012), 225304 (cit. on pp. 13, 37).

[41] J. Struck et al. "Engineering Ising-XY spin-models in a triangular lattice using tunable artificial gauge fields". Nat. Phys. **9** (2013), 738 (cit. on p. 13).

[42] G. Jotzu, M. Messer, R. Desbuquois, M. Lebrat, T. Uehlinger, D. Greif, and T. Esslinger. "Experimental realization of the topological Haldane model with ultracold fermions". Nature **515** (2014), 237 (cit. on p. 13).

[43] Y.-J. Lin, K. Jiménez-García, and I. B. Spielman. "Spin-orbit-coupled Bose-Einstein condensates." Nature **471** (2011), 83 (cit. on p. 13).

[44] L. W. Cheuk, A. T. Sommer, Z. Hadzibabic, T. Yefsah, W. S. Bakr, and M. W. Zwierlein. "Spin-Injection Spectroscopy of a Spin-Orbit Coupled Fermi Gas". Phys. Rev. Lett. **109** (2012), 095302 (cit. on p. 13).

[45] P. Wang, Z.-Q. Yu, Z. Fu, J. Miao, L. Huang, S. Chai, H. Zhai, and J. Zhang. "Spin-Orbit Coupled Degenerate Fermi Gases". Phys. Rev. Lett. **109** (2012), 095301 (cit. on p. 13).

[46] C. Hamner, C. Qu, Y. Zhang, J. Chang, M. Gong, C. Zhang, and P. Engels. "Dicke-type phase transition in a spin-orbit-coupled Bose–Einstein condensate". Nat. Commun. **5** (2014), 4023. arXiv: 1405.2132v1 (cit. on p. 13).

[47] K. Jiménez-García, L. J. LeBlanc, R. A. Williams, M. C. Beeler, C. Qu, M. Gong, C. Zhang, and I. B. Spielman. "Tunable Spin-Orbit Coupling via Strong Driving in Ultracold-Atom Systems". Phys. Rev. Lett. **114** (2015), 125301 (cit. on p. 13).

[48] C. L. Kane and E. J. Mele. "Quantum Spin Hall Effect in Graphene". Phys. Rev. Lett. **95** (2005), 226801 (cit. on pp. 13, 69).

[49] C. L. Kane and E. J. Mele. "Z_2 Topological Order and the Quantum Spin Hall Effect". Phys. Rev. Lett. **95** (2005), 146802 (cit. on pp. 13, 51).

[50] X.-L. Qi and S.-C. Zhang. "Topological insulators and superconductors". Rev. Mod. Phys. **83** (2011), 1057 (cit. on pp. 13, 51).

[51] M. Hasan and C. Kane. "Colloquium: Topological insulators". Rev. Mod. Phys. **82** (2010), 3045 (cit. on pp. 13, 51, 52, 62).

[52] B. A. Bernevig, T. L. Hughes, and S.-C. Zhang. "Quantum spin Hall effect and topological phase transition in HgTe quantum wells." Science **314** (2006), 1757. arXiv: 0611399 [cond-mat] (cit. on p. 13).

[53] B. A. Bernevig and S.-C. Zhang. "Quantum spin Hall effect." Phys. Rev. Lett. **96** (2006), 106802. arXiv: 0504147 [cond-mat] (cit. on p. 13).

[54] M. König, S. Wiedmann, C. Brüne, A. Roth, H. Buhmann, L. W. Molenkamp, X.-L. Qi, and S.-C. Zhang. "Quantum spin hall insulator state in HgTe quantum wells." Science **318** (2007), 766. arXiv: 0710.0582 (cit. on p. 13).

[55] M. Hafezi, E. Demler, M. Lukin, and J. Taylor. "Robust optical delay lines via topological protection". Nat. Phys. **7** (2011), 9. arXiv: 1102.3256 (cit. on p. 13).

[56] M. Hafezi, S. Mittal, J. Fan, A. Migdall, and J. M. Taylor. "Imaging topological edge states in silicon photonics". Nat. Photonics **7** (2013), 1001. arXiv: 1302.2153 (cit. on pp. 13, 65).

[57] M. C. Rechtsman, J. M. Zeuner, Y. Plotnik, Y. Lumer, D. Podolsky, F. Dreisow, S. Nolte, M. Segev, and A. Szameit. "Photonic Floquet topological insulators". Nature **496** (2013), 196 (cit. on p. 13).

[58] R. Süsstrunk and S. D. Huber. "Observation of phononic helical edge states in a mechanical 'topological insulator'" (2015). arXiv: 1503.06808 (cit. on p. 13).

[59] M. Atala, M. Aidelsburger, J. T. Barreiro, D. Abanin, T. Kitagawa, E. Demler, and I. Bloch. "Direct measurement of the Zak phase in topological Bloch bands". Nat. Phys. **9** (2013), 795 (cit. on p. 13).

[60] L. Duca, T. Li, and M. Reitter. "An Aharonov-Bohm interferometer for determining Bloch band topology". Science **347** (2014), 288. arXiv: 1407.5635 (cit. on p. 13).

[61] M. Aidelsburger, M. Lohse, C. Schweizer, M. Atala, J. T. Barreiro, S. Nascimbène, N. R. Cooper, I. Bloch, and N. Goldman. "Revealing the topology of Hofstadter bands with ultracold bosonic atoms". Nat. Phys. **11** (2014), 162. arXiv: 1407.4205 (cit. on p. 13).

[62] K. Goral, K. Rzazewski, and T. Pfau. "Bose-Einstein condensation with magnetic dipole-dipole forces". Phys. Rev. A **61** (1999), 051601 (cit. on p. 15).

[63] L. Santos, G. V. Shlyapnikov, P. Zoller, and M. Lewenstein. "Bose-Einstein condensation in trapped dipolar gases". Phys. Rev. Lett. **85** (2000), 4. arXiv: 0005009 [cond-mat] (cit. on p. 15).

[64] L. Santos, G. V. Shlyapnikov, and M. Lewenstein. "Roton-maxon spectrum and stability of trapped dipolar Bose-Einstein condensates." Phys. Rev. Lett. **90** (2003), 250403. arXiv: 0301474 [cond-mat] (cit. on p. 15).

[65] A. Griesmaier, J. Werner, S. Hensler, J. Stuhler, and T. Pfau. "Bose-Einstein Condensation of Chromium". Phys. Rev. Lett. **94** (2005), 160401 (cit. on pp. 15, 16).

[66] J. Stuhler, A. Griesmaier, T. Koch, M. Fattori, T. Pfau, S. Giovanazzi, P. Pedri, and L. Santos. "Observation of dipole-dipole interaction in a degenerate quantum gas". Phys. Rev. Lett. **95** (2005), 150406. arXiv: 0508228 [cond-mat] (cit. on p. 15).

[67] S. Ronen, D. C. E. Bortolotti, and J. L. Bohn. "Radial and angular rotons in trapped dipolar gases". Phys. Rev. Lett. **98** (2007), 030406. arXiv: 0607704 [cond-mat] (cit. on p. 15).

[68] T. Koch, T. Lahaye, J. Metz, B. Fröhlich, A. Griesmaier, and T. Pfau. "Stabilization of a purely dipolar quantum gas against collapse". Nat. Phys. **4** (2008), 218 (cit. on p. 15).

[69] T. Lahaye, J. Metz, B. Fröhlich, T. Koch, M. Meister, A. Griesmaier, T. Pfau, H. Saito, Y. Kawaguchi, and M. Ueda. "D-Wave collapse and explosion of a dipolar bose-einstein condensate". Phys. Rev. Lett. **101** (2008), 080401. arXiv: 0803.2442 (cit. on p. 15).

[70] T. Lahaye, C. Menotti, L. Santos, M. Lewenstein, and T. Pfau. "The physics of dipolar bosonic quantum gases". Reports Prog. Phys. **72** (2009), 126401 (cit. on pp. 15–17, 27, 51).

[71] A. Micheli, G. K. Brennen, and P. Zoller. "A toolbox for lattice-spin models with polar molecules". Nat. Phys. **2** (2006), 341 (cit. on pp. 15, 28).

[72] P. Hauke, F. M. Cucchietti, A. Müller-Hermes, M. C. Bañuls, J. I. Cirac, and M. Lewenstein. "Complete devil's staircase and crystal-superfluid transitions in a dipolar XXZ spin chain: A trapped ion quantum simulation". New J. Phys. **12** (2010), 113037. arXiv: 1008.2945 (cit. on pp. 15, 29).

[73] A. V. Gorshkov, S. R. Manmana, G. Chen, J. Ye, E. Demler, M. D. Lukin, and A. M. Rey. "Tunable Superfluidity and Quantum Magnetism with Ultracold Polar Molecules". Phys. Rev. Lett. **107** (2011), 115301 (cit. on pp. 15, 28, 29).

[74] A. Gorshkov, J. Otterbach, M. Fleischhauer, T. Pohl, and M. Lukin. "Photon-Photon Interactions via Rydberg Blockade". Phys. Rev. Lett. **107** (2011), 133602. arXiv: 1103.3700v1 (cit. on p. 15).

[75] S. V. Syzranov, M. L. Wall, V. Gurarie, and A. M. Rey. "Spin-orbital dynamics in a system of polar molecules". Nat Commun **5** (2014), 5391 (cit. on pp. 15, 29, 51, 59, 89).

[76] S. D. Huber and H. P. Büchler. "Dipole-Interaction-Mediated Laser Cooling of Polar Molecules to Ultracold Temperatures". Phys. Rev. Lett. **108** (2012), 193006. arXiv: 1112.0554 (cit. on p. 15).

[77] B. Yan, S. a. Moses, B. Gadway, J. P. Covey, K. R. a. Hazzard, A. M. Rey, D. S. Jin, and J. Ye. "Observation of dipolar spin-exchange interactions with lattice-confined polar molecules." Nature **501** (2013), 521 (cit. on pp. 15, 17, 58, 60).

[78] A. de Paz, A. Sharma, A. Chotia, E. Maréchal, J. H. Huckans, P. Pedri, L. Santos, O. Gorceix, L. Vernac, and B. Laburthe-Tolra. "Nonequilibrium quantum magnetism in a dipolar lattice gas". Phys. Rev. Lett. **111** (2013), 185305 (cit. on p. 15).

[79] K. R. a. Hazzard, M. V. D. Worm, M. Foss-Feig, S. R. Manmana, E. D. Torre, T. Pfau, M. Kastner, and A. M. Rey. "Quantum correlations and entanglement in far-from-equilibrium spin systems". Phys. Rev. A **90** (2014), 063622 (cit. on p. 15).

[80] D. Barredo, H. Labuhn, S. Ravets, T. Lahaye, A. Browaeys, and C. S. Adams. "Coherent Excitation Transfer in a "Spin Chain" of Three Rydberg Atoms". Phys. Rev. Lett. **114** (2014), 113002 (cit. on pp. 15, 17, 52).

[81] J. W. Britton, B. C. Sawyer, A. C. Keith, C.-C. J. Wang, J. K. Freericks, H. Uys, M. J. Biercuk, and J. J. Bollinger. "Engineered two-dimensional Ising interactions in a trapped-ion quantum simulator with hundreds of spins". Nature **484** (2012), 489. arXiv: 1204.5789 (cit. on p. 16).

[82] K. Kim, M.-S. Chang, S. Korenblit, R. Islam, E. E. Edwards, J. K. Freericks, G.-D. Lin, L.-M. Duan, and C. Monroe. "Quantum simulation of frustrated Ising spins with trapped ions." Nature **465** (2010), 590 (cit. on p. 16).

[83] J. Cai, A. Retzker, F. Jelezko, and M. B. Plenio. "A large-scale quantum simulator on a diamond surface at room temperature". Nat. Phys. **9** (2013), 168. arXiv: 1208.2874 (cit. on p. 16).

[84] M. J. Martin, M. Bishof, M. D. Swallows, X. Zhang, C. Benko, J. Von-Stecher, A. V. Gorshkov, A. M. Rey, and J. Ye. "A Quantum Many-Body Spin System in an Optical Lattice Clock". Science **341** (2013), 632 (cit. on p. 16).

[85] Q. Beaufils, R. Chicireanu, T. Zanon, B. Laburthe-Tolra, E. Maréchal, L. Vernac, J.-C. Keller, and O. Gorceix. "All-optical production of chromium Bose-Einstein condensates". Phys. Rev. A **77** (2008), 61601 (cit. on p. 16).

[86] B. Naylor, A. Reigue, E. Maréchal, O. Gorceix, B. Laburthe-Tolra, and L. Vernac. "Chromium dipolar Fermi sea". Phys. Rev. A **91** (2015), 011603 (cit. on p. 16).

[87] M. Lu, N. Q. Burdick, S. H. Youn, and B. L. Lev. "Strongly Dipolar Bose-Einstein Condensate of Dysprosium". Phys. Rev. Lett. **107** (2011), 190401 (cit. on p. 16).

[88] M. Lu, N. Burdick, and B. Lev. "Quantum Degenerate Dipolar Fermi Gas". Phys. Rev. Lett. **108** (2012), 215301 (cit. on pp. 16, 38, 47).

[89] K. Aikawa, A. Frisch, M. Mark, S. Baier, A. Rietzler, R. Grimm, and F. Ferlaino. "Bose-Einstein Condensation of Erbium". Phys. Rev. Lett. **108** (2012), 210401 (cit. on p. 16).

[90] K. Aikawa, A. Frisch, M. Mark, S. Baier, R. Grimm, and F. Ferlaino. "Reaching Fermi degeneracy via universal dipolar scattering". Phys. Rev. Lett. **112** (2014), 010404. arXiv: 1310.5676 (cit. on pp. 16, 38).

[91] S. Hensler, J. Werner, A. Griesmaier, P. Schmidt, A. Görlitz, T. Pfau, S. Giovanazzi, and K. Rzazewski. "Dipolar relaxation in an ultra-cold gas of magnetically trapped chromium atoms". Appl. Phys. B Lasers Opt. **77** (2003), 765 (cit. on pp. 16, 38, 51).

[92] M. Fattori, T. Koch, S. Goetz, A. Griesmaier, S. Hensler, J. Stuhler, and T. Pfau. "Demagnetization cooling of a gas". Nat. Phys. **2** (2006), 765 (cit. on pp. 16, 51).

[93] V. V. Volchkov, J. Rührig, T. Pfau, and A. Griesmaier. "Efficient demagnetization cooling of atoms and its limits". Phys. Rev. A **89** (2014), 043417. arXiv: 1306.3365 (cit. on p. 16).

[94] S. Ospelkaus, K.-K. Ni, D. Wang, M. H. G. de Miranda, B. Neyenhuis, G. Quéméner, P. S. Julienne, J. L. Bohn, D. S. Jin, and J. Ye. "Quantum-state controlled chemical reactions of ultracold potassium-rubidium molecules." Science **327** (2010), 853. arXiv: 0912.3854 (cit. on p. 16).

[95] G. Quéméner and P. S. Julienne. "Ultracold molecules under control!" Chem. Rev. **112** (2012), 4949 (cit. on pp. 16, 17).

[96] K.-K. Ni, S. Ospelkaus, M. H. G. de Miranda, A. Pe'er, B. Neyenhuis, J. J. Zirbel, S. Kotochigova, P. S. Julienne, D. S. Jin, and J. Ye. "A high phase-space-density gas of polar molecules." Science **322** (2008), 231 (cit. on pp. 17, 51).

[97] S. Ospelkaus, K.-K. Ni, G. Quéméner, B. Neyenhuis, D. Wang, M. H. G. de Miranda, J. L. Bohn, J. Ye, and D. S. Jin. "Controlling the Hyperfine State of Rovibronic Ground-State Polar Molecules". Phys. Rev. Lett. **104** (2010), 030402 (cit. on pp. 17, 51, 58, 60).

[98] C. H. Wu, J. W. Park, P. Ahmadi, S. Will, and M. W. Zwierlein. "Ultracold fermionic Feshbach molecules of Na23K40". Phys. Rev. Lett. **109** (2012), 085301 (cit. on pp. 17, 51).

[99] M. S. Heo, T. T. Wang, C. a. Christensen, T. M. Rvachov, D. a. Cotta, J. H. Choi, Y. R. Lee, and W. Ketterle. "Formation of ultracold fermionic NaLi Feshbach molecules". Phys. Rev. A **86** (2012), 021602 (cit. on pp. 17, 51).

[100] A. Chotia, B. Neyenhuis, S. a. Moses, B. Yan, J. P. Covey, M. Foss-Feig, A. M. Rey, D. S. Jin, and J. Ye. "Long-lived dipolar molecules and Feshbach molecules in a 3D optical lattice". Phys. Rev. Lett. **108** (2012), 080405 (cit. on pp. 17, 51).

[101] R. Löw, H. Weimer, J. Nipper, J. B. Balewski, B. Butscher, H. P. Büchler, and T. Pfau. "An experimental and theoretical guide to strongly interacting Rydberg gases". J. Phys. B **45** (2012), 113001. arXiv: 1202.2871v1 (cit. on p. 17).

[102] S. Westermann, T. Amthor, a. L. De Oliveira, J. Deiglmayr, M. Reetz-Lamour, and M. Weidemüller. "Dynamics of resonant energy transfer in a cold Rydberg gas". Phys. Rev. A **65** (2006), 063404 (cit. on p. 17).

[103] J. Nipper, J. B. Balewski, A. T. Krupp, B. Butscher, R. Löw, and T. Pfau. "Highly resolved measurements of stark-tuned Förster resonances between Rydberg atoms". Phys. Rev. Lett. **108** (2012), 113001 (cit. on p. 17).

[104] S. Ravets, H. Labuhn, D. Barredo, T. Lahaye, and A. Browaeys. "Measurement of the Angular Dependence of the Dipole-Dipole Interaction Between Two Individual Rydberg Atoms at a Förster Resonance" (2015). arXiv: 1504.00301v1 (cit. on p. 17).

[105] D. Booth, S. T. Rittenhouse, J. Yang, H. Sadeghpour, and J. Shaffer. "Production of trilobite Rydberg molecule dimers with thousand-Debye permanent electric dipole moments" (2014). arXiv: 1411.5291 (cit. on p. 17).

[106] S. Weber. "To be published". Master Thesis. Universität Stuttgart, 2015 (cit. on pp. 17, 66).

[107] A. Micheli, G. Pupillo, H. P. Büchler, and P. Zoller. "Cold polar molecules in two-dimensional traps: Tailoring interactions with external fields for novel quantum phases". Phys. Rev. A **76** (2007), 043604 (cit. on pp. 18, 21).

[108] A. V. Gorshkov, S. R. Manmana, G. Chen, E. Demler, M. D. Lukin, and A. M. Rey. "Quantum magnetism with polar alkali-metal dimers". Phys. Rev. A **84** (2011), 033619 (cit. on pp. 18, 20, 28, 29).

[109] J. M. Brown and A. Carrington. *Rotational Spectroscopy of Diatomic Molecules*. Cambridge Molecular Science. Cambridge University Press, 2003 (cit. on p. 18).

[110] T. Holstein and H. Primakoff. "Field dependence of the intrinsic domain magnetization of a ferromagnet". Phys. Rev. **58** (1940), 1098 (cit. on p. 24).

[111] M. Klinsmann. "Ferroelectricity and quantum phase transition in cold polar molecules". Diploma thesis. Universität Stuttgart, 2011 (cit. on p. 26).

[112] B. Spivak and S. A. Kivelson. "Phases intermediate between a two-dimensional electron liquid and Wigner crystal". Phys. Rev. B **70** (2004), 155114 (cit. on pp. 27, 36).

[113] H. P. Büchler, E. Demler, M. Lukin, A. Micheli, N. Prokof'ev, G. Pupillo, and P. Zoller. "Strongly Correlated 2D Quantum Phases with Cold Polar Molecules: Controlling the Shape of the Interaction Potential". Phys. Rev. Lett. **98** (2007), 060404 (cit. on p. 27).

[114] G. E. Astrakharchik, J. Boronat, I. L. Kurbakov, and Y. E. Lozovik. "Quantum phase transition in a two-dimensional system of dipoles". Phys. Rev. Lett. **98** (2007), 060405. arXiv: 0608246 [cond-mat] (cit. on p. 27).

[115] L. Bonsall and A. A. Maradudin. "Some static and dynamical properties of a two-dimensional Wigner crystal". Phys. Rev. B **15** (1977), 1959 (cit. on pp. 27, 30).

[116] E. G. Dalla Torre, E. Berg, and E. Altman. "Hidden Order in 1D Bose Insulators". Phys. Rev. Lett. **97** (2006), 260401 (cit. on p. 28).

[117] L. Pollet, J. D. Picon, H. P. Büchler, and M. Troyer. "Supersolid phase with cold polar molecules on a triangular lattice". Phys. Rev. Lett. **104** (2010), 125302. arXiv: 0906.2126 (cit. on p. 28).

[118] B. Capogrosso-Sansone, C. Trefzger, M. Lewenstein, P. Zoller, and G. Pupillo. "Quantum Phases of Cold Polar Molecules in 2D Optical Lattices". Phys. Rev. Lett. **104** (2010), 125301 (cit. on p. 28).

[119] C. Trefzger, C. Menotti, and M. Lewenstein. "Pair-supersolid phase in a bilayer system of dipolar lattice bosons". Phys. Rev. Lett. **103** (2009), 035304. arXiv: 0904.1552 (cit. on p. 28).

[120] L. Bonnes, H. Büchler, and S. Wessel. "Polar molecules with three-body interactions on the honeycomb lattice". New J. Phys. **12** (2010), 053027 (cit. on p. 28).

[121] N. R. Cooper and G. V. Shlyapnikov. "Stable topological superfluid phase of ultracold polar fermionic molecules". Phys. Rev. Lett. **103** (2009), 155302. arXiv: 0907.3080 (cit. on p. 28).

[122] D. W. Wang, M. D. Lukin, and E. Demler. "Quantum fluids of self-assembled chains of polar molecules". Phys. Rev. Lett. **97** (2006), 180413. arXiv: 0608250 [cond-mat] (cit. on p. 28).

[123] M. Müller, I. Lesanovsky, H. Weimer, H. P. Büchler, and P. Zoller. "Mesoscopic Rydberg Gate Based on Electromagnetically Induced Transparency". Phys. Rev. Lett. **102** (2009), 170502. arXiv: 0811.1155v2 (cit. on p. 28).

[124] S. Müller. "Quantum phase transitions with polar molecules". Diploma thesis. Universität Stuttgart, 2010 (cit. on pp. 29, 30, 59, 93).

[125] R. Kubo. "The spin-wave theory of antiferromagnetics". Phys. Rev. **87** (1952), 568 (cit. on p. 31).

[126] A. Auerbach. *Interacting Electrons and Quantum Magnetism*. 1994, 255 (cit. on p. 31).

[127] X. L. Deng, D. Porras, and J. I. Cirac. "Effective spin quantum phases in systems of trapped ions". Phys. Rev. A **72** (2005), 063407. arXiv: 0509197 [quant-ph] (cit. on p. 32).

[128] N. Schuch, J. I. Cirac, and M. M. Wolf. "Quantum states on harmonic lattices". Commun. Math. Phys. **267** (2006), 65. arXiv: 0509166 [quant-ph] (cit. on p. 32).

[129] P. Bruno. "Absence of spontaneous magnetic order at nonzero temperature in one- and two-dimensional Heisenberg and XY systems with long-range interactions." Phys. Rev. Lett. **87** (2001), 137203. arXiv: 0105129 [cond-mat] (cit. on pp. 33, 34).

[130] N. D. Mermin and H. Wagner. "Absence of ferromagnetism or antiferromagnetism in one- or two-dimensional isotropic Heisenberg models". Phys. Rev. Lett. **17** (1966), 1133 (cit. on p. 34).

[131] J. R. de Sousa. "Phase diagram in the quantum XY model with long-range interactions". Eur. Phys. J. B **43** (2005), 93 (cit. on p. 34).

[132] K. Jiménez-García, L. LeBlanc, R. Williams, M. Beeler, A. Perry, and I. Spielman. "Peierls Substitution in an Engineered Lattice Potential". Phys. Rev. Lett. **108** (2012), 225303 (cit. on p. 37).

[133] Y. Lin, R. L. Compton, K. Jiménez-García, J. V. Porto, and I. B. Spielman. "Synthetic magnetic fields for ultracold neutral atoms." Nature **462** (2009), 628 (cit. on p. 37).

[134] J. Dalibard, F. Gerbier, G. Juzeliunas, and P. Öhberg. "Colloquium: Artificial gauge potentials for neutral atoms". Rev. Mod. Phys. **83** (2011), 1523 (cit. on p. 37).

[135] N. Cooper, E. Rezayi, and S. Simon. "Vortex Lattices in Rotating Atomic Bose Gases with Dipolar Interactions". Phys. Rev. Lett. **95** (2005), 200402 (cit. on pp. 37, 49).

[136] M. Baranov, K. Osterloh, and M. Lewenstein. "Fractional Quantum Hall States in Ultracold Rapidly Rotating Dipolar Fermi Gases". Phys. Rev. Lett. **94** (2005), 070404 (cit. on pp. 37, 49).

[137] K. Osterloh, N. Barberán, and M. Lewenstein. "Strongly Correlated States of Ultracold Rotating Dipolar Fermi Gases". Phys. Rev. Lett. **99** (2007), 160403 (cit. on pp. 37, 49, 50).

[138] A. Einstein and W. J. de Haas. "Experimenteller Nachweis der Ampèreschen Molekularströme". Verhandl. der Dtsch. Phys. Gesellschaft **17** (1915), 152 (cit. on p. 38).

[139] L. Santos and T. Pfau. "Spin-3 Chromium Bose-Einstein Condensates". Phys. Rev. Lett. **96** (2006), 190404 (cit. on pp. 38, 51).

[140] Y. Kawaguchi, H. Saito, and M. Ueda. "Einstein–de Haas Effect in Dipolar Bose-Einstein Condensates". Phys. Rev. Lett. **96** (2006), 080405 (cit. on pp. 38, 51).

[141] H. Yoshimoto and S. Kurihara. "Analytic treatment of interacting Fermi gas in an arbitrary dimensional harmonic trap". J. Phys. A. Math. Gen. **36** (2003), 10461 (cit. on p. 42).

[142] A. Berglund, S. Lee, and J. McClelland. "Sub-Doppler laser cooling and magnetic trapping of erbium". Phys. Rev. A **76** (2007), 053418 (cit. on p. 46).

[143] R. Chicireanu, A. Pouderous, R. Barbé, B. Laburthe-Tolra, E. Maréchal, L. Vernac, J.-C. Keller, and O. Gorceix. "Simultaneous magneto-optical trapping of bosonic and fermionic chromium atoms". Phys. Rev. A **73** (2006), 053406 (cit. on p. 46).

[144] A. Frisch, M. Mark, K. Aikawa, F. Ferlaino, J. L. Bohn, C. Makrides, A. Petrov, and S. Kotochigova. "Quantum chaos in ultracold collisions of gas-phase erbium atoms." Nature **507** (2014), 475. arXiv: 1312.1972 (cit. on p. 46).

[145] T. Maier, H. Kadau, M. Schmitt, M. Wenzel, C. Wink, T. Pfau, K. Jachymski, and P. S. Julienne. "Broad Feshbach resonances in collisions of ultracold Dysprosium atoms" (2015). arXiv: 1506.01875v1 (cit. on p. 46).

[146] B. Pasquiou, E. Maréchal, G. Bismut, P. Pedri, L. Vernac, O. Gorceix, and B. Laburthe-Tolra. "Spontaneous Demagnetization of a Dipolar Spinor Bose Gas in an Ultralow Magnetic Field". Phys. Rev. Lett. **106** (2011), 255303 (cit. on pp. 46, 51).

[147] F. Serwane, G. Zürn, T. Lompe, T. B. Ottenstein, a. N. Wenz, and S. Jochim. "Deterministic preparation of a tunable few-fermion system." Science **332** (2011), 336 (cit. on p. 47).

[148] G. Hardy and S. Ramanujan. "Asymptotic formulaae in combinatory analysis". Proc. London Math. Soc. **2** (1918), 75 (cit. on p. 49).

[149] R.-Z. Qiu, S.-P. Kou, Z.-X. Hu, X. Wan, and S. Yi. "Quantum Hall effects in fast-rotating Fermi gases with anisotropic dipolar interaction". Phys. Rev. A **83** (2011), 063633 (cit. on pp. 49, 50).

[150] T. Graß, M. a. Baranov, and M. Lewenstein. "Robustness of fractional quantum Hall states with dipolar atoms in artificial gauge fields". Phys. Rev. A **84** (2011), 043605. arXiv: 1105.0299 (cit. on p. 49).

[151] Y. Zhang, E. H. Rezayi, and K. Yang. "Realization of strong-pairing quantum Hall phase in bilayer cold atom systems with dipolar interactions". Phys. Rev. B **90** (2014), 165102. arXiv: 1407.7935 (cit. on p. 49).

[152] E. J. Bergholtz and Z. Liu. "Topological Flat Band Models and Fractional Chern Insulators". Int. J. Mod. Phys. B **27** (2013), 1330017 (cit. on p. 51).

[153] S. a. Parameswaran, R. Roy, and S. L. Sondhi. "Fractional quantum Hall physics in topological flat bands". Comptes Rendus Phys. **14** (2013), 816 (cit. on p. 51).

[154] C. Nayak, A. Stern, M. Freedman, and S. Das Sarma. "Non-Abelian anyons and topological quantum computation". Rev. Mod. Phys. **80** (2008), 1083 (cit. on p. 51).

[155] S. Raghu, X. L. Qi, C. Honerkamp, and S. C. Zhang. "Topological mott insulators". Phys. Rev. Lett. **100** (2008), 156401 (cit. on p. 51).

[156] Y.-F. Wang, Z.-C. Gu, C.-D. Gong, and D. N. Sheng. "Fractional Quantum Hall Effect of Hard-Core Bosons in Topological Flat Bands". Phys. Rev. Lett. **107** (2011), 146803 (cit. on pp. 51, 63, 68).

[157] T. Neupert, L. Santos, C. Chamon, and C. Mudry. "Fractional Quantum Hall States at Zero Magnetic Field". Phys. Rev. Lett. **106** (2011), 236804 (cit. on p. 51).

[158] Y.-F. Wang, H. Yao, C.-D. Gong, and D. N. Sheng. "Fractional quantum Hall effect in topological flat bands with Chern number two". Phys. Rev. B **86** (2012), 201101 (cit. on pp. 51, 68).

[159] A. G. Grushin, T. Neupert, C. Chamon, and C. Mudry. "Enhancing the stability of a fractional Chern insulator against competing phases". Phys. Rev. B **86** (2012), 205125 (cit. on p. 51).

[160] G. Möller and N. R. Cooper. "Composite Fermion Theory for Bosonic Quantum Hall States on Lattices". Phys. Rev. Lett. **103** (2009), 105303 (cit. on pp. 51, 68).

[161] K. Sun, W. V. Liu, and S. D. Sarma. "Topological semimetal: a probable new state of quantum optical lattice gases protected by D_4 symmetry". Nat. Phys. **8** (2010), 67 (cit. on p. 51).

[162] M. Barkeshli and X.-L. Qi. "Topological Nematic States and Non-Abelian Lattice Dislocations". Phys. Rev. X **2** (2012), 031013 (cit. on p. 51).

[163] F. Wang and Y. Ran. "Nearly flat band with Chern number C=2 on the dice lattice". Phys. Rev. B **84** (2011), 241103 (cit. on p. 51).

[164] A. Sterdyniak, C. Repellin, B. A. Bernevig, and N. Regnault. "Series of Abelian and non-Abelian states in C>1 fractional Chern insulators". Phys. Rev. B **87** (2013), 205137 (cit. on p. 51).

[165] Z. Liu, E. J. Bergholtz, H. Fan, and A. M. Läuchli. "Fractional Chern Insulators in Topological Flat Bands with Higher Chern Number". Phys. Rev. Lett. **109** (2012), 186805 (cit. on p. 51).

[166] N. Y. Yao, A. V. Gorshkov, C. R. Laumann, A. M. Läuchli, J. Ye, and M. D. Lukin. "Realizing Fractional Chern Insulators in Dipolar Spin Systems". Phys. Rev. Lett. **110** (2013), 185302 (cit. on pp. 51, 52, 63, 68).

[167] S. Yang, Z.-C. Gu, K. Sun, and S. Das Sarma. "Topological flat band models with arbitrary Chern numbers". Phys. Rev. B **86** (2012), 241112 (cit. on p. 51).

[168] A. Dauphin, M. Müller, and M. A. Martin-Delgado. "Rydberg-atom quantum simulation and Chern-number characterization of a topological Mott insulator". Phys. Rev. A **86** (2012), 053618 (cit. on p. 51).

[169] N. R. Cooper and R. Moessner. "Designing topological bands in reciprocal space". Phys. Rev. Lett. **109** (2012), 215302 (cit. on p. 51).

[170] N. R. Cooper and J. Dalibard. "Reaching Fractional Quantum Hall States with Optical Flux Lattices". Phys. Rev. Lett. **110** (2013), 185301 (cit. on p. 51).

[171] T. Shi and J. I. Cirac. "Topological phenomena in trapped-ion systems". Phys. Rev. A **87** (2013), 013606 (cit. on p. 51).

[172] N. Y. Yao, S. D. Bennett, C. R. Laumann, B. L. Lev, and a. V. Gorshkov. "Bilayer fractional quantum Hall states with ultracold dysprosium" (2015). arXiv: 1505.03099v1 (cit. on pp. 51, 52, 68).

[173] D. a. Pesin and L. Balents. "Mott physics and band topology in materials with strong spin-orbit interaction". Nat. Phys. **6** (2009), 376 (cit. on p. 51).

[174] E. Tang, J.-W. Mei, and X.-G. Wen. "High-Temperature Fractional Quantum Hall States". Phys. Rev. Lett. **106** (2011), 236802 (cit. on p. 51).

[175] Z. Qiao, W. K. Tse, H. Jiang, Y. Yao, and Q. Niu. "Two-dimensional topological insulator state and topological phase transition in bilayer graphene". Phys. Rev. Lett. **107** (2011), 256801. arXiv: 1109.1131 (cit. on p. 51).

[176] A. de Paz, A. Chotia, E. Maréchal, P. Pedri, L. Vernac, O. Gorceix, and B. Laburthe-Tolra. "Resonant demagnetization of a dipolar Bose-Einstein condensate in a three-dimensional optical lattice". Phys. Rev. A **87** (2013), 051609 (cit. on p. 51).

[177] M. Vengalattore, S. R. Leslie, J. Guzman, and D. M. Stamper-Kurn. "Spontaneously Modulated Spin Textures in a Dipolar Spinor Bose-Einstein Condensate". Phys. Rev. Lett. **100** (2008), 170403 (cit. on p. 51).

[178] D. M. Stamper-Kurn and M. Ueda. "Spinor Bose gases: Symmetries, magnetism, and quantum dynamics". Rev. Mod. Phys. **85** (2013), 1191 (cit. on p. 51).

[179] X.-J. Liu, X. Liu, C. Wu, and J. Sinova. "Quantum anomalous Hall effect with cold atoms trapped in a square lattice". Phys. Rev. A **81** (2010), 033622 (cit. on pp. 52, 63).

[180] T. D. Stanescu, V. Galitski, and S. Das Sarma. "Topological states in two-dimensional optical lattices". Phys. Rev. A **82** (2010), 013608 (cit. on pp. 52, 63).

[181] N. Goldman, F. Gerbier, and M. Lewenstein. "Realizing non-Abelian gauge potentials in optical square lattices: an application to atomic Chern insulators". J. Phys. B **46** (2013), 134010 (cit. on pp. 52, 63).

[182] F. Li, L. Sheng, and D. Y. Xing. "Extended Haldane's model and its simulation with ultracold atoms". EPL (Europhysics Lett. **84** (2008), 60004 (cit. on pp. 52, 63).

[183] N. Y. Yao, C. R. Laumann, A. V. Gorshkov, S. D. Bennett, E. Demler, P. Zoller, and M. D. Lukin. "Topological Flat Bands from Dipolar Spin Systems". Phys. Rev. Lett. **109** (2012), 266804 (cit. on pp. 52, 63).

[184] D. Jaksch and P. Zoller. "Creation of effective magnetic fields in optical lattices: the Hofstadter butterfly for cold neutral atoms". New J. Phys. **5** (2003), 56 (cit. on p. 52).

[185] M. J. Piotrowicz, M. Lichtman, K. Maller, G. Li, S. Zhang, L. Isenhower, and M. Saffman. "Two-dimensional lattice of blue-detuned atom traps using a projected Gaussian beam array". Phys. Rev. A **88** (2013), 013420 (cit. on p. 52).

[186] F. Nogrette, H. Labuhn, S. Ravets, D. Barredo, L. Béguin, A. Vernier, T. Lahaye, and A. Browaeys. "Single-Atom Trapping in Holographic 2D Arrays of Microtraps with Arbitrary Geometries". Phys. Rev. X **4** (2014), 021034 (cit. on p. 52).

[187] B. A. Bernevig. *Topological insulators and topological superconductors*. Princeton University Press, 2013 (cit. on p. 52).

[188] J. E. Moore. "Notes for MIT minicourse on topological phases" (2011) (cit. on p. 53).

[189] A. Schnyder, S. Ryu, A. Furusaki, and A. Ludwig. "Classification of topological insulators and superconductors in three spatial dimensions". Phys. Rev. B **78** (2008), 195125 (cit. on pp. 55, 77).

[190] A. Kitaev. "Periodic table for topological insulators and superconductors". AIP Conf. Proc. (2009). arXiv: 0901.2686 (cit. on pp. 55, 77).

[191] S. Ryu, A. P. Schnyder, A. Furusaki, and A. W. W. Ludwig. "Topological insulators and superconductors: tenfold way and dimensional hierarchy". New J. Phys. **12** (2010), 065010 (cit. on pp. 55, 77).

[192] X. Liu, Z. Wang, X. C. Xie, and Y. Yu. "Abelian and non-Abelian anyons in integer quantum anomalous Hall effect and topological phase transitions via superconducting proximity effect". Phys. Rev. B **83** (2011), 125105 (cit. on p. 63).

[193] Y.-X. Wang, F.-X. Li, and Y.-M. Wu. "Quantum Hall effect of Haldane model under magnetic field". EPL (Europhysics Lett. **105** (2014), 17002 (cit. on p. 63).

[194] T. Fukui, Y. Hatsugai, and H. Suzuki. "Chern Numbers in Discretized Brillouin Zone: Efficient Method of Computing (Spin) Hall Conductances". J. Phys. Soc. Japan **74** (2005), 1674 (cit. on p. 65).

[195] Y. M. Lu and A. Vishwanath. "Theory and classification of interacting integer topological phases in two dimensions: A Chern-Simons approach". Phys. Rev. B **86** (2012), 125119. arXiv: 1205.3156 (cit. on p. 68).

[196] X. Chen, Z. C. Gu, Z. X. Liu, and X. G. Wen. "Symmetry protected topological orders and the group cohomology of their symmetry group". Phys. Rev. B **87** (2013), 155114 (cit. on p. 68).

[197] B. I. Halperin. "Statistics of quasiparticles and the hierarchy of fractional quantized hall states". Phys. Rev. Lett. **52** (1984), 1583 (cit. on p. 68).

[198] Y.-H. Wu and J. K. Jain. "Quantum Hall effect of two-component bosons at fractional and integral fillings". Phys. Rev. B **87** (2013), 245123 (cit. on p. 68).

[199] M. Creutz. "End states, ladder compounds, and domain-wall fermions". Phys. Rev. Lett. **83** (1999), 2636 (cit. on pp. 69, 72, 74).

[200] A. Bermudez, D. Patanè, L. Amico, and M. Martin-Delgado. "Topology-induced anomalous defect production by crossing a quantum critical point". Phys. Rev. Lett. **102** (2009), 135702. arXiv: 0811.3843 (cit. on p. 69).

[201] M. Tovmasyan, E. P. L. van Nieuwenburg, and S. D. Huber. "Geometry-induced pair condensation". Phys. Rev. B **88** (2013), 220510 (cit. on pp. 69, 78, 79).

[202] S. Takayoshi, H. Katsura, N. Watanabe, and H. Aoki. "Phase diagram and pair Tomonaga-Luttinger liquid in a Bose-Hubbard model with flat bands". Phys. Rev. A **88** (2013), 063613. arXiv: 1309.6329 (cit. on p. 69).

[203] D. Sticlet, L. Seabra, F. Pollmann, and J. Cayssol. "From fractionally charged solitons to Majorana bound states in a one-dimensional interacting model". Phys. Rev. B **89** (2014), 115430. arXiv: 1312.6131 (cit. on p. 69).

[204] C.-K. Chiu and A. P. Schnyder. "Classification of reflection symmetry protected topological semimetals and nodal superconductors". Phys. Rev. B **90** (2014), 205136. arXiv: 1408.4642 (cit. on p. 77).

[205] Y.-m. Lu and D.-h. Lee. "Inversion symmetry protected topological insulators and superconductors" (2014). arXiv: 1403.5558 (cit. on p. 77).

[206] W. P. Su, J. R. Schrieffer, and A. J. Heeger. "Solitons in Polyacetylene". Phys. Rev. Lett. **42** (1979), 1698 (cit. on p. 78).

[207] L. Wang, M. Troyer, and X. Dai. "Topological charge pumping in a one-dimensional optical lattice". Phys. Rev. Lett. **111** (2013), 026802. arXiv: 1301.7435 (cit. on p. 78).

[208] J. B. Balewski. "A single electron in a Bose-Einstein condensate". PhD thesis. Universität Stuttgart, 2014 (cit. on pp. 81, 85).

[209] T. Karpiuk, M. Brewczyk, K. Rzążewski, J. B. Balewski, A. T. Krupp, A. Gaj, R. Löw, S. Hofferberth, and T. Pfau. "Detecting and imaging single Rydberg electrons in a Bose-Einstein condensate" (2014). arXiv: 1402.6875 (cit. on pp. 81, 84).

[210] A. Gaj, A. T. Krupp, J. B. Balewski, R. Löw, S. Hofferberth, and T. Pfau. "From molecular spectra to a density shift in dense Rydberg gases." Nat. Commun. **5** (2014), 4546. arXiv: 1404.5761 (cit. on p. 81).

[211] M. L. Glasser. "The evaluation of lattice sums. I. Analytic procedures". J. Math. Phys. **14** (1973), 409 (cit. on p. 92).

[212] M. Moshinsky. "Transformation brackets for harmonic oscillator functions". Nucl. Phys. **13** (1959), 104 (cit. on p. 102).

[213] I. Talmi. "Nuclear Spectroscopy with Harmonic Oscillator Wave Functions". Helv. Phys. Acta **25** (1952), 185 (cit. on p. 102).

Acknowledgements

The last few years would not have been as interesting and enjoyable without the help and the company of certain special people. Primarily, I am very grateful to Hans Peter Büchler for a very inspiring time and the chance to work on a lot of interesting projects. I have learned a lot from you and I very much enjoy discussing physics with you. Thank you for always supporting me and for giving me many valuable opportunities throughout my PhD. I want to thank Tilman Pfau for being the first one to get me interested in this exciting field of physics. You have supported me in many different ways throughout my years at the university and I am very grateful for that. I am very thankful to Maria Daghofer for promptly accepting to review my thesis.

I have profited a lot from discussing and doing physics with many great people I have met during the last years. Special thanks go to my fellow PhD students Nicolai Lang and Przemysław Bienias for uncounted hours of interesting and very helpful discussions. Further thanks for invaluable discussions go to Jonathan Balewski, Sebastian Weber, Norman Yao, Alban Urvoy, Axel Griesmaier, Sebastian Huber, Thierry Lahaye, Antoine Browaeys and Kazimierz Rzążewski. Particular thanks also goes to friends and colleagues I have met throughout the years: Adam Bühler, Thorsten Treffon, Krzysztof Pawłowski, Jens Honer, Stephan Humeniuk, Michael Hauber, Eslam Khalaf, Karim Bouadim and Anita Gaj. It would not have been the same without you. Thanks also go to Mikhail Lukin for giving me the opportunity to join his group in Harvard for two months and to Ildiko Poljak and Oliver Nagel for the organizational part. A huge thank you goes to Andi, Basti, Fabi, Holger, Matze and Patrick for many memorable experiences throughout the last nine years. Last, extraordinary thanks go to my family for always supporting me!